# Predicting Buckling and Plasticity of Finite Element Models Using Machine Learning

## An Application of Convolutional Neural Networks on the Ultimate Strength and Stress Distribution Prediction of Stiffened Panels

K.M. Snel

# Predicting Buckling and Plasticity of Finite Element Models Using Machine Learning

## An Application of Convolutional Neural Networks on the Ultimate Strength and Stress Distribution Prediction of Stiffened Panels

by

K.M. Snel

to obtain the degree of Master of Science
at the Delft University of Technology.

| | | |
|---|---|---|
| Student number: | 4275233 | |
| Project duration: | September 9, 2019 - September 10, 2020 | |
| Thesis committee: | Prof. Ir. J. J. Hopman, | TU Delft, Chair |
| | Dr. C. L. Walters, | TU Delft, Supervisor |
| | Dr. N. Yorke-Smith, | TU Delft, Supervisor |

# Preface

This thesis on predicting the ultimate strength of stiffened panels by using machine learning is written to obtain the Master of Science degree in Marine Technology at the Delft University of Technology. This research was performed under the supervision of Dr. Carey Walters for the structural part, and Dr. Neil Yorke-Smith for the machine learning part.

During my thesis, I have acquired knowledge on a wide variety of topics. At the start of the thesis, I had little experience with the buckling of stiffened panels, modeling with Ansys, and the use of machine learning, which are actually the topics on which the entire thesis is based. The thesis topic gained my interest and, therefore, I started this thesis without really knowing what the final goal would be. The project started by choosing Carey as the daily supervisor for my thesis. We did not know each other since I did not attend any of your courses. Still, I enjoyed the conversation we had about different graduation topics. Carey, I would like to thank you for all the meetings we had, the ideas you gave me, and the great off-topic chats we had during the meetings. I want to thank you for getting Neil involved in the project. Neil, I would like to thank you for your meetings, the great feedback during the project, and supporting my project while I had no prior knowledge of machine learning. I would like to thank both of you in guiding me through the project while still giving me all the freedom in my thesis.

Besides my supervisors, I would also like to thank my family and friends for supporting me during my thesis and my time at the university. I would also like to thank my great office friends who provided me with lots of fun every day. And, of course, I must thank my lovely Renée for being my greatest support. You have endured all my stories about machine learning and buckling, asked critical questions and wanted to proofread parts of my thesis.

*K.M. Snel*
*Delft, September 2020*

# Contents

# Summary

The first development of ships bigger than 300 meter is dated back to the 1960s. Since then, the development of bigger, more efficient vessels continued, pushing the designs towards their strength limits. Sometimes, constructions are pushed beyond their limits with the possibility of significant negative economic and environmental impact or, in the worst case, impact on human life. Back in 2013, the MOL Comfort, a 316-meter long container vessel, suffered from buckling, followed by a major collapse in the bottom hull plating of the ship resulting in the ship breaking into two parts. The failure of this new vessel, built in 2008, makes it explicitly clear why the development of accurate methods and models is still required to predict if a design can withstand the expected loads during its operations.

In the past two decades, machine learning has been applied in the field of structural design, but the amount of research regarding the scalability and generalizability of machine learning within structural design is limited. This report investigates the application, scalability and generalizability of machine learning to predict the ultimate strength of stiffened panels. In shipbuilding, stiffened panels are considered one of the main structural elements. The main research question answered in this research is:

*Under what conditions is it possible to predict buckling and plasticity for a meshed stiffened panel making use of machine learning?*

Two parts are presented in this research to provide an answer to the research question. The first part of this research represents the process of generating a large dataset that is used to train the machine learning model. The dataset contains a broad set of longitudinal uni-axial compressed, and lateral pressure loaded stiffened panels with geometries that can realistically be used in shipbuilding. Optimization is performed on a developed analytical model that incorporates structural non-linearities and structural design rules provided by classification societies. The obtained geometries are used to predict the ultimate strength and stress distribution over the stiffened panel at the moment of failure by the use of numerical analysis. The collected results are used as training and validation data for the developed machine learning model. The mesh of the numerical models is used as the input for the machine learning model.

The second part of the research is dedicated to developing a machine learning model that can predict the ultimate strength and stress distribution over the stiffened panel at the moment of failure. In this research, two different machine learning models are developed, which are similar for the most part. Both models use the entire mesh of a stiffened panel as input for the model. The first model outputs the ultimate strength of the stiffened panel, which is a single numerical value. The second model predicts the stresses over the entire mesh of the stiffened panel.

Both developed machine learning models are subjected to extensive testing with different data and data sizes. Overall, it can be concluded that machine learning can be considered an excellent tool to predict the ultimate strength and the stress distribution over the entire stiffened panel at the moment of failure. This statement is only valid when sufficient data is available for training to obtain stable learning of the developed model. When more data is available, the model is more likely to become well trained, and the obtained results are less dependent on the spread of the input data. The trained model can achieve accurate predictions as long as the input parameters lay within a 5% margin of the original data used to train the model and the input data is of similar to the data used for training. Outside this range, there is no guarantee that the model can predict results accurately. When results are predicted for input data past the 5% margin, the error of the predicted values rapidly increases. For a similar machine learning model with a similar dataset for training, the recommendation is to have at least 4000 training examples with a good spread in geometrical parameters to obtain stable learning. When data becomes more complex, for example, due to the introduction of more geometrical parameters, it is expected that an increase of the dataset, which will be used to train the machine learning model, is required. Besides the obtained results, the performed research creates multiple possibilities for further research.

# Nomenclature

| | | |
|---|---|---|
| $[K]$ | Global tangent stiffness matrix | $-$ |
| $[k_i]$ | i$^{th}$ element tangent stiffeness matrix | $-$ |
| $[K_\sigma]$ | Global stress stiffness matrix | $-$ |
| $\beta$ | Plate slenderness coefficient | $-$ |
| $\epsilon, \epsilon_{ii}$ | Strain, ii-directional strain in x, y, z-direction | $-$ |
| $\gamma_{ij}$ | Shear strain in ij-direction | $-$ |
| $\hat{y}_i$ | Predicted value | $-$ |
| $\lambda$ | Column slenderness parameter | $m^{-1}$ |
| $\lambda_i$ | Eigenvalue of the i$^{th}$ buckling mode | $-$ |
| $\nu$ | Poisson ratio | $-$ |
| $\phi$ | Stress function | $-$ |
| $\rho$ | Radius of gyration | $m$ |
| $\rho_p$ | Pearson correlation coefficient | $-$ |
| $\rho_w$ | Water density | $kg \cdot m^{-3}$ |
| $\sigma, \sigma_{ii}$ | Stress, ii-directional stress in x,y,z-direction | $Pa$ |
| $\sigma_u$ | Ultimate strength | $Pa$ |
| $\sigma_{cr}$ | Critical buckling stress | $Pa$ |
| $\sigma_{i,min}, \sigma_{i,max}$ | Minimum and maximum stress in i-direction | $Pa$ |
| $\sigma_{rcx}, \sigma_{rcy}$ | Compressive residual stress in x- and y-direction, respectively | $Pa$ |
| $\sigma_{rex}, \sigma_{rey}$ | Residual stress correction stress in x- and y-direction, respectively | $Pa$ |
| $\sigma_{rsx}^*$ | Danielson compressive residuals stress correction | $Pa$ |
| $\sigma_{rs}$ | Residual stress | $Pa$ |
| $\sigma_{rtx}, \sigma_{rty}$ | Tensile residual stress in x- and y-direction, respectively | $Pa$ |
| $\sigma_{std}$ | Standard deviation | $-$ |
| $\sigma_{VM}$ | Von Mises stresses | $Pa$ |
| $\sigma_{xav}$ | Averaged stress in x-direction | $Pa$ |
| $\sigma_{xE}$ | Elastic buckling stress | $Pa$ |
| $\sigma_{xu}, \sigma_{yu}$ | Ultimate strength in x- and y-direction | $Pa$ |
| $\sigma_y$ | Material yield strength | $Pa$ |
| $\tau_{ij}$ | Shear stress in ij-direction | $Pa$ |

| | | |
|---|---|---|
| $\theta_i$ | Rotational boundary condition around the i-axis | $-$ |
| $\zeta_{\lambda,min}$ | Initial deflection scaling factor | $-$ |
| $\{\psi_i\}$ | Eigenvector of the i$^{th}$ buckling mode | $-$ |
| $\{F\}$ | Global force vector | $-$ |
| $\{F^a\}$ | Global applied force vector | $-$ |
| $\{f^a\}$ | i$^{th}$ element applied force vector | $-$ |
| $\{F^r\}$ | Global internal force vector | $-$ |
| $\{f^r\}$ | i$^{th}$ element internal force vector | $-$ |
| $\{f_i\}$ | i$^{th}$ element force vector | $-$ |
| $\{u\}$ | Global displacement vector | $-$ |
| $\{u_i\}$ | i$^{th}$ element displacement vector | $-$ |
| $a$ | Stiffened panel length | $m$ |
| $A_m$ | Buckling amplitude for plates | $m$ |
| $a_t$ | Breadth of tensile residual stress in y-direction | $m$ |
| $A_{mn}$ | Initial deflection amplitude for plates | $m$ |
| $B$ | Stiffened panel width | $m$ |
| $b$ | Spacing between stiffeners | $m$ |
| $b_f$ | Width of the flange | $m$ |
| $b_i$ | Bias term of the neural network | $-$ |
| $b_t$ | Breadth of tensile residual stress in x-direction | $m$ |
| $D_x, D_y, H$ | Directional flexural rigidities | $Pa \cdot m^4$ |
| $E, E_i$ | Young's modulus, modulus of elasticity | $Pa$ |
| $E_t$ | Tangent modulus | $Pa$ |
| $F$ | Filter size | $-$ |
| $g$ | Gravitational constant | $m \cdot s^{-2}$ |
| $G_{ij}$ | Elastic shear modulus | $Pa$ |
| $h$ | Waterdepth | $m$ |
| $h_w$ | Height of the web | $m$ |
| $I$ | Moment of Inertia | $m^4$ |
| $I_c$ | Input of the convolutional layer | $-$ |
| $K$ | Kernel matrix | $-$ |
| $k$ | Residual stress correction factor | $-$ |
| $L$ | Length | $m$ |
| $m$ | Longitudinal number of buckling halve waves | $-$ |

| | | |
|---|---|---|
| $n$ | Transverse number of buckling halve waves | $-$ |
| $n_d$ | Number of datapoints in a dataset | $-$ |
| $n_s$ | Number of stiffeners | $-$ |
| $P$ | Compressive Force | $N$ |
| $p$ | Hydrostatic pressure | $Pa$ |
| $P_0$ | Amount of required zero-padding | $-$ |
| $P_E$ | Euler buckling load | $N$ |
| $P_{cr}$ | Critical buckling load | $N$ |
| $R, R_i$ | Nodal receptive field | $-$ |
| $S, S_i$ | Strides of the operation | $-$ |
| $t$ | Material thickness | $m$ |
| $t_f$ | Flange thickness | $m$ |
| $t_p$ | Plate thickness | $m$ |
| $t_w$ | Web thickness | $m$ |
| $u, v, w$ | Dispalacement in repsectively x,y,z-direction | $m$ |
| $u_i$ | Displacement boundary condition in i-direction | $-$ |
| $w$ | Deflection | $m$ |
| $w_0$ | Initial deflection for plates | $m$ |
| $w_{ij}$ | Nodal weight of the neural network | $-$ |
| $w_{o,i}$ | Initial deflection of i-th buckling mode | $m$ |
| $w_{oc}$ | Column-type initial deflection | $m$ |
| $w_{opl}$ | Initial deflection of the plating between stiffeners | $m$ |
| $w_{os}$ | Stiffener sideways initial deflection | $m$ |
| $y_i$ | Real observed value | $-$ |

# List of Figures

# List of Tables

# I

# Research and Theoretical Introduction

# 1
# Introduction

The first development of ships bigger than 300 meter is dated back to the 1960s. Since then, the development of bigger, more efficient vessels continued, pushing the designs towards the limits of their strength. Sometimes, structures are pushed beyond their limits with the possibility of significant negative economic and environmental impact or, in the worst case, impact on human life. As an example, back in 2013, the MOL Comfort, a 316-meter long container vessel, suffered from buckling, followed by a major collapse in the bottom hull of the ship resulting in the ship breaking into two parts. Salvage operations failed, resulting in a loss of over three thousand containers and an equal number of tons of marine diesel oil spillage [1]. The vessel was new, built in 2008, making it explicitly clear why the development of accurate methods and models is still required to predict whether or not a design is able to withstand the expected loads during its operations.

Most of the newly developed models are based on Finite Element Analysis, from now on called FEA. Nowadays, many classification societies oblige the use of FEA models for strength prediction in marine structures and provide engineers with a set of rules and guidelines to perform those analyses [2]. In the last decade, Machine Learning, from now on called ML, gained significant interest in the field of applied science. The reason for this is mainly due to the excellent performance of ML on complex problems [3]. ML also made its introduction in structural design, but the amount of research regarding the scalability and generalizability of ML within structural design is limited. This report investigates the application, scalability, and generalizability of ML to predict the ultimate strength of stiffened panels. Stiffened panels are considered one of the main structural elements of shipbuilding. Before going into the report's details, a short motivation for this research will be given in section section 1.1. Afterward, the main objective of this research will be elaborated, followed by a section providing the report's general outline, respectively section 1.2 and section 1.3.

## 1.1. Motivation

In structural design, the classical methods for design were long based on Allowable Stress Design (ASD) methods. This method depends on loads and stresses based on the yield strength of the material. This method gives no guarantee on the safety factor since the real ultimate strength of the construction is not known. Nowadays, Limit State Design (LSD) is broadly accepted as the primary approach for structural safety calculations [4]. Limit states are defined as follows:

*"A condition under which a particular structural component or an entire structural system fails to perform its designated function"* [5]

LSD in shipbuilding consists of four limit states, of which one is the Ultimate Limit State (ULS). The ULS is determined by structural failure, for example, structural collapse [6]. The other limit states are based on serviceability, fatigue, and accidents, which will not be further discussed in this research. In ships, stiffened panels are subjected to significant compressive loads during its operating lifetime, predominantly in-plane compressive loads. Extensive buckling of a stiffened plate can leave the stiffened plate with little remaining stiffness, which may result in collapse and thus total failure of the structure. For this reason, buckling is considered one of the failure modes within the ULS design of ships. Therefore, it is important to be able to predict the ultimate strength of stiffened panels and preferably large structures with reasonable accuracy. Realistic buckling results are often related to complex non-linear calculations, which can be performed by most commercial available FEA software. FEA produces reliable results if models are correctly simplified with the right boundary conditions. However, this requires significant runtime and computing power for large complex models [7].

An alternative for accurate and faster models might be developed using Machine Learning (ML). The goal of ML can be considered as follows:

*"The goal of machine learning is to program computers to use example data or past experience to solve a given problem"* [8]

ML has proven itself as a good alternative for many tasks in a wide variety of applications. Currently, the application of ML in structural engineering problems is limited. However, more and more research is being done on the combination of ML and structural engineering [3]. ML is especially interesting as an addition or partial alternative for models that contain significant non-linearities, which are difficult to describe with simple equations within analytical models. As mentioned before, numerical models often form the solution to this problem, but those models are often a trade-off between accuracy and computational power. Most numerical models are based on a mesh, a subdivision of the structure into small finite elements. In most cases, more elements in the mesh will give a higher accuracy, but the use of more elements requires more equations to be solved, thus increasing the computation time and amount of data per structural model [9]. ML might form the bridge between accuracy and computational time, which are now conflicting characteristics in structural engineering models. One of the drawbacks of ML's application within the field of structural design is the amount of data required to get acceptable performance. A large number of data is not something widely available for many structural engineering problems. A structural engineer might have access to a dataset containing several hundreds of data points, while in many disciplines where ML is widely adopted, significantly larger quantities of data are available. This research will look into ML as a suitable alternative for FEA to predict multiple failure modes in stiffened panels. Also, the scalability and generalizability of the ML will be investigated. The next section, section 1.2, will describe the goal of the research in detail with all the related sub-questions.

## 1.2. Research Goal

This research considers the application of machine learning to predict structural failure for multiple buckling modes in stiffened panels. From the introduction, the following research question arises:

*Under what conditions is it possible to predict buckling and plasticity for a meshed stiffened panel making use of machine learning?*

Several sub-questions have been defined to support the answer to the main research question:

1. *Which range of geometric parameters covers a comprehensive set used in shipbuilding, and captures all different types of buckling/local failure?* - Teaching the algorithm to predict failure of structures that will never be used will not have added value to the model. Therefore, it is important to obtain a representative set of data samples.

2. *Which type of ML-model is suitable to predict local structural failure? Also, which type of training algorithm is efficient to train this ML-model?* - ML is a broad subject, and many different styles of models exist. Not every model excels in the same tasks. Therefore, appropriate model selection is essential.

3. *How can the ML-model be trained to determine the ultimate strength of the stiffened panel without the ML-model knowing how it will fail?* - Different modes of buckling can occur in a stiffened panel based on the geometry, imperfections, and material properties. It is import to determine if the model can learn to predict the ultimate strength based on only the input parameters.

4. *When is the ML-model fully converged, and what is the minimal amount of training data needed for acceptable convergence?* - When are the result of the model accepted, or when is decided to train the model for longer to obtain even better results? The amount of available data is often limited to structural engineers. Therefore, it is essential to know how much data is required to obtain acceptable results.
5. *Is the trained ML-model able to predict results outside its training scope correctly, so-called 'scalability' and 'generalizability'. If so, to what level of extrapolation are results considered useful?* - Generally, if something is learned, we can still perform tasks that are slightly different, but what happens if the tasks become too different from the initial tasks that we used to learn? To what extent are we still able to perform the task with success?.

The questions above will be answered throughout the report. The conclusions and recommendations will reflect on the both the research question and its sub-questions described.

## 1.3. Outline of the Report

From the research goal, it becomes clear that this report will consist of several parts. Part I of the report will start with some fundamental theory on both buckling and machine learning, explained in chapter 2, supporting the reader in understanding the report better. This chapter is followed by a literature review in chapter 3.

After a first introduction to the topic, the reader will find Part II which describes all aspects of the data generation. The first chapter, chapter 4, introduces the reader to the actual stiffened panel model and its loading conditions. Next, the analytical model used to acquire a representative set of parameters for the stiffened panel is described in chapter 5. The last chapter of this part contains the description of the numerical model that is used to obtain the output data for the ML-model, chapter 6.

Part III of the report explains both developed ML-models. The ML-model that is used to predict if structural failure will occur is described in chapter 7. The next chapter, chapter 8, will describe the ML-model that is used to predict the localized stress distribution over the stiffened panel at the ultimate strength. Both chapters will described the scalability and generalizability for the ddeveloped models

In Part IV, the report will be completed with the conclusion and the recommendations for further research in chapter 9 and chapter 10, respectively.

# 2

# Fundamental Theory

It is expected that some readers will have no prior experience with either buckling or machine learning. Therefore, this chapter will elaborate on the theoretical fundamentals of both topics. The theory described in this chapter is considered prior knowledge throughout the report. It is expected that the reader has some background related to physics.

In section 2.1 a basic introduction to buckling will be given, starting with the very basics working towards plate buckling, nonlinearities and Finite Element Methods (FEM). The second part of this chapter, section 2.2, will give an introduction to the basics of machine learning, especially related to Convolutional Neural Networks (CNNs).

## 2.1. Buckling

This section will give an introduction to buckling, which forms the basis for a better understanding of the analysis performed in chapter 5 and chapter 6. The following definition could represent buckling:

*Buckling is considered a significant increase in lateral deflection caused by the application of axial compressive forces on thin structures.*

As previously mentioned in section 1.1, after severe buckling, a structure may lose a significant amount of its stiffness or strength, resulting in structural failure when loading continues. The understanding of this phenomenon is an essential factor in ensuring structural safety. Two main types of buckling analysis are found: linear and nonlinear. Linear models adopt a linear relationship between stress and strain. Also, linear geometrical behavior is adopted. They are easily applicable and provide a quick result but at the cost of accuracy. Nonlinear models often deliver good accuracy on the real ultimate strength of a structure. Nonlinear models have increased complexity and require more computational power than linear models.

Several factors can have a significant impact on the ultimate strength of columns and panels. These factors will be discussed throughout the sections. Only the effects that are created during construction will be discussed. Effects like corrosion and cracking are neglected.

The first introduction to cloumn buckling is given in section 2.1.1. The buckling theory will be extended to plate buckling theory in section 2.1.2. In the next section, section 2.1.3, the influence of residual stress on the ultimate strength will be discussed. The initial deflection of a structure can also negatively influence the ultimate strength of a structure. The initial deflection will be discussed in section 2.1.4. The next section, section 2.1.5, will describe the use of numerical models. Eigenvalue buckling analysis and quasi-static buckling analysis will be discussed in section 2.1.6 and section 2.1.7, respectively. If the reader is familiar with buckling it is recommended these skip these sections and continue reading in section 2.2.1.

### 2.1.1. Euler Buckling

This section will start with the fundaments of linear buckling, Euler buckling, also called column buckling. Euler buckling is the most basic description of column buckling, not taking into account any form of nonlinearities like initial deflection, plasticity, and eccentricity. Plasticity is deformation that is permanent even after unloading the structure, elastic deformations are non-permanent deformations. A column without those nonlinearities is also called an ideal column. Euler buckling only adopts the linear part of material behavior. The material is considered homogeneous and isotropic, and deformations are considered small. The stress-strain relation is given by eq. (2.1). Stress ($\sigma$) is linearly related to the strain ($\epsilon$) by the Young's Modulus ($E$).

$$\epsilon = \frac{1}{E}\sigma \tag{2.1}$$

In the hull of ships, it is often assumed that the boundary conditions are simply supported. The reason for this will be further explained in section 4.1. Therefore, a simply supported column will be assumed in this section, as can be seen in fig. 2.1.

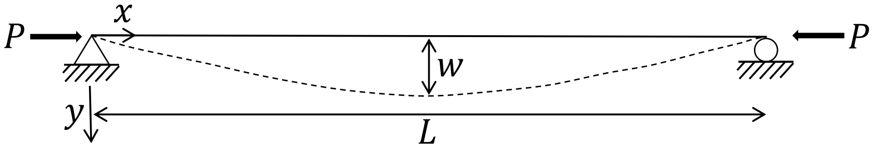

Figure 2.1: Representation of a simply supported beam. $w$ is the beam's deflection. P is the applied compressive force.

In column buckling, small deflections and rotations are assumed. In the column, internal and external bending moments are present. Those moments can be used to write an equilibrium of the bending moments on the column. The moment equilibrium can be rewritten to the homogeneous second-order linear differential equation, eq. (2.2). The general solution for the differential equation is given in eq. (2.3).

$$\frac{d^2w}{dx^2} + \left(\frac{P}{EI}\right)w = 0 \tag{2.2}$$

$$w(x) = C_1 \sin\left(\sqrt{\frac{P}{EI}}x\right) + C_2 \cos\left(\sqrt{\frac{P}{EI}}x\right) \tag{2.3}$$

Simply supported boundary conditions impose no deflection ($w = 0$), and no bending moment ($d^2w/dx^2 = 0$) at the support. The constants in the differential equation can be found with the application of $w(x = L) = 0$ and $w(x = 0) = 0$. Constant $C_2$ becomes zero eliminating the second term from the differential equation's right hand side, giving a non-trivial solution in the form of eq. (2.4).

$$\sqrt{\frac{P}{EI}}L = n\pi \tag{2.4}$$

Physical mechanisms always prefer a state that requires the least energy. When compressing a column, it will tend to buckle in a half-sinusoidal shape since this requires the least energy, as can be seen in fig. 2.1. The number of half waves is described by $n$. The critical buckling load can then be obtained by rewriting eq. (2.4) with $n = 1$ to eq. (2.5).

$$P_{cr} = P_E = \frac{\pi^2 EI}{L^2} \tag{2.5}$$

The radius of gyration ($\rho = \sqrt{I/A}$), can be used to transform the Euler buckling load to a critical stress equation, eq. (2.5).

$$\sigma_{cr} = \frac{P_{cr}}{A} = \frac{\pi^2 EI}{L^2}\frac{\rho^2}{I} = \frac{\pi^2 E\rho^2}{L^2} \tag{2.6}$$

The Euler buckling load can be rewritten with the column slenderness coefficient ($\lambda$) to obtain a ratio between the critical Euler stress and the structure's yield strength ($\sigma_y$). The column slenderness coefficient is based on the yield strength of the material, the Young'ss modulus, and the radius of gyration ($\rho$), and can be seen in eq. (2.7). When squaring the radius of gyration ($\rho^2$), it can be substituted in the Euler buckling stress equation, eq. (2.6), to obtain an equation relating the Euler buckling stress to the yield strength and the slenderness coefficient of the construction, eq. (2.8).

$$\lambda = \frac{1}{\pi\rho}\sqrt{\frac{\sigma_y}{E}} \tag{2.7}$$

$$\sigma_{cr} = \frac{\pi^2 E \rho^2}{L^2} = \frac{\pi^2 E}{L^2}\frac{L^2 \sigma_y}{\pi^2 \lambda^2 E} \rightarrow \frac{\sigma_{cr}}{\sigma_y} = \frac{1}{\lambda^2} \tag{2.8}$$

Similarly, it is possible to obtain the Euler buckling load for fixed supports, which also considers constrained rotations ($dw/dx = 0$) as an additional boundary condition. The use of fixed boundary conditions will not be used throughout this report, therefore, this will not be further explained. Euler buckling is only effective for perfect structural elements. A real structure is never considered perfect, but the Euler equation forms the foundation for multiple analytical models that take into account effects as plasticity, initial deformation, and eccentricity. The most well-known models are the Johnson-Ostenfeld equation and the Perry-Robertson equation. Other models are available like the Rankine models, but they are not widely adopted. Johnson-Ostenfeld adds plasticity to the equation. Perry-Robertson includes eccentricity and initial deflection. The importance of plasticity and initial deflection will be described in section 2.1.3 and section 2.1.4.

### 2.1.2. Plate Buckling

When looking at plates, the 2-D cases of column buckling turns into a 3-D case. In the 3-D case, the constitutive relation described in eq. (2.1), need to be extended by incorporating the Poisson effect ($\nu$). The Poisson effect implies that a positive strain will cause a negative strain in both orthogonal and lateral direction. In case of thin plates under axial compression, we can consider in-plane stress conditions: $\sigma_{zz} = \tau_{yz} = \tau_{zx} = 0$. This reduces the stress-strain relations for plates to eq. (2.9).

$$\begin{bmatrix} \epsilon_{xx} \\ \epsilon_{yy} \\ \gamma_{xy} \end{bmatrix} = \frac{1}{E}\begin{bmatrix} 1 & -\nu & 0 \\ -\nu & 1 & 0 \\ 0 & 0 & 2\,(1+\nu) \end{bmatrix}\begin{bmatrix} \sigma_{xx} \\ \sigma_{yy} \\ \tau_{xy} \end{bmatrix} \tag{2.9}$$

In this section, it is assumed that plates are simply supported. This way, the buckling shape of plates will have a sinusoidal shape in the direction of the length ($a$), called the longitudinal direction, and the width ($b$), called the transverse direction, of the plate when subjected to uni-axial compression, see fig. 2.2. A second component over the y-axis will be added to eq. (2.3), resulting in the eq. (2.10). From this equation, it can be seen that a sinusoidal shape will occur in both directions. The parameters $m$ and $n$ are the buckling halve-wave numbers in the plate's longitudinal and transverse direction, respectively. Parameter $A_m$ is the buckling amplitude.

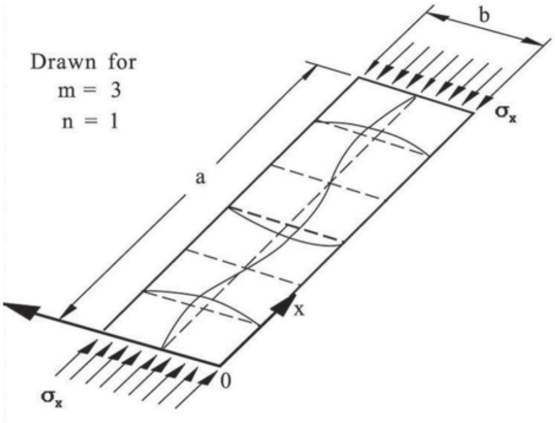

Figure 2.2: Buckling halve waves in both x- and y-direction. The value of $m$ represents the number of half waves in the longitudinal direction ($a$), $n$ represents the number half waves in the transverse direction ($b$). In this figure, the plate is drawn for $m = 3$ and $n = 1$. Image taken from [10].

$$w = A_m \sin\left(\frac{m\pi x}{a}\right)\sin\left(\frac{n\pi y}{b}\right) \tag{2.10}$$

When subjected to longitudinal uni-axial compression, the stress strain relations will change. The equations from eq. (2.9), will change to the set in eq. (2.11).

$$\begin{cases} \epsilon_{xx} = \dfrac{1}{E}\sigma_{xx} \\ \epsilon_{yy} = -\dfrac{\nu}{E}\sigma_{xx} \end{cases} \tag{2.11}$$

By applying the same principles as described for Euler buckling, the elastic buckling stress of a plate can be determined. Again, by setting the plate's internal and external bending moments equal to each other, one can solve for critical stress by substituting the displacement equation, eq. (2.10), in the equilibrium equation. This will result in equation eq. (2.12).

$$\sigma_{xE} = \frac{\pi^2 a^2 D \left(\frac{m^2}{a^2} + \frac{n^2}{b^2}\right)^2}{tm^2} \rightarrow \sigma_{xE} = k\frac{\pi^2 D}{b^2 t}; k = \left(\frac{mb}{a} + \frac{a}{mb}\right)^2 \tag{2.12}$$

Parameter $D$ is the flexural rigidity of the plate, which depends on the Young's modulus, Poisson ratio and the thickness of the plate ($t$). The flexural rigidity is described by eq. (2.13).

$$D = \frac{Et^3}{12(1-\nu^2)} \tag{2.13}$$

The lowest value for the elastic buckling load for uni-axial compressed plates will be obtained by selecting $n = 1$, which is one buckling half-wave in the transverse direction of the plate. With $n = 1$, eq. (2.12) can be rewritten to eq. (2.14).

$$\sigma_{xE,1} = \frac{\pi^2 D}{a^2 t}\left(m + \frac{1}{m}\left(\frac{a}{b}\right)^2\right)^2 \tag{2.14}$$

For uni-axial compressed plates, the value of $m$ can be determined by the aspect ratio of the plate, as described in eq. (2.15).

$$\frac{a}{b} \leq \sqrt{m\,(m+1)} \tag{2.15}$$

This section provides information based on the theory given in lecture slides from MIT [11] and the books of Timoshenko and Gere [12] and Hughes and Paik [7]. The previously discussed section, section 2.1.1 and section 2.1.2, form the introduction to the reader who has no prior experience with buckling. The equations and derivations described are limited but should form a feeling for what is happening when columns and plates buckle. If the reader is more interested in buckling analysis and its derivations, the reader can consult one of the many available books about this topic.

### 2.1.3. Residual Stress

The importance of incorporating plasticity within ultimate strength models is related to the residual stress in structures. Residual stress ($\sigma_{rs}$) is internal stress in the structure that is always present, even in the unloaded state. For stiffened plates, there are two main reasons for residual stress within the structure. Both reasons are related to thermal gradients during the production stage.

The first reason is the hot-rolling of plates/stiffeners during fabrication. During the process of cooling, the temperature gradients are not the same throughout the material. Hot-rolled T-stiffeners tend to cool faster at the edges of the flanges, creating residual stresses [13]. The geometry of a T-stiffener is shown in fig. 4.2. The plate's edges tend to cool more rapidly than the center of the plate, resulting in compressive residual stress on the edges and tension in the middle of the plate. Compressive residual stresses due to hot-rolling can be close to one-third of the yield strength of the parent material [14].

The second cause for residual stress is welding. During welding, the material is heated until it becomes fully plastic. Due to the uneven cooling after welding, tensile residual stress will occur at the weld seam and compressive residual stresses in the middle of the plate, as shown in fig. 2.3. The magnitude of the tensile stress can be close to the yield strength of the parent material. The physical mechanism that happens in the material during cooling will not add to the understanding of the importance of plasticity and will therefore not be discussed in this report.

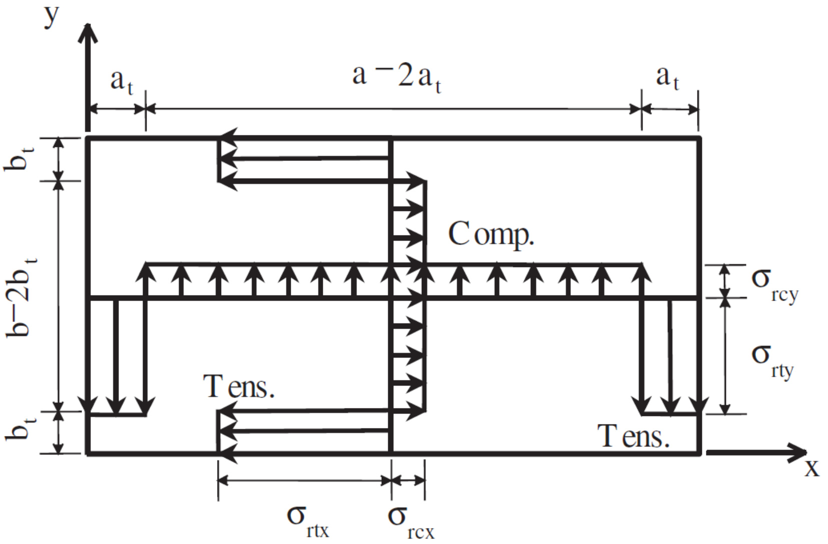

Figure 2.3: Residual stress developed in a plate due to uneven cooling after welding around all the edges. Around the weld-seam, tensile residual stress will develop close to the yield strength, $\sigma_y$ of the parent material. Image taken from [10].

As mentioned before, buckling is caused by compressive forces on thin structures. From now on, compressive forces are considered positive, and tensile forces are considered negative values. If we subject a welded plate to uni-axial compression in the longitudinal direction, the force applied will add up to the compressive force in the center of the plate, $\sigma_y = \sigma + \sigma_{rs}$, causing plasticity in the material before the Euler critical buckling load, $\sigma < \sigma_y$, has been reached. This behavior shows the importance of incorporating plasticity into the ultimate strength calculations. Theoretically, welding residual stress can also add to the strength of the material. Welding residual stress can prevent plasticity near the weld seam of the material due to the tensile residual stress when loaded by compressive force in the longitudinal direction, $\sigma_y = \sigma - \sigma_{rs}$.

Plasticity is incorporated into eq. (2.8) by adopting elastic-perfectly plastic material properties [14]. Past the linear elastic stress-strain relation, 0-A in fig. 2.4, the material starts to behave nonlinearly. Beyond the yield strength, there is a moment of purely plastic strain, also called yield plateau, as seen in segment A-B. Eventually, strain-hardening will occur until the ultimate strength ($\sigma_u$) has been reached at point C. Strain-hardening is the phenomenon where during plastic deformation, material dislocations start to move, and new dislocations are created within the crystal structure of the material, increasing the stress required for a specific elongation. Strain hardening is difficult to model. Therefore, in analytical models and even numerical models, a bi-linear isotropic material is assumed. The nonlinear part B-C will be approximated with a tangent modulus $E_t$, which is also displayed in fig. 2.4. It is often assumed that the tangent modulus is zero, which would mean that the material is considered elastic-perfectly plastic. Yield flow starts beyond the yield strength without the further increase due to elongation.

The Johnson-Ostenfeld equation takes plasticity into account with a plasticity correction, which is often assumed to start when the elastic buckling stress in eq. (2.5) or eq. (2.12) is past half of the yield strength. This is shown in eq. (2.16) [14].

$$\sigma_{xu} = \begin{cases} \sigma_{xE} & \text{for } \sigma_{xE} \leq 0.5\sigma_y \\ \sigma_y\left(1 - \frac{\sigma_y}{4\sigma_{xE}}\right) & \text{for } \sigma_{xE} > 0.5\sigma_y \end{cases} \tag{2.16}$$

The effect of residual stress can also be added to equation eq. (2.14) by adding a residual stress correction ($\sigma_{rex}$) which is calculated by eq. (2.18a). This will results in eq. (2.17). This correction factor

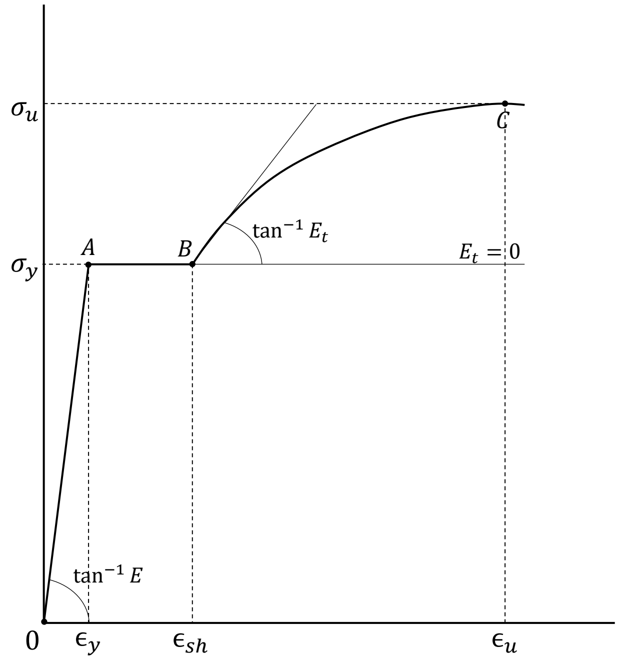

Figure 2.4: Stress-strain diagram. 0-A: showing the linear behaviour until the yield strength. A-B: Showing plastic material flow, also called yield plateau. B-C: nonlinear strain-hardening.

is determined by both the compressive and tensile residual stress over the plating. These equations display the effect of residual stress in the longitudinal directions. Stiffened panels are welded on every side of the plating. Therefore, it is also important to introduce welding residual stress in the transverse direction. The correction factor in y-direction is given by eq. (2.18b).

$$\sigma_{xE,1} = \frac{\pi^2 D}{a^2 t}\left(m + \frac{1}{m}\left(\frac{a}{b}\right)^2\right)^2 - \sigma_{rex} \tag{2.17}$$

$$\sigma_{rex} = \sigma_{rcx} + \frac{2}{b}(\sigma_{rtx} - \sigma_{rcx})\left(b_t - \frac{b}{2\pi}\sin\frac{2\pi b_t}{b}\right) \tag{2.18a}$$

$$\sigma_{rey} = \sigma_{rcy} + \frac{2}{b}(\sigma_{rty} - \sigma_{rcy})\left(a_t - \frac{a}{2\pi}\sin\frac{2\pi a_t}{a}\right) \tag{2.18b}$$

In these equations $\sigma_{rcx}$ and $\sigma_{rtx}$ are the compressive residual stress and the tensile residual stress in x-direction, respectively, as given in fig. 2.3. The parameters $\sigma_{rcy}$ and $\sigma_{rty}$ are then the compressive residual stress and the tensile residual stress in the y-direction. As mentioned before, the tensile residual stress is close to the yield strength of the parent material for most steels ($\sigma_{rtx} \cong \sigma_y$). The compressive residual stress is often taken as eq. (2.19a) in the x-direction and eq. (2.19b) in the y-direction. These equations define the residual stress as a fraction of the yield strength of the parent material. The levels determine the amount of residual stress present in the structure. Sometimes excessive residual stress can be present in a structure as is noted in the experimental study of Smith et al. [15]. Therefore, multiple levels of residual stress are defined.

$$\sigma_{rcx} = \begin{cases} -0.05\sigma_y & \text{for a slight level} \\ -0.15\sigma_y & \text{for an average level} \\ -0.3\sigma_y & \text{for a severe level} \end{cases} \tag{2.19a}$$

$$\sigma_{rcy} = k\frac{b}{a}\sigma_{rcx} \tag{2.19b}$$

Where $k$ is a correction factor based on the yield strength of the parent material. The values of $k$ are presented in table 2.1. For other material yield stress factors, the factor can be determined by making use of interpolation. Parameters $b_t$ and $a_t$ are the width of the residual tensile stress zones, which are approximated by eq. (2.20a) and eq. (2.20b). This approximation is based on force balance.

Table 2.1: k-material factor according to the international association of classification societies (IACS). By interpolating it is possible to obtain the k-material factor for other material yield strengths.

| $\sigma_y$ (MPa) | $k$-factor (-) |
|---|---|
| 235 | 1.00 |
| 315 | 0.78 |
| 355 | 0.72 |
| 390 | 0.66 |
| 460 | 0.62 |

$$(b - 2b_t)\sigma_{rcx} = -2b_t\sigma_{rtx} \rightarrow b_t = \frac{b}{2}\frac{\sigma_{rcx}}{\sigma_{rcx} - \sigma_{rtx}} \tag{2.20a}$$

$$(a - 2a_t)\sigma_{rcy} = -2a_t\sigma_{rty} \rightarrow a_t = \frac{a}{2}\frac{\sigma_{rcy}}{\sigma_{rcy} - \sigma_{rty}} \tag{2.20b}$$

The description is given for residual stress, and its effect on the elastic buckling strength in eq. (2.17) is valid for compressive forces in the longitudinal direction. The elastic buckling strength can be obtained for compressive force over the transverse direction in a similar manner, which will not be further discussed.

This subsection makes clear the importance of incorporating the residual stress in the ultimate strength analysis and how it negatively can influence the ultimate strength. It also is explained how residual stress can be estimated in plates welded on the edges.

### 2.1.4. Initial Deflection

Another important aspect related to the ultimate strength of structures is the initial deflection of the structure. In reality, a structure is never perfectly flat or straight because deformations in the structure might occur during the handling or processing of the materials in the building process. One of the most critical factors causing initial deformations is the welding of the materials. Due to the heating and cooling, the material deforms. In this process, the material does not fully return to its original state creating initial deflection in the material. During the compressive force application, this initial deflection will add up to the deformation caused by compressive force in eq. (2.2), $w \rightarrow w + w_0$. This increase in deformation will cause the material to buckle faster, thus lowering the ultimate strength of the structure.

The shape of the initial deflection is, in reality, complex and challenging to describe. It is often assumed that the initial deflection will be similar to the first element in a Fourier series over both axis, as described in eq. (2.21) [12]. The parameter $w_0$ is the initial deflection, $A_{0mn}$ the amplitude.

$$w_0 = \sum_{m=1}^{M}\sum_{n=1}^{N} A_{0mn}\sin\left(\frac{m\pi x}{a}\right)\sin\left(\frac{n\pi y}{b}\right) \tag{2.21}$$

### 2.1.5. Numerical Analysis

For simple structures like plates and beams, analytical equations can form a quick and easy usable first estimate. For more accurate estimates, geometry and material nonlinearities are essential to take into account. The application of nonlinearities is often difficult with the use of analytical models for more complex structures. Therefore, numerical methods like Finite Element Methods (FEM) are often used to obtain accurate buckling and ultimate strength assessments. There are other methods available, like Element Free Galerkin methods (EFG). These are less often used in buckling analysis than FEM and will not be further considered in this research.

In FEM, a structure is represented by making a geometry. This geometry will then be divided into small finite elements, together called a mesh. This process is called discretization of the continuum. Elements can either be 1-D elements (lines), 2-D elements (shells), or 3-D elements (solids). Every element has a certain amount of points, called nodes, distributed over the edges or the surface of the element. For those nodes, the Degrees of Freedom (DoFs) are described. In this way, it is possible to create a set of equations related to the finite elements. For the entire structure, FEM uses the global equation set shown in eq. (2.22). For every i$^{th}$ element, this equation is written as eq. (2.23).

$$\{F\} = [K]\{u\} \rightarrow \{F^a\} - \{F^r\} = [K]\{u\} \tag{2.22}$$

$$\{f_i\} = [k_i]\{u_i\} \rightarrow \{f_i^a\} - \{f_i^r\} = [k_i]\{u_i\} \tag{2.23}$$

In those equations, $\{F\}$ and $\{f_i\}$ are the load vectors on the structure. The load vector is separated in an applied force vector $\{F^a\}$ and the internal restoring force vector $\{F^r\}$. Matrices $[K]$ and $[k_i]$ are the tangent stiffness matrices, describing the resistance to strain. This matrix depends on the parameters of the model, such as geometry and material properties. $\{u\}$ and $\{u_i\}$ are the displacement vectors. These equations are a basic representation of the equations solved for time-independent analysis. In FEA, the displacements are determined, which can be turned into strains and stresses. When a model is divided into more elements, a more accurate prediction is usually obtained. The use of more elements also increases the number of required computations and significantly increases the model size and the computational power required.

There are multiple methods for determining the ultimate strength with a buckling analysis. The simplest method is linear eigenvalue buckling, in which the bifurcation stress is determined. This method will be discussed in section 2.1.6. When incorporating nonlinear effects, a quasi-static analysis will often be used. With nonlinear analysis, a better approximation of the real ultimate strength can be obtained compare to eigenvalue buckling analysis. Quasi-static analysis well be discussed in section 2.1.7.

### 2.1.6. Eigenvalue Buckling Analysis

In eigenvalue buckling, the problem is solved under ideal and elastic circumstances. In eigenvalue buckling, it is also assumed that deflections are small so that small deflection theory can be used. In eigenvalue buckling, the goal is to find the bifurcation buckling point: the point that indicates the moment of instantaneous buckling. The bifurcation point is the linear elastic buckling point, which is also called Euler buckling. The name eigenvalue buckling comes from the fact that in eigenvalue buckling, the point is searched for which stiffness matrix $[K]$ becomes singular. This search is similar to searching for non-trivial solutions in an eigenvalue problem. The problem that is solved can be written as eq. (2.24).

$$([K] + \lambda_i[K_\sigma])\,\{\psi_i\} = 0 \tag{2.24}$$

Matrix $[K]$ is the previously describe stiffness matrix, which depends on the geometry and the material properties. $[K_\sigma]$ is called the stress stiffness matrix. This matrix is updated during every load step while solving and contains values related to the increase or decrease of stiffness due to the current stress state. The parameter $\lambda_i$ is an eigenvalue of the i$^{th}$ buckling mode and the force-scaling factor, which will be explained later. The vector $\{\psi_i\}$ is the buckling mode eigenvector and is a normalized displacement vector. This vector represents the displacement of the i$^{th}$ buckling mode corresponding to i$^{th}$ eigenvalue. Solving the eigenvalue problem will give the eigenvalue and the corresponding buckling modes of the structure. Within FEM, there are multiple methods available to extract those eigenvalues. Those methods will not be further discussed and can be found explained in detail in most manuals of commercial FEM software [16]. In numerical eigenvalue buckling, the eigenvectors do no represent real displacements. The displacement vector is normalized, meaning that all rotations and deflections are scaled between 0 and 1. The buckling mode related to the lowest eigenvalue represents the dominant buckling shape. The bifurcation point can be obtained by scaling the initially applied loads on the model with the lowest eigenvalue. If the lowest eigenvalue is equal to 1, the bifurcation load on the construction is found.

The eigenvalue buckling analysis is often not performed to obtain the bifurcation point of the structure, but to obtain the first elastic buckling mode shape. The first elastic buckling mode is the eigenvector $\{\psi_i\}$, which corresponds with the lowest obtained eigenvalue $\lambda_i$. This mode shape is often used as an initial deflection for a quasi-static analysis. As mentioned earlier, the eigenvector with the buckling mode is normalized, making it easy to scale to the desired initial deflection amplitude. Often, the buckling mode shape is scaled to the maximum amplitude described in the study of Smith et al. [15], or to maximum values obtained from experimental research.

### 2.1.7. Quasi-Static Buckling Analysis

In quasi-static buckling analysis, forces and displacements are incremented in small steps. When those sub-steps are small enough, the inertial effects of the structure become negligible. This way, the iterative process becomes a quasi-static analysis instead of a dynamic analysis. Often, quasi-static analysis is used, including nonlinear behavior, making use of large deflection theory. Compared to eigenvalue buckling, a non-ideal structure is assumed with initial deflections, often obtained from the first mode of the eigenvalue buckling.

$$\{F^a\} - \{F_i^r\} = [K_i]\{\Delta u_i\} \tag{2.25}$$

In a quasi-static analysis, the loads or displacements are incremented in small steps. At every load step, the nonlinear force balance between external and internal forces described in eq. (2.25) must be solved. In this equation, the displacement vector is written as $\{\Delta u_i\}$, which represents the displacement at increment $i$. An iterative process is required to solve this equation. Most analysis types make use of the Newton-Raphson method [16]. This method iteratively solves the imbalance between the externally applied forces and the internal forces. In this method, the left-hand side of eq. (2.25) will be determined to obtain a force imbalance on the right-hand side of the equation. This process is done by iteratively updating $\{\Delta u_i\}$ and $[K_i]$ to obtain a force imbalance that is considered converged. To determine if a solution is converged, it is often assumed that the difference between the externally applied and internal forces is below a certain error margin. As soon as the force imbalance is considered converged, the next displacement increment of the quasi-static analysis will be applied, and the iterative process to solve the force imbalance will be repeated. This iterative method is effective if the function to solve is monotonic. When reaching the ultimate strength of a structure, this method might become unstable and contains inaccurate results due to the large increase in deformations and rotations when assuming elastic-perfectly plastic material. Therefore, in a quasi-static buckling analysis, the arc-length method is often used.

$$\lambda\{F^a\} - \{F_i^r\} = [K_i]\{\Delta u_i\} \tag{2.26}$$

$$\Delta L = \sqrt{\{\Delta u_i\}^T\{\Delta u_i\}} \tag{2.27}$$

The arc-length method is based on eq. (2.26) [16]. The arc-length equation is similar to the Newton-Raphson equation eq. (2.25). The load factor ($\lambda$) changes every iteration over the arc defined with radius $\Delta L$. This way, the applied load vector $\{F^a\}$ becomes variable. In the arc-length method, an arc is used with the radius $\Delta L$, derived from the displacement vector $\{\Delta u_i\}$ by eq. (2.27). The arc-length method combined with the iterative solving of the Newton-Raphson method makes it possible to obtain converged results of solutions which are non-monotonic or even not continuous, which can be the case in quasi-static buckling analysis. Therefore, in this research, the arc-length method will be adopted for the quasi-static analysis.

## 2.2. Machine Learning

As mentioned in section 1.1, one can describe machine learning with the following definition:

*”The goal of machine learning is to program computers to use example data or past experience to solve a given problem”* [8]

Within machine learning, three types of main problems are defined: Unsupervised learning, supervised learning, and reinforcement learning. When for a problem only the input data is known, it is still possible to use algorithms to learn relations between the individual data points. This type of task is called unsupervised learning. If the ouput of the data is known, the algorithm can learn to predict the outcome. This problem can be either a classification task or a regression task and is called supervised learning. In both cases, the algorithm learns to find the relation between the in- and output data. For the last type of problem, there are situations where models are taught to respond to interactions with other inputs. These interactive problems are called reinforcement learning. This thesis’s subject is about predicting the failure of stiffened panels, for which an ultimate strength is required. The ultimate strength is a numerical value, so therefore it can be considered a regression problem. Since it is a numerical value, it is known what the output corresponding to the input should be. Therefore, this problem is considered supervised learning, and no further attention will be paid to unsupervised and reinforcement learning throughout this report.

nonlinear regression can be performed by Neural Networks (NNs). There are many different NN architectures developed over the last decades. First, an introduction will be given to the basic NNs and Deep Neural Networks (DNNs) in section 2.2.1. This section describes the main idea and principles behind NNs. Neural networks are the most used architecture within structural engineering in the last decade [3]. Next, an introduction will be given to Convolutional Neural Networks (CNNs) and why this architecture is different from DNNs, see section 2.2.2.

### 2.2.1. Deep Neural Networks

This section will describe the basics of NNs and DNNs, providing the inexperienced reader with an idea of what NNs are and how they can learn relations between the input and output of data. A schematic overview of a neural network is displayed in fig. 2.5. Three columns, called layers, of neurons can be observed. There are three main parts in the NN: the input layer, the output layer, and the hidden layer. The input layer has the same number of neurons as the number of input parameters of the model. A Neuron is a point in the network where different signals come together, drawn as circles in the figure. The output layer has the same size as the number of desired outputs by the designer of the network. In the middle section of the model, there are hidden layers with an arbitrary number of neurons. If there are three or more hidden layers in the network, it is classified as a DNN.

When every neuron of layer $i$ is connected with every neuron in layer $i+1$, the network is called fully connected or dense. The information transferred from a neuron in one layer to a neuron in the next layer is multiplied by a weight $w_{ij}$. A bias term $(b_j)$ will be added to the input $(x_i)$ multiplied by the weight $(w_{ij})$. The weight represents the slope of a linear function, and the bias term the intercept. All the information that arrives from layer $i$ to layer $i+1$ is summarized in the individual neurons in layer $i+1$. All operations until this moment are a linear process. Nonlinearities need to be introduced to the neural network to make sure that the network can learn more complex relations between the in- and output of the network. The summarized result in a neuron is put through an activation function $f$, which is often nonlinear. This way, the output of layer $i+1$ becomes nonlinear. This process is repeated in every single neuron throughout the network. This process is mathematically represented in eq. (2.28) for a single neuron. If this equation is extended to two layers, it becomes clear how complex nonlinear functions can be created within the neural network. This process is represented in eq. (2.29).

$$a_j = f\left(\sum_{i=1}^{N} w_{ij} x_i + b_j\right) \tag{2.28}$$

$$b_k = g\left(\sum_{j=1}^{M} w_{jk} a_j + b_k\right) \rightarrow g\left(\sum_{j=1}^{M} w_{jk} f\left(\sum_{i=1}^{N} w_{ij} x_i + b_j\right) + b_k\right) \tag{2.29}$$

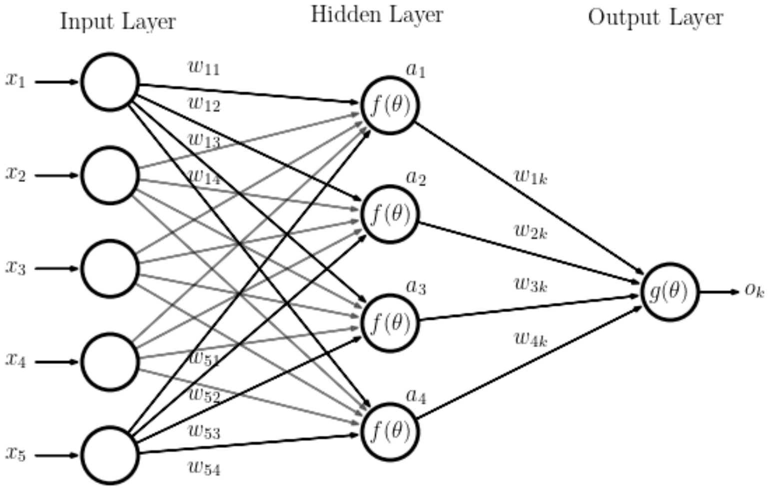

Figure 2.5: Schematic overview of a single hidden layer neural network. Neurons are represented by circles, and the lines in between the neurons represent the connection between the individual neurons. The first layer is the input layer. The middle layers of the network are called the hidden layers. The hidden layer can consist of multiple layers. The last layer is the output layer. Image taken from [17].

Equation (2.29) shows that for two consecutive layers, the nonlinear output of the first layer is again multiplied by a new weight in the second layer. Again a bias term is added. A second nonlinear function, $g$, will be applied over the already nonlinear output of the first layer. It becomes clear that by adding more hidden layers to the network, the network can predict more complex results.

It is also required to understand how these equations can predict the outcome of the input. If the ML model must correctly predict the outcome of the input, it must find the weights $(w_{ij})$ and biases $(b_j)$ such that the input data is transformed to the correct output data. This process is done by first initializing the weights and then insert the inputs into the model to see its accuracy in predicting the outcome. The error on the predictions, also called loss, will be calculated based on an error function and will then be sent back through the network, called back-propagating. This principle is why the models are often referred to as back-propagating neural networks in the literature. By back propagating the error it is possible to determine the gradients of the loss in every neuron. This gradient will then be used to change the weights and biases. Then, the data can be sent through the network to see if the obtained loss decreases. This process is repeated until the moment the model stops learning or if the desired performance is obtained. When all data is sent through the network once, it is called an epoch. Often, the amount of data is so large that it is not possible or efficient to put all the data through the network before updating the weights. In this case, the data is split into smaller groups, called batches or mini-batches. After putting a batch through the network, the weights and biases will be updated. How the created loss updates the weights and biases is determined by the optimizer that is used.

This short section should provide the reader with some basic understanding of how a NN works. The next section will introduce the CNN, which is the primary type of NN used within this research.

### 2.2.2. Convolutional Neural Networks

In the previous section, the basics of NNs are explained. In this research, a Convolutional Neural Network (CNN) is used. The principles of NNs still apply to CNNs, although the process is slightly different and more efficient for large-sized input data. For example, a mesh of a plate with 10 nodes in the plate's length and width would already have 100 points with information. If we assume that these points contain information about their coordinates, the mesh contains an x-, y-, and z-value at every node. This information indicates that there are already 300 points of data available. If this would be a basic NN with a hidden layer of five neurons, all those 300 points will be connected with the five neurons. This data will result in already 1,500 weights that have to be updated in only the first layer. For large sized data, the basic NN becomes inefficient. Another important fact is that on the plate, normally, the nodes next to each other will interact with each other. If the nodes are used as individual inputs for the

NN, the information about the interaction is lost. This loss of information is a drawback of using NNs. The interaction between individual data points is called the spatial information of data. CNN's keep this spatial information within the model, which is important for the current research [18].

This section will not provide the reader with a complete overview of all the different layers and options available within CNNs. The information that is provided is the principles that are applied within this research. Basic understanding of those principles is required to correctly understand the assumptions that will be made in chapter 7 and chapter 8. First, the main building block of CNNs will be discussed: the convolutional layer. Next, pooling layers will be explained, followed by a brief explanation of activation functions. Also, some attention will be given to optimizers and loss functions.

**Convolutional Layers** are the main building block in CNNs. The principle of multiplying the input with a weight still applies. Instead of applying a single weight to a single input parameter, in convolutional layers, the data is considered 2-D or 3-D. The example of a $10 \times 10$ mesh with Cartesian coordinates (x-, y-, z-values) as data becomes a dataset with a size of $10 \times 10 \times 3$. When more data belongs to a single point on the mesh, the individual data layers belonging to a data point are called channels. With this definition, the $10 \times 10$ data has 3 channels. In convolutional layers, a matrix of weights is used. This matrix has a size of $F \times F \times C$ and is called a filter. The 2-D layer of a single channel in the filter is called a kernel. A filter is schematized in fig. 2.6. Parameter $F$ and $C$ are the width/height of the filter and the number of channels in the input data, respectively. All the elements in the kernel are individual weights. The kernel slides over the original data with a certain step size, called the stride. At every move of the filter, the dot product is calculated between the input data at the filter's location and the weights in the filter itself. The output of this dot product delivers a new matrix, which will be summed together to a single value. A bias value will be added to the summed signal. This process is represented by eq. (2.30) and is mathematically seen as a cross-correlation instead of a convolution; however, it is often referred to as a convolution. During the filter's sliding over the input data, the weights in the filter stay the same. After the filter is applied to the entire input, a 2-D matrix is obtained. In convolutional layers, often multiple different filters are used to obtain more information from the data. The result of all those filters together produce a new 3-D matrix. In convolutional layers, the obtained matrices are stacked.

$$I_c(x,y) = \left( \sum_{i=0}^{n} \sum_{j=0}^{m} K(i,j) I_c(x+i, y+j) \right) + b_{ij} \tag{2.30}$$

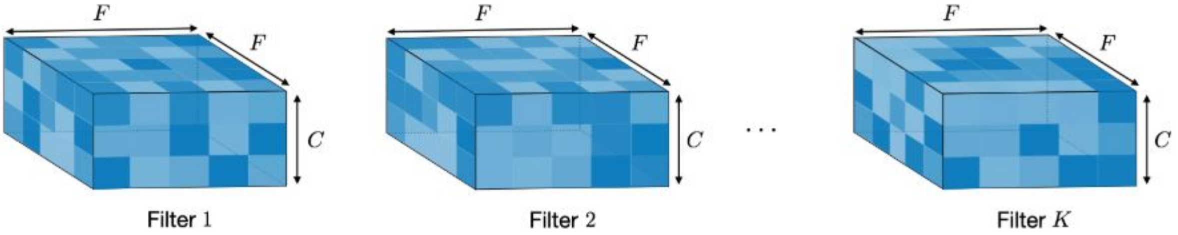

Figure 2.6: Schematic representation of a convolutional filter. The filter is $F \times F \times C$ where $F$ represents the filter width and height, and $C$ is equal to the number of channels in the input data. All coloured cubes represent individual weights. Image taken from [19].

If, for example, a $3 \times 3$ kernel is used, the size of the output data changes after every convolution. This change in size will happen for all kernels that are larger than $1 \times 1$. The size change is represented in fig. 2.7, and depends on the size of the kernel and the strides applied in the convolutional layer. The figure shows that information becomes compressed. The pink $2 \times 2$ output contains information about the entire initial input data. Every data point in the output has a receptive field. The receptive field is the size of the data the output values represent. The size of the receptive field can be determined by eq. (2.31). Where $K_j$ denotes the kernel size and $S_i$ denotes the strides. This equation clarifies how both the strides and the size of the filter influence the change of the size of the output data. In the example of fig. 2.7, the individual data points after convolution contains the information of a $5 \times 5$ area in the original data. In this research, only $3 \times 3$ kernels will be used with a stride of 1.

The figure also clarifies that information at the edge of the input data is taken less into account. For example, the corner is only taken into account once, while a data point in the middle of the data is used nine times. This principle will cause a loss of information at the edges of the data. Therefore, data is often surrounded by a layer of zeros, called zero-padding. The process itself is called padding. This way, there is no loss of data at the edges of the data. The amount of required zero padding is determined by eq. (2.32). Parameter $I$ is the size of the input, $S$ the stride, and $F$ the filter size.

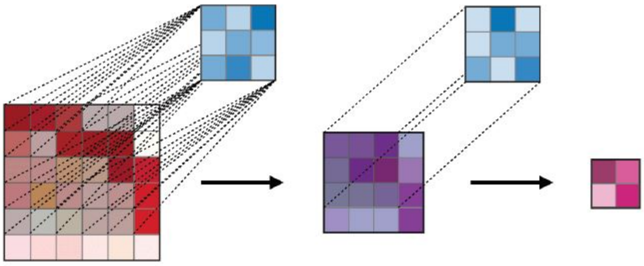

Figure 2.7: Schematic representation of two consecutive convolutional layers. The used filter is $3 \times 3$ and the strides are 1. This will cause a decrease in output size. Image taken from [19].

$$R_k = 1 + \sum_{j=1}^{k} (K_j - 1) \prod_{i=0}^{j-1} S_i \tag{2.31}$$

$$P_0 = \frac{\left(\frac{I}{S} - 1\right) S + F - I}{2} \tag{2.32}$$

**Pooling layers** are commonly used layers in CNNs. One of the pooling layer goals is to lower the number of learnable parameters in the CNN to decrease the required computational power. The most important reason to use pooling layers is that they also add to the generalizability of the network by making it less prone to errors created by translational invariance [20]. Translational invariance is when the data is similar but shifts from its position. There are generally two types of pooling layers used, an average pooling layer or a max pooling layer. Max pooling often outperforms average pooling by highlighting the most distinct data points in the dataset. One of the downsides is the partial loss of spatial information [21]. Max pooling has a filter size, which will be used as an overlay of the input data $I$. The max pooling layer will select the maximum value of the input values within the filter size. This process is displayed in fig. 2.8.

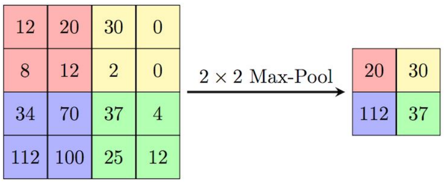

| | | | |
|---|---|---|---|
| 12 | 20 | 30 | 0 |
| 8 | 12 | 2 | 0 |
| 34 | 70 | 37 | 4 |
| 112 | 100 | 25 | 12 |

| | |
|---|---|
| 20 | 30 |
| 112 | 37 |

Figure 2.8: Schematic representation of a max pooling layer. The filter is $2 \times 2$ and removes 75% of the initial data by only selecting the maximum value of the input data $I$ within the filter. Image taken from [20].

**Activation functions** are functions that are applied after a convolution has been performed. This way, nonlinearities can be introduced to the network, or outputs can be suppressed depending on the activation function used. In most models, nonlinear functions are used to introduce nonlinear predicting capabilities to the network. In most recently developed regression models, Rectified Linear Units (ReLU) are often used. The ReLU activation function shows that they are capable of accelerating the convergence of the model. They also help solve the problem of exploding and vanishing gradients, a phenomenon that will prevent the model from effectively learning [22, 23]. The vanishing gradient is a problem that can occur when using multiple hidden layers in the network and using, for example, $tanh$ or $sigmoid$ activation functions which force the output between 0 and 1 or -1 and 1. The activation functions are displayed in fig. 2.9.

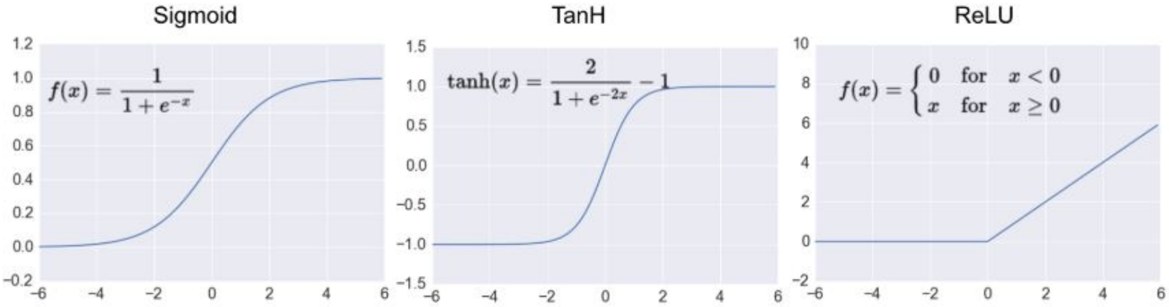

Figure 2.9: $tanh$, $sigmoid$ and $ReLU$ activation function. In this research, the ReLU activation will be used. Image taken from [24].

**Optimizers** are the algorithms that are used to process the error obtained by the loss function. The optimizer processes the obtained error to change the weights in the network by calculating the gradient of the error for every individual weight contribution. How the weights are changed is dependent on the optimizer that is used. Commonly used optimizers are Adam, Adamax, Adagrad, SGD, Adadelta, and RMSProp. The different optimizers will not be discussed in this report since it would not add to the basic understanding of the principles of CNNs. In this research, the Adamax optimizer will be used for both developed models, which will be further elaborated in section 7.3.

**Loss functions** are used to determine the performance of the network in the input data. In regression problems, two types of loss functions are often used. These are: the Mean Squared Error (MSE), see eq. (2.33), and the Mean Absolute Error (MAE), see eq. (2.34). The major difference between the two loss functions is that the error gets squared in the MSE. The squaring of the error means that bad predictions will get even a higher loss, and their influence on the learning process will increase. This loss is then used by the optimizer to change the weights. When using the MSE, bad predictions cause more rigorous changes to the weights of the model.

$$MSE = \frac{\sum_{i=1}^{n} (y_i - \hat{y}_i)^2}{n} \tag{2.33}$$

$$MAE = \frac{\sum_{i=1}^{n} |y_i - \hat{y}_i|}{n} \tag{2.34}$$

This section should provide the reader with necessary information about NNs and CNNs, which should help the reader understand the choices that have been made in chapter 7 and chapter 8. This chapter does not provide all details of the processes but is here to develop a feel of the process.

# 3

# Literature Review

After introducing the motivation and research goal of this report, this chapter will present a literature review on buckling analysis. This review will begin with a short section, section 3.1, on the different methods described within analytical buckling analysis. The next section will explain some state-of-the-art in numerical buckling analysis, see section 3.2. Application of machine learning in structural analysis, and especially buckling analysis, will be discussed in section 3.3. The results of this literature review will be discussed in section 3.4. Experimental research is not taken into account for this literature review since the goal of this research is to develop a model that can correctly predict the ultimate strength.

## 3.1. Analytical Buckling Analysis

The importance of buckling analysis already became clear in chapter 1. The transition from Allowable Stress Design (ASD) to Limit State Design (LSD) made the development of accurate and easy applicable models even more important. LSD has proven itself as a better approach for structural design. By taking multiple modes of failure in consideration, safe, and also economical designs can be developed according to Hughes and Paik [7]. The first buckling models are developed long ago for simple cases like perfect beams assuming elastic material behavior and small deflections. Since then, models became more accurate and realistic by the addition of plasticity, initial deformations, residual stresses, and large deflection theory. The addition of more complex behaviors also increases the model complexity. Also, the use of different materials like aluminum, high strength steels, composites or even a combination of them cause the necessity for new model development.

A significant amount of analytical models have been developed over the last couple of decades. Most models are developed based on standard ultimate strength models that are widely adopted. These are the models that are described in many structural engineering books. Most of those models consider five different modes of buckling failure, like those described in Paik [14] and Bakker et al. [25]. These buckling modes can be seen in fig. 3.1. Those models are extended to be also accurate for structures loaded with a combination of multiple loads like in Paik and Kim [26],Paik et al. [27]. Most of the newly developed models are empirical models related to a specific material or load-case or a combination of both. For example, Paik [28] developed an empirical set of equations to predict the ultimate strength of aluminum stiffened panel loaded under axial compression. This research was extended to also contain accurate results for aluminum stiffened panels subjected to a combination of axial compression and lateral pressure by Khedmati et al. [29]. Previously developed empirical closed-form formula coefficients are refit to obtain new ultimate strength calculation for stiffened steel plates with crack damage subjected to axial compression by Zareei and Iranmanesh [30].

### Factors That Influence The Ultimate Strength

The type of stiffeners used, corrosion, initial deflection, and residual stress are considered important factors in predicting the ultimate strength of stiffened panels used in the marine environment. Much research is devoted to the type of stiffener use as stiffening of plates. Danielson and Wilmer [32] derived analytical expressions to predict the ultimate strength of bulb profiles and obtained results that are similar to the results found by applying Finite Element Analysis (FEA) on the same structures. Also, the effect of corrosion on the ultimate strength of stiffened and un-stiffened panels is researched. Mohammad et al. [33] investigated the effect of corrosion on both stiffened and un-stiffened panels under longitudinal uni-axial compression by making use of extensive FEA in Ansys. They assessed the effect of corrosion for a different number of exposure years. Kim et al. [34] derived a fourth-order polynomial

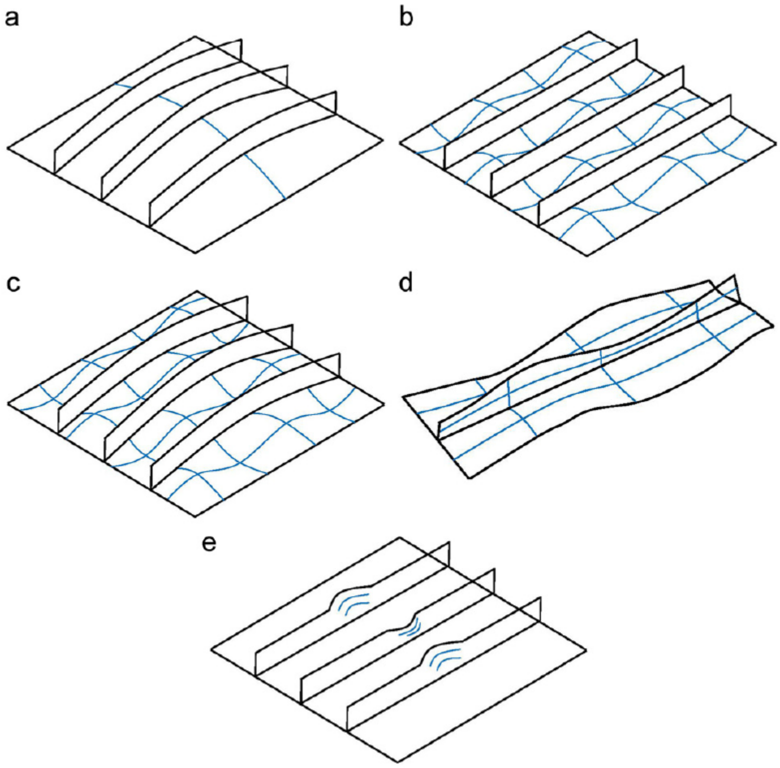

Figure 3.1: Widely accepted failure modes of stiffened plates. (a) Overall buckling of the plate and stiffeners. (b) Buckling of the plating between stiffeners wihtout collapse of the stiffeners. (c) Beam-column type buckling of the stiffener with attached plating. (d) Buckling in the stiffener web. (e) Tripping of the stiffener. Image taken from [31].

based on ALPS/ULSAP obtained results to predict the ultimate strength behavior of stiffened panels that are generally used in the construction of double-hulled oil tankers. ALPS/ULSAP is a module for the Ultimate Limit State (ULS) evaluation of steel and aluminum stiffened panels. Stiffened panels are, in reality, never considered perfect. Welding and fabrication cause the structure to develop an initial deflection, which can lower the structure's ultimate strength. In most research papers, initial deflection is assumed to be a Fourier series buckling shape. In contrast, real initial deflections are often more complex and hard to describe, as described by Yao and Fujikubo [35]. The post-buckling response of stiffened panels under axial compression has been investigated by applying uncertain initial plate deflection by Qiu et al. [36]. Another important factor related to the ultimate strength of structures is the residual stress introduced by, for example, hot-rolling and welding of steels. Chen and Soares [37] developed a simple model to predict the residual stress distribution in stiffened plates subjected to axial compressive loads. The research explicitly looks at residual stress caused by fillet welding during production. They based the model on results obtained with FEA. They found important relations between the residual stress and initial imperfection. Severe initial deflections with residual stress caused even a drop of 18% of the ultimate strength compared to the case where no initial deflection was presented. Residual stress on average decreased the ultimate strength with around 5-7%.

**Large Deflection Theory**

Often small deflections are assumed, implying small strains and small rotations, significantly reducing the complexity of models. In shipbuilding, stiffened panels are subjected to loads that can cause deformations such that the strains are often not considered within the small deflection theory-range. Therefore some analytical models incorporate large deflection theory, increasing the model complexity often to a semi-analytical model. Some of those models that are developed are designed for a broad spectrum of different loading conditions. A semi-analytical model to predict buckling and post-buckling behavior has also been developed by Byklum and Amdahl [38] to handle multiple combinations of loads. In this research, a set of equations is designed to analyze the large deflection buckling behavior for any combination of bi-axial compression, shear, and lateral pressure. The model they developed shows good correspondence with results obtained through FEA. Post-buckling models are also used to derive a set of analytical equations to model large-deflection behavior for stiffened plates under transversal axial compression by Bakker et al. [25]. Due to the decoupling of flexural en membrane response, they developed a simple and more readily applicable set of equations.

**Boundary Conditions**
In shipbuilding, stiffened panels are continuous structures. A model of a stiffened panel is in reality surround by other equal stiffened panels or similar structural elements. This continuous structure implies partially constrained rotation boundary conditions at the location of longitudinal and transversal stiffeners. Partially constrained boundary conditions are often difficult to model in FEM. For analytical models, boundary conditions are often assumed simply supported according to Okumoto et al. [39]. Boundary conditions in structural analysis can have a significant influence on the results obtained. Therefore, a significant amount of research is applied to the boundary conditions of stiffened panels. Paik et al. [40] obtained an analytical model for the prediction of large deflection behavior of stiffened steel panels with partially rotational restrained boundary conditions. The model is obtained by modification of simply-supported plate equations.

This section clarifies that although the first models for predicting the ultimate strength of stiffened panels are dated before 2000, a significant amount of research is still being done on modifications of already existing equations or the development of new sets of equations. Most state-of-the-art research is related to a specific load-case, material, or a combination of both. Substantial research is also done related to residual stress, initial deflection, and accurate boundary conditions for stiffened plates. Topics as corrosion and crack damage are also researched within the field of ultimate strength prediction. So, most current research is related to obtain easy and quickly accessible equations for specific cases. This section makes evident that there is still the ongoing desire to develop models that are quick and easily applicable to predicting the ultimate strength of thin structures and produce an accurate prediction of the ultimate strength.

## 3.2. Numerical Buckling Analysis

In buckling analysis, numerical models like Finite Element Methods (FEM) are widely seen as an essential design tool. Finite Element Analysis (FEA) yields accurate results under the right assumptions and with correct boundary conditions. However, for large complex models, it requires a significant amount of computational power, according to Byklum and Amdahl [38]. Experimental research on the buckling of stiffened panels is expensive and time-consuming. Therefore, FEA is often used to validate results or as a data generation tool to perform new research. In many of the previously discussed studies, FEA is used: Paik [28], Khedmati et al. [29], Zareei and Iranmanesh [30], Mohammad et al. [33], Chen and Soares [37], Paik et al. [40]. Finite Element (FE) software is widely available in different commercial packages and is often used to perform research which is challenging to execute with experiments.

**Boundary Conditions**
As mentioned in section 3.1, the boundary conditions for stiffened panels in shipbuilding are often assumed simply supported while, in reality, it behaves partially rotational constrained. Accurate boundary condition selection in FEA has shown its importance in many research papers. A substantial amount of research has been performed on the influence of used boundary conditions. When FEA is used to perform analysis on stiffened plates, different structural layouts are used in recent research. Sometimes 1-bay or 1/2+1+1/2-bay plate stiffener combinations are used, or most often they are 1-bay|1-span, 1/2+1+1/2-bay|1-span or 1/2+1+1/2-bay|1/2+1+1/2-span models as described in the research of Hughes and Paik [7]. FE models larger than 1-bay|1-span make it possible to model the large longitudinal and transversal stiffeners. Often they are not geometrically created but are mimicked making use of boundary conditions. The adoption of those more advanced models and boundary conditions is recently widely researched. Xu et al. [41] investigated the effect of the used boundary conditions for two different layouts. Both periodic and symmetry boundary conditions were investigated. They concluded that the best choice of boundary condition is plate aspect-ratio dependent for uni-axial loaded stiffened panels. The aspect ratio determines if an odd or even number of halve waves will develop in the panel. Similar research has been performed on stiffened panels subjected to several combined loads by Xu

et al. [42]. In recent research, this study is extended to different types of stiffeners commonly used in shipbuilding by Pan et al. [43].

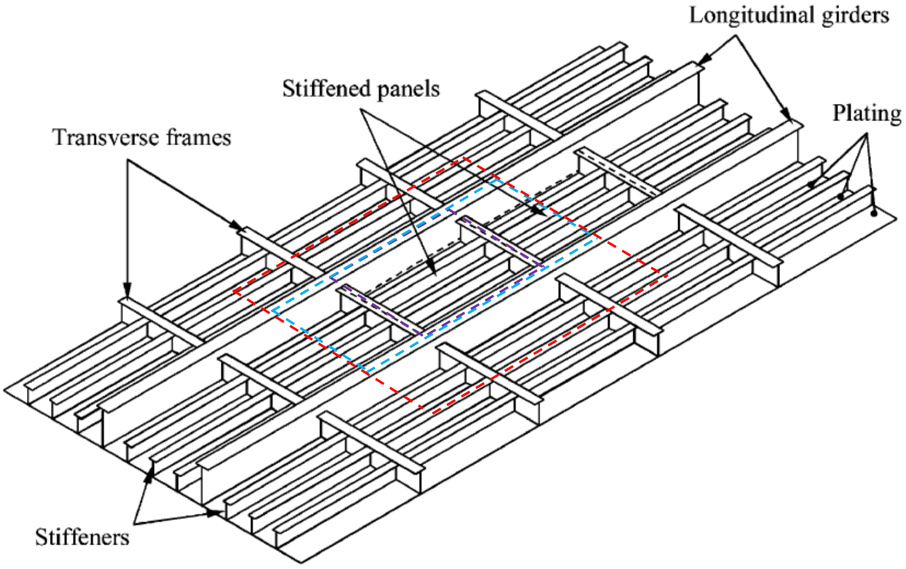

Figure 3.2: Continues stiffened panel. The purple line defines a 1-bay|1-span model. The blue line defines a 1/2+1+1/2-bay|1-span model. The red line defines a 1/2+1+1/2-bay|1/2+1+1/2-span model. Image taken from [26].

### Factors That Influence The Ultimate Strength

Besides the fact that the application of FEA is often more efficient than experimental research, some processes are difficult to test in real experiments. For example, the effect of structural cracks on the ultimate strength is difficult to test with real experiments. The effect of longitudinal through-thickness cracks on the ultimate strength of steel flat and stiffened panels has been investigated by Du et al. [44]. The effect of welding residual stress is also possible to model with FEM. Khedmati et al. [45] used FEA to investigate the effect of different residual stress patterns on the ultimate strength of aluminum stiffened panels, a research that is difficult to do experimentally. They also tested the effect of different stiffener arrangements. The stiffened panels in this research are subjected to a combination of axial compression and lateral pressure. In new-built ships, the use of high-strength steel becomes more prevalent. High strength steels often behave differently then mild steels. The ultimate strength of mild and high-strength steel stiffened panels is tested by the use of FEA in research by Li et al. [46]. They incorporated both initial deflection and residual stress within the models. Multiple stiffener arrangements have been tested, namely flat bar, T-stiffeners and bulb stiffeners are tested within the research.

Most of the previously mentioned research was applied to flat stiffened panels. In shipbuilding, also curved stiffened panels are used around the bow, stern, and bilge. However, less research is available on curved stiffened panels. The effect of curvature in one direction has been researched. It is found that parabolic curvature can significantly increase the ultimate buckling strength of stiffened panels according to the research of Khedmati and Edalat [47]. Similar results were obtained in a recent extensive investigation of the buckling strength and collapse behavior of curved stiffened panels loaded under axial compression executed by Park et al. [48].

### New Developed Numerical Models

Besides the use of widely available FE software, some researchers try to develop better FE models. Instead of using the classical approach to obtain all the stiffness matrices in FEA, Carrera Unified Formulations, CUF, are developed. Recently, CUF is used to predict the large deflection behavior of square plates loaded with transverse uni-axial compression. The research of Wu et al. [49] found an increase in accuracy and speed compared to conventional FE calculations. Besides the use of quasi-static FE analysis for the ultimate strength analysis, Element Free Galerkin methods (EFG) can also be used for buckling analysis of thin structures. Research by Huang et al. [50] found that overall EFG accuracy is similar to that of quasi-static FE analysis. Besides that, they also mentioned that EFG required more computation power on average. An improved version of EFG has been developed by Sadamoto et al. [51]. The improved version is tested on perforated and stiffened panels. The described method is more efficient for performing buckling analysis on stiffened panels. Constrained Finite Element Method (cFEM) is a new development of FEA by Jin et al. [52] where it is possible to decompose the buckling deformation into three groups. The three groups are global displacements, distortional deformations, and local deformations, allowing for individual analysis of the different deflection mode components. The research was applied to thin-walled structures. Thriving results are recently achieved with the use of cFEM on stiffened panels by [53].

A different numerical method for assessing the ultimate strength of stiffened panels is PULS, Panel Ultimate Limit State. PULS is based on orthotropic plate theory and suitable for different loads and types of stiffeners. Steen et al. [54] proves that PULS outperforms most empirical sets of equations and the results obtained with PULS are close to that of conventional FE software.

An alternative for FEA is Finite Strip Methods (FSM). Instead of element subdivision of the structure, the structure is divided into small strips, reducing the complexity of the model, but also making it less versatile in application than FEA, according to Khan [55]. Although it is less versatile, new models based on FSM are still being developed. A semi-analytical FSM is developed to perform buckling analysis by Hancock and Pham [56]. The results of the newly developed version of FSM are compared with results obtained from FEM and spline-FSM. The developed model showed good accuracy compared with FEA and spline-FSM. The model shows to be more efficient than both FEA and splines-FSM.

This section clarifies that FEA is widely adopted as a method for performing buckling analysis for a wide variety of conditions. FEA is often used as a validation tool for analytical models. This section also shows that FEA can be a good alternative for experimental research in situations that are challenging to recreate in experiments. Examples of those researches are related to crack damage and different residual stress contributions. Despite many applications, researchers still try to develop more accurate, faster, and easier applicable models.

## 3.3. Machine Learning Applied in Structural Anaylsis

Machine learning (ML) is currently applied in a wide variety of tasks in many different disciplines. ML is starting to find its way in structural engineering. According to Salehi and Burgueño [3], An increase in studies is observed where ML is used in structural engineering. A large part of the research is related to Neural Networks. The first application of machine learning to predict the buckling strength of stiffened panels already dates back to the late 1990s, which is the research performed by Wei and Zhang [57]. The research obtained considerably good accuracy in predicting compressive strength by making use of a counter-propagating neural network. The data used in this research was obtained from previous experiments.

### Buckling and Ultimate Strength Prediction of Columns and Beams

ML is applied to a wide variety of topics within structural engineering. ML is often utilized in research related to processes that are difficult to correctly model and predict. This application is the case with non-linear materials, such as concrete, which is an in-homogenous material. Babanajad et al. [58] used Gene Expression Programming (GEP) to predict the ultimate tri-axial strength of concrete. A large dataset is obtained based on literature. With the application of GEP, accurate ultimate strength predictions are obtained, which are often more accurate the predictions made with widely available models. As mentioned in the introduction of this section, NNs are often applied within structural engineering. Some research reflects on the performance of neural networks compared to other methods, like fuzzy logic and regression. The different models were tested on reinforced concrete columns by Tekeli et al. [59]. A similar performance was obtained between the different models.

NNs are widely applied for predicting deflection and or ultimate buckling strength of beams and columns. The amount of experiments in structural engineering is often limited. In a significant number of studies, data required for machine learning is generated using FEM. This principle is applied to the distortional buckling of steel I-beams by Tohidi and Sharifi [60]. A NN was developed to predict the buckling strength of bridge girders with restrained distortional buckling. The dataset consists of a small amount of FE models. The NN was used to develop a simple equation that can be efficiently used to predict the steel I-beams' buckling ultimate strength. Similar research was recently applied to the more complex cellular steel I-beams. A small amount of data was used for training and testing by Sharifi et al. [61]. An earlier study performed by Abambres et al. [62] also investigates the ultimate buckling strength of Cellular I-profiles with the use of a NNs. They used 3645 models for training and testing. The NN makes an average error of 0.4%. Due to the easy use of trained NNs, they can also be successfully used to perform a parametric study for column buckling, according to the study of Sheidaii and Bahraminejad [63].

**Plates and Stiffened Panels**

Besides the use of machine learning for column buckling, various studies have also been done related to plates, thin shells, and stiffened panels. The application of NNs on the ultimate strength prediction of steel stiffened plates has been tested on a small set of data by Pu and Mesbahi [64]. In total, 119 examples were used for training, and 24 examples are used for testing the models. With a small amount of training data, better performance was already obtained compared to empirical formulations. The application of NNs is also tested for plates made of non-linear materials. Aluminum and stainless steel alloys often have a complex stress-strain curve, which is non-linear. The ultimate strength of plates made of aluminum and stainless steel subjected to axial compression has been predicted by using an NN and a Gene-Expression Programming algorithm (GEP) in the research of Cevik and Guzelbey [65]. The GEP made an average error, which was three times larger than the NN's average error. Besides metals, NNs are also applied to composites. The amount of training data used in the research of Subramani and Sharmila [66] was also limited. Results were in agreement with results obtained from FEA. FEA was also used to generate a dataset of steel plates with circular holes in the research done by Sonmez and Komur [67]. A total of 400 FE models have been used to train a NN to obtain an explicit formula to predict the ultimate strength of steel plates with circular cut-outs. An error of less than 2% was obtained in this research. Response Surface Method, RSM, is sometimes used in structural engineering to obtain an approximation of the relation between design parameters and structural response. Conventional RSM can be a timing consuming process. An NN-RSM combination is developed to obtain a more accurate and faster ultimate strength assessment for plates by Pu et al. [68]. The ultimate strength of steel-arches has also been tested on a small set of data by Hasanzadehshooiili et al. [69].

The application of machine learning to the ultimate strength of stiffened panels is limited. A combination of NN-RSM has also been developed for stiffened panels by Mesbahi and Pu [70]. The NN was developed to obtain an empirical formulation for ultimate strength prediction. This research mentioned that NN-RSM showed consistent performance on extrapolation. The ultimate strength of flat-bar aluminum stiffened panels has also been predicted using ML in research done by Zareei et al. [71]. Effects caused by welding were incorporated into this model. The research showed more accurate results compared to standard empirical formulations. A NN trained on a small set of FE models has also been used to predict the ultimate strength of laminated composite stiffened panels loaded with in-plane shear. The model showed high accuracy and efficiency, according to Mallela and Upadhyay [72]. Kumar et al. [73] developed a model to determine the ultimate strength of hat stiffened composite panels subjected to axial-compressive loading. The obtained error of most models is below 2%

Most of the discussed research on the ultimate strength of plates and stiffened panels only tested the performance of the machine learning models inside the range of training. A limited amount of research mentioned that they looked into the generalizability and scalability of the model.

**Shell Structures**

Buckling is a phenomenon that is interesting not only for plates and stiffened panels. Buckling assessment is essential for all structures that are considered thin that will meet compressive forces during usage. Recently, a NN is used to predict the ultimate buckling load of cylindrical shells. For this research, 390 models were obtained from different experimental studies. An average error of less than 10% was obtained on the experimental test data for the model within its training range. Tahir and Mandal [74] concluded that models outside the training scope should be handled with care, and more data would be required to obtain decent results.

**Stress Prediction**

Most of the described studies make use of simple NNs. The inputs of the models developed are often geometrical parameters or material parameters. In some models, they use ratios between different parameters. The output of most models is often either a deflection, stress, or force. Most ML models are built with a single or a few hidden layers and use *sigmoid* or *tanh* non-linear activation functions, which show less application in the last few years. Also, the use of newer NN architectures like Convolutional Neural Networks (CNN) is limited. The use of newer optimization algorithms like Adam is also limited. Some research does make use of newer machine learning strategies. Especially within the sector of biomedical engineering, researchers start to use newer ML algorithms and architectures. FEA is also widely adopted in the biomedical world, especially for urgent patient-related models, quick and accurate FE models are needed. Within the biomedical application of FEA, buckling does not play a role, but stress prediction over a structure does play an important role. Stress prediction is closely related to ultimate strength prediction, and thus it will be incorporated within this research.

Computational Fluid Dynamics (CFD) can be used to predict stresses caused by fluid flow, for example, the blood flow through the aorta. CFD calculations rely on a similar process to that of FEA but are used for fluid flow problems. In recent research performed by Liang et al. [75], 729 patient aorta FE meshes have been used to predict the stress distribution over the entire aorta. Instead of using a few input parameters like in all previously discussed research, they use the mesh of the geometry as input. First, the geometry is mapped to a 2-D surface. By using Principle Component Analysis (PCA), this flattened geometry is compressed to an array containing a few digits. This array represents the geometry. This process is also called shape encoding. The array compressed from the input geometry forms the input for a fully connected Deep Neural Network (DNN), that maps the compressed geometry array to a compressed stress array. This compressed stress array is the compressed form of the stress distribution over the geometry. This compressed array is then decoded to the initial geometry with the stresses determined on every node of the geometry, called stress decomposition. A low error of 0.492% was obtained compared to FEA data. The research mentions that although a small error is obtained, a clinical application needs a more substantial amount of training data to give accurate, reliable results.

Similar research has been done to predict hemodynamics; the velocity and pressure fields of the blood flow. The same input data has been used in the later research. In the research by Liang et al. [76], three different models were developed to predict the pressure field, velocity magnitude, and the velocity vector field. The models are slightly different from those described in the previous paper, but the encoding-decoding architecture principles are used again. The velocity field and the pressure field were predicted with an average error of less than 2% compared to FEA results. For clinical acceptance, a rejection option is required when input differs too much from the initially trained dataset.

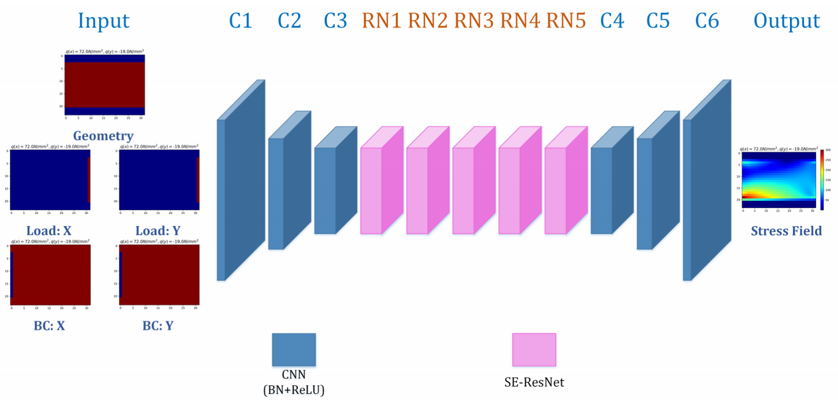

Figure 3.3: Overview of the StressNet architecture showing in blue the convolutional layers, and in pink the squeeze and excitation modules. Image taken from [77].

A more structural related research tried to predict stress distributions in cantilevered structures. This research by Nie et al. [77] also used the encoder-decoder structure for the two models that they developed, called SCSNet and StressNet. For the encoder, convolutional layers have been used, keeping spatial information within the model. Convolutional layers are also used for the decoder. SCSNet makes use of fully connected layers between the encoder and the decoder. Stressnet replaces the fully connected layers with squeeze and excitation modules in combination with ResNet identity modules, as can be seen in fig. 3.3. The used data-set contains 120.960 small FE models. StressNet outperformed SCSNet significantly. SCSNet made an average error five times larger than StressNet. The error they obtained with predicting the maximum stress is even lower than the average stress prediction error. This research also tested the effect of a smaller amount of training files, by training the model also for 20.000 models. Both trained models showed similar trends, and further lowering the number of training examples is not tested. Another research also used a mesh as input for their developed NN.

**Structural Mesh as Input for Neural Networks**
Inverse problem solving is when the output of the scenario is known, but we want to learn what the initial condition is. Inverse problem solving is something that is often related to damage en failure analysis. To learn what caused the failure, we want to know the initial conditions that caused the failure. The research by Chen et al. [78] used impact loaded structures as input for the model to predict the loading at the moment of impact and the speed of impact and the impact duration. This research makes clear that NNs can learn to predict critical structural parameters. In this research, they used PCA to map the geometry, consisting of 6400 nodes, to a smaller array, forming the input in the fully connected NN. The research of Ren et al. [79] also tried to predict the location, load, and duration of impact loads on beams. They directly fed the mesh with plastic deformations as input to the DNN. ML is not only used as a post damage tool. It can also be used to predict damage in structures, which is difficult when, in reality, damage can be internal. In the research performed by Liu and Zhang [80], they developed a Convolutional Neural Network (CNN) to predict brace buckling damage in frames. CNNs require an image-like input. In the study by Liu and Zhang [80], seismic-loading graphs are mapped into a Fourier spectrum image and used as input for the CNN. The CNN is developed to classify if an element will be damaged or not, and executes this task with high accuracy. A CNN is also developed in the research of Liu and Zhang [81] to classify damage to steel structures. A VGG-16 architecture is adopted for the developed network, and it is tested on two different FE structures. The first model is trained on 3200 and 8600 data points. It was observed that more training data would improve the accuracy of the model. They recommend using a dataset of several thousand images to obtain correct predictions. The second model is only trained with the full dataset. In both models, an average error of less than 5% was obtained.

As can be seen from the literature described above, machine learning has found its way in structural engineering. Although, notably, one of the issues within this field of research is the amount of available data. Most research is based on a small dataset of models. Only the most recent studies made use of datasets over a thousand data points. Also, the application of the more modern machine learning methods and architectures is limited. Most studies that are related to the ultimate strength prediction of stiffened plates tend to use simple NNs. Only a few studies mention the ML models' performance outside the scope of training, so-called scalability, and generalizability. To the author's knowledge, non of them provided the reader with actual detailed information over the performance outside the range of training. Most of the discussed studies trained the model with all the data they had available. Just one of the discussed studies tried to train the ML model with fewer data to see how the amount of data influenced the performance.

## 3.4. Conclusion

This chapter provided the reader with an overview of buckling analysis and research related to the topic of this report. Both section 3.1 and section 3.2 make it clear that the development of more accurate and efficient applicable models is desired. A significant proportion of the research is done to analytical buckling models related to specific geometry, load, or material cases. Not many researchers develop methods suitable for a wide variety of load and material cases. The application of FEM is proven versatile for performing buckling and ultimate strength analysis in section 3.2. FEA is often adopted as a validation tool for analytical models. FEA can successfully be used to predict the ultimate strength of cracked or corroded structures accurately. Despite the broad application of FEA, some researchers try to develop better and less computational expensive tools. Those models are often based on already available methods like FEM, FSM, and EFG.

From section 3.3, it becomes clear that buckling analysis by making use of ML is not new. Most researchers obtain good accuracy by using ML with only a small amount of training data. This accuracy is obtained on results closely related to the data the ML was trained on. Until recently, most used ML models are simple NNs. The use of newer and more advanced models is still limited. Some of the discussed studies state that inaccurate predictions are obtained outside the range of training. However, limited information is provided about this performance. Only one paper mentioned the influence of the number of training samples on the performance of the model. They tested with two different sizes of training data and found an increase in accuracy with more training data available.

From this literature review, it becomes clear that machine learning can be a useful alternative for predicting the ultimate strength and stress distribution compared to FEA. Still, FEA often remains necessary to obtain enough data to train the ML model. To the author's knowledge, too little information is available on the required amount of data to train accurate ML models for structural engineering problems. The lack of information means that no clear conclusion can be drawn relating the amount of training data to ML's performance within structural engineering. It is essential to know this because, for most structural engineering problems, that amount of available data is limited. The absence of required information is considered a gap in the literature. Also, too little information is available on the scalability and generalizability of those designed models. No conclusion can be drawn on how well-trained ML models can predict accurate results outside the scope of training. The inadequacy of this information is considered a second gap in the literature. The research goal and the related sub-goals will try to fill this gap in the literature.

# II

# Data Generation

# 4

# Stiffened Panel Model

After introducing the fundamentals of buckling and machine learning in chapter 2 and the literature review in chapter 3, this chapter will give a short basic description of stiffened panels and their loading conditions. It will be explained what a stiffened panel is considered within this research. If the reader is familiar with what a stiffened panel is and the basic loading conditions of the ship structure, it is not required to read this chapter. The explanation will start with a short description of the ship's hull structure and the stiffening related to this structure. Also, the material used in this research will be elaborated. This will be explained in section 4.1. The next section will address the loads a ship hull will be subjected to during its operations and the effect of those loads on the ship's structure. This can be read in section 4.2.

## 4.1. Geometry and Materials

The primary structural element in ships are large stiffeners and plates. The primary stiffening in ships consists of large longitudinal stiffeners called girders and large transverse stiffeners called frames. These are highlighted in the schematic, fig. 4.1, by orange and green lines, respectively. The primary stiffening in ships forms the 'skeleton' of the ship. The primary stiffeners are welded to the 'skin' of the ship, which is the outer hull.

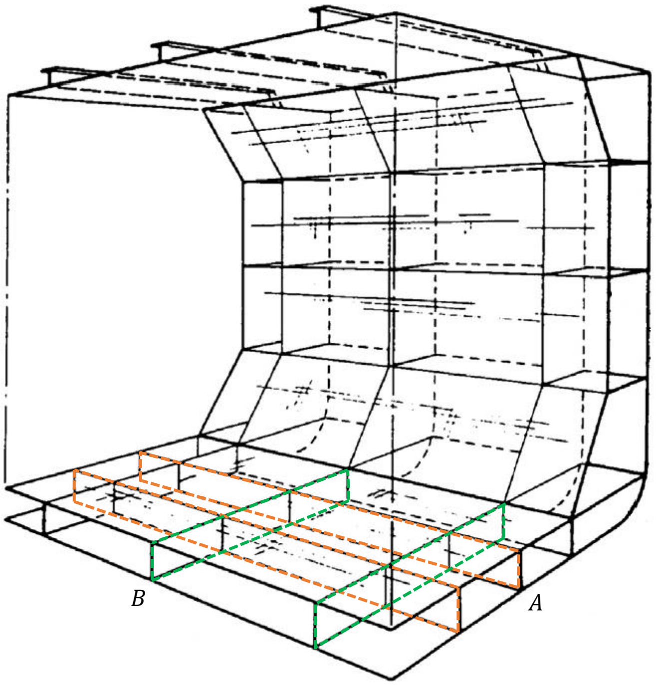

Figure 4.1: Schematic of a ship's hull construction without secondary stiffening drawn. (A) Longitudinal stiffening, also called girders, are marked with orange. (B) The transverse stiffening, also called frames, are marked with green. Image taken from [6].

The spacing of the girders and frames can be several meters. The stiffness of the plates is generally not sufficient to carry the loads, and therefore secondary stiffening is introduced, which is not drawn in the schematic. Secondary stiffening is often consists of only small longitudinal stiffeners evenly spaced between the girders. If the span between frames becomes large, stiffened panels will sometimes be made cross-stiffened by placing small transverse stiffeners between the frames. In this research, a stiffened panel is defined as a plate in which boundaries are the large girders and frames, with only longitudinal secondary stiffening. Represented by the purple 1-bay|1-span model in fig. 3.2.

The primary stiffeners at the edges of the stiffened panel, are significantly larger compared to the secondary stiffeners. They are designed to have a large resistance to bending and deforming, but they will bend during heavy loadcases. It is difficult to capture this behavior with simple boundary conditions when the structure is continuous. The boundaries can best be defined by a simply supported boundary condition with some resistance to rotations. These boundary conditions are difficult to model, and the resistance behavior is complex. Therefore it is often assumed that the boundary conditions can be modeled as simply supported, allowing rotations and in-plane movement of the plate edges. Besides, it is assumed that the edges remain straight.

In shipbuilding, a wide variety of secondary stiffening is used. The most common stiffeners used are T-stiffeners (tee stiffeners), bulb profiles, angle profiles, and flat bar stiffeners. A graphical representation is given in fig. 4.2. T- and angle stiffeners can either be welded or hot-rolled sections. Bulb profiles are often rolled. Flat bars are sensitive to tripping, a form of stiffener failure, and are therefore less used nowadays. T- or bulb stiffeners are frequently used; the best choice is case dependent. In this research, it will be assumed that the stiffening of the plate is made up of T-stiffeners. The main reason for this is their high flexural rigidity, their resistance to bending, and the ease of modeling and not introducing eccentricity effects from the geometry, which would be present when bulb profiles are used.

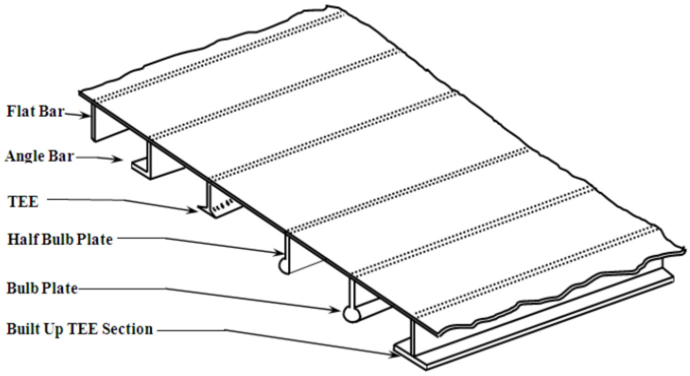

Figure 4.2: A graphical representation of the most commonly used stiffeners in shipbuilding. In this research T-stiffeners are used. Image taken from [82].

The primary building material for ships has long been standard structural steel. There is a wide variety of steels available with different advanced properties. In shipbuilding, the use of high strength steels becomes more prevalent. Aluminum is also often used in shipbuilding, but the primary usage is in the housing of ships. The application of aluminum in hulls is limited and often related to small vessels. Therefore steel will be used for the stiffened panels throughout the research. The streel primary used in ships is still mild structural steel, S235. The material properties are given in table 4.1 and will be used throughout the research.

Table 4.1: Mild structural steel S235 material properties.

| Property | Value | Units |
|---|---|---|
| Young's Modulus | 206 | $GPa$ |
| Poisson's Ratio | 0.3 | – |
| Yield strength | 235 | $MPa$ |

## 4.2. Loading Conditions

In the design of ships, two types of load are often considered: operational loads and accidental loads. Operational loads consist of still-water loads and environmental loads. Still-water loads consist of the ship's loading but also the buoyancy forces. Environmental loads are the loads caused by the environment, like waves, wind, and currents. Accidental loads are the loads that are caused by, for example, collision. In this research, the still water bending moment, motion in waves, and the hydrostatic pressure will be incorporated. The still water bending moment and the wave loads are related to axial compression of the structure, which will be elaborated in section 4.2.1. Water will also cause lateral pressure to the structure, also called hydrostatic pressure, which will be discussed in section 4.2.2.

### 4.2.1. Axial Compression

Axial compression is compression in the longitudinal or transverse direction. For ships, longitudinal axial compression is the most critical load related to buckling. Transverse compressive forces will develop due to bending and rotation but are considerably smaller than the longitudinal compressive forces. Therefore, only the longitudinal compressive force will be taken into account for this research. Longitudinal compression is developed by the behavior of the construction in waves and the still water bending moment. Both loads will cause bending of the ship, also called hogging and sagging. In fig. 4.3, the effect of hogging and sagging is schematically displayed.

During hogging, there is excessive buoyancy in the middle of the ship, causing it to bend downwards, compressing the bottom of the ship and extending the deck. During sagging, there is more buoyancy at the bow and the stern of the ship bending the bow and stern upwards. This way, tension will be generated in the bottom structure, and compressive force will develop in the deck. Hogging and sagging is something that mainly develops with long wavelengths and large waves, and they can generate significant compressive forces in the construction. In reality, the compressive force might not be perfectly evenly distributed over the side of a stiffened plate. However, it is assumed that the longitudinal compressive force of the side of the plate is evenly distributed for simplicity. In this research, it is assumed that the uniaxial compressive force in the longitudinal direction of the stiffened panel is uniformly distributed over the stiffened panel's entire face.

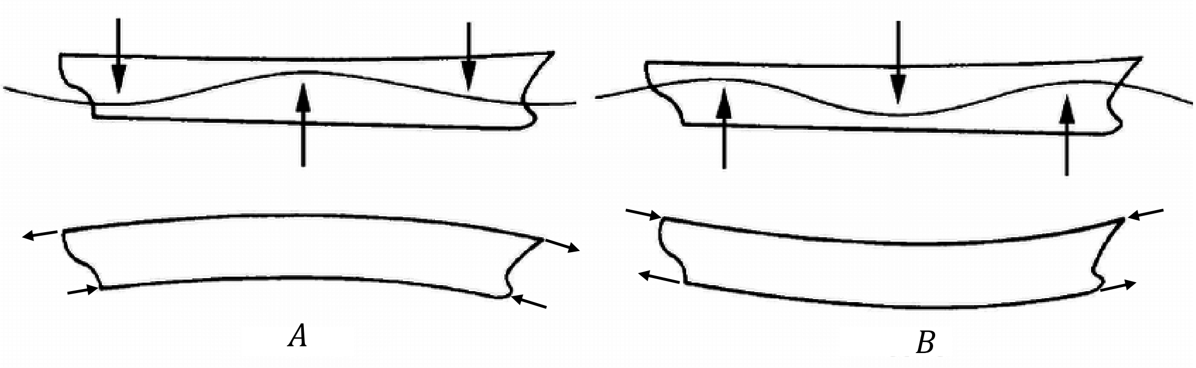

Figure 4.3: Compressive force is generated in the ship due to hogging and sagging motion in waves. (a) Shows the hogging motion of the ship. Compression is present in the bottom of the ship. (b) Shows the sagging motion of the ship. Compression is present in the deck of the ship. Image taken from [83].

### 4.2.2. Hydrostatic Pressure

Hydrostatic pressure is the pressure on the structure developed by the weight of the water, which can simply be calculated from eq. (4.1). Parameter $\rho_w$ is the density of the water, often taken as 1025 kg/m$^3$ for seawater. Parameter $h$ is the water depth in meters, $g$ the gravity constant, which is equal to 9.81 m/s$^2$. The hydrostatic pressure of a ship is in still water constant but might vary due to waves.

$$p = \rho_w g h \tag{4.1}$$

Within this research, it is assumed that the stiffened panels are located at the bottom of a ship similar to the *Maersk E Class*, which is in a hogging state, with a draft of 16 meters. A factor of 1.1 is added to the draft to add some influence of waves. A wave height of 1.6 meter falls within the moderate sea state. This draft is chosen so the hydrostatic pressure would have significant interaction with the compressive forces.

Other forces occur during the bending and rotation of the ship as well. These forces, such as shear force, will be neglected in this research. The stiffened plates in this research are loaded with both longitudinal uni-axial compressive force and lateral pressure. In cases where the order of loading can play a role, like in non-linear buckling analysis in FEA, it is assumed that only lateral pressure is present in the first load step. After loading with lateral pressure, it will be loaded with compressive forces.

# 5

# Analytical Large Deflection Model

This research aims to predict the utlimate strength and the stress distribution at the moment of failure over a stiffened panel by using machine learning (ML). ML needs a significant amount of data for it to effectively learn information between the provided data. Thus, it is necessary to develop an extensive dataset that will be used to train the ML model. This research uses stiffened panels in the hull of ships as input data for the ML model. Therefore, it is essential to have data that correctly represents the structures that will generally be seen in shipbuilding. It is not easy to determine a comprehensive set of geometrical parameters that correctly represents stiffened panels used in shipbuilding by only making use of literature. For this reason, it is chosen to use an analytical buckling model described by Hughes and Paik [7] that incorporates the effects of initial deflection, large deflections, and welding residual stress. This model is also suitable for the desired combination of uniaxial compression and lateral pressure.

The first section in this chapter, section 5.1, will discuss the basic principles of the analytical model. After that, a short discussion will be given on the used geometry and the parameters involved in section 5.2. The third section, section 5.3, is dedicated to the main failure modes, which are considered in the buckling of stiffened panels. In section 5.4, the assumed initial deflection will be discussed, and the principles of incorporating residual stress within the model will be explained. In section 5.5, the analytical model that was developed will be verified with results obtained from the literature. In section 5.6, it will be explained how this analytical model is used to perform an optimization to obtain a representative set in geometrical parameters of stiffened plates.

## 5.1. Model Description

The analytical model incorporates initial deflection of the plates and stiffeners, large deflection theory, and residual stress in the plating due to welding. By incorporating those non-linearities, this model will give a good estimate of the buckling ultimate strength. The parameter optimization will be used to generate a comprehensive set of geometrical parameters of stiffened panels.

The model described by Hughes and Paik [7] is based on large deflection theory developed by Von Kármán [84]. This plate theory assumes the following equilibrium equation when incorporating initial deflection $w_0$, eq. (5.1). The corresponding compatibility equation is given by eq. (5.2).

$$D_x \frac{\partial^4 w}{\partial x^4} + 2H \frac{\partial^4 w}{\partial x^2 \partial y^2} + D_y \frac{\partial^4 w}{\partial y^4} - t\left[\frac{\partial^2 \phi}{\partial y^2}\frac{\partial^2 (w+w_o)}{\partial x^2} - 2\frac{\partial^2 \phi}{\partial x \partial y}\frac{\partial^2 (w+w_o)}{\partial x \partial y} + \frac{\partial^2 \phi}{\partial x^2}\frac{\partial^2 (w+w_o)}{\partial y^2} + \frac{p}{t}\right] = 0 \quad (5.1)$$

$$\frac{1}{E_y}\frac{\partial^4 \phi}{\partial x^4} + \left(\frac{1}{G_{xy}} - 2\frac{v_x}{E_x}\right)\frac{\partial^4 \phi}{\partial x^2 \partial y^2} + \frac{1}{E_x}\frac{\partial^4 \phi}{\partial y^4} - \left[\left(\frac{\partial^2 w}{\partial x \partial y}\right)^2 - \frac{\partial^2 w}{\partial x^2}\frac{\partial^2 w}{\partial y^2} + 2\frac{\partial^2 w_o}{\partial x \partial y}\frac{\partial^2 w}{\partial x \partial y} - \frac{\partial^2 w_o}{\partial x^2}\frac{\partial^2 w}{\partial y^2} - \frac{\partial^2 w}{\partial x^2}\frac{\partial^2 w_o}{\partial y^2}\right] = 0 \quad (5.2)$$

In this research, it is assumed that the plates are made of perfectly isotropic mild structural steel S235. Isotropic material implies that the directional flexural rigidities $D_x$, $H$, and $D_y$ are the same, and they can be calculated by making use of eq. (5.3). The Poisson ratios in both directions are also equal, $\nu_x = \nu_y \rightarrow \nu$. The elastic shear modulus for isotropic material is given in eq. (5.4). Parameter $\phi$ in these equations represents the Airy stress function on the plate. A stress function relates to individual stresses in a more usable form that satisfies the equilibrium equations. The stress function is obtained by substituting the initial deflection in the compatibility equation eq. (5.2).

$$D_x = H = D_y \rightarrow D = \frac{Et^3}{12(1-\nu^2)} \tag{5.3}$$

$$G_{xy} \rightarrow G = \frac{E}{2(1+\nu)} \tag{5.4}$$

This simplification reduces the equilibrium equation described in eq. (5.1) to eq. (5.5). The compatibility equation in eq. (5.2) reduces to eq. (5.6). The operator $\nabla^4$ is the biharmonic operator, which is the squared Laplacian $\nabla^2$. This set of equations forms the basis of the entire model. The rest of the equations of the model are not further explained in detail, but a short description is given when equations are considered important to discuss.

$$D\nabla^4 w - t\left[\frac{\partial^2\phi}{\partial y^2}\frac{\partial^2\left(w+w_o\right)}{\partial x^2} - 2\frac{\partial^2\phi}{\partial x\partial y}\frac{\partial^2\left(w+w_o\right)}{\partial x\partial y} + \frac{\partial^2\phi}{\partial x^2}\frac{\partial^2\left(w+w_o\right)}{\partial y^2} + \frac{p}{t}\right] = 0 \tag{5.5}$$

$$\frac{1}{E}\nabla^4\phi - \left[\left(\frac{\partial^2 w}{\partial x\partial y}\right)^2 - \frac{\partial^2 w}{\partial x^2}\frac{\partial^2 w}{\partial y^2} + 2\frac{\partial^2 w_o}{\partial x\partial y}\frac{\partial^2 w}{\partial x\partial y} - \frac{\partial^2 w_o}{\partial x^2}\frac{\partial^2 w}{\partial y^2} - \frac{\partial^2 w}{\partial x^2}\frac{\partial^2 w_o}{\partial y^2}\right] = 0 \tag{5.6}$$

The initial deflection, eq. (2.21), and plate deflection function, eq. (2.10), are substituted within the compatibility equation, which makes it then possible to obtain the stress function $\phi$. This stress function is then used to derive an equation that makes it possible to find the deflection amplitude ($A_{mn}$) in eq. (2.10). Depending on the buckling mode, the derived amplitude and applied force are used to obtain the membrane stresses within the structure. Those membrane stresses are used to determine if the von Mises yield criterion is met at multiple locations in the stiffened panel. The lowest applied force that causes failure according to one of the failure criteria is considered the ultimate strength of the stiffened panel. Both the buckling modes and the failure criteria will be discussed in section 5.3.

## 5.2. Geometry, Boundary Conditions and Loading

This section will contain an explanation of the stiffened panel as it is used for the analytical model. The geometry that is adopted for the analytical model is the same as described in section 4.1. The same simply supported boundary conditions will be adopted. It is also assumed that the edges of the stiffened panel stay straight due to its continuous structure. The straight boundary condition is represented in fig. 5.1. The arrows represent the constraints over the edge. The orange arrows represent a rotational constrained over the axis of drawing. The blue arrows represent a restrained displacement over the axis of drawing.

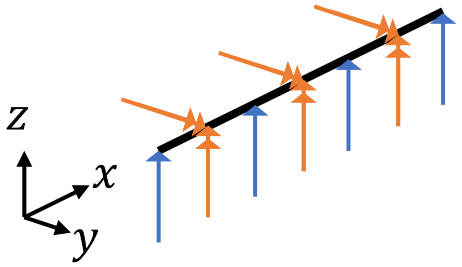

Figure 5.1: Simply supported plate edge with the edge kept straight. Orange arrows represent rotational constraints over that axis of drawing. Blue arrows represent displacement constraints in the direction of drawing.

The stiffened panel is also represented with a top-view in fig. 5.2. The stress ($\sigma_{xav}$) is the averaged uniform distribution of the uni-axial compressive force. Parameter $p$ is the hydrostatic pressure as described in section 4.2.2. The parameter $a$ is the length of the panel, $B$ the full width of the stiffened panel, and $b$ the distance between the individual stiffeners. This research does not take into account that stiffeners could be unevenly spaced over the stiffened panel. Therefore, the spacing of the between the stiffeners is given by eq. (5.7).

$$b = \frac{B}{n_s + 1} \tag{5.7}$$

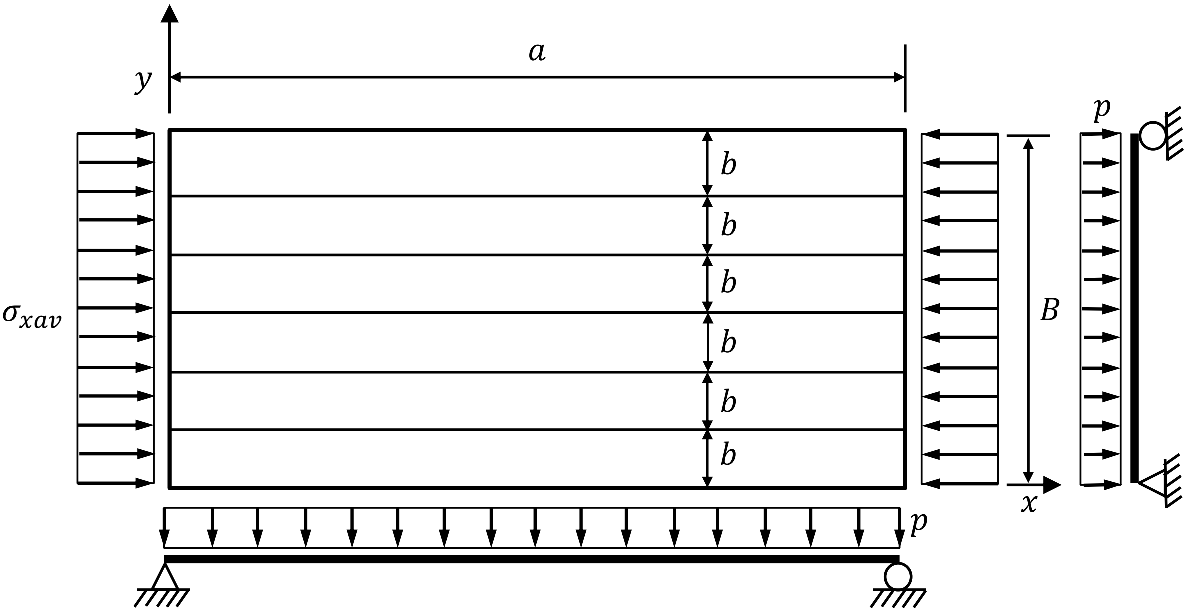

Figure 5.2: Geometry of the simply supported stiffened panel subjected with uni-axial compressive $\sigma_{xav}$ force and lateral pressure $p$.

As mentioned in section 4.1, T-stiffeners will be used in this research. The geometry is given in fig. 5.3. Parameters $b_f$ and $t_f$ are the width and thickness of the flange, respectively. The parameters $t_w$ and $h_w$ represent the thickness and height of the web. The thickness of the plating is denoted by $t_p$.

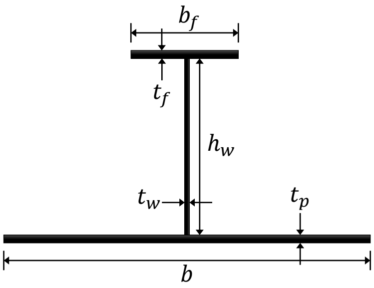

Figure 5.3: Cross-sectional view of the bottom plating and the T-stiffener. The width of the plate is given by $b$ and the corresponding thickness $t_p$. The stiffener has a webheight $h_w$ and a thickness $t_w$. The flange has a breadth $b_f$ and a thickness $t_f$.

## 5.3. Failure Modes

This section describes the failure modes which are often considered within buckling of stiffened panels. Also, the von Mises failure criteria that are assumed for every individual failure mode will be discussed. For the buckling of stiffened plates, five modes of collapse are often assumed. Those buckling modes are displayed in fig. 5.4. In stiffened panels, it is assumed that stresses can redistribute throughout the plate if the boundaries are kept straight. Stiffened panels in literature are often assumed to collapse as soon as the boundaries fail [7]. Therefore, three failure locations are possible where initial yielding can start in the structure. Those locations are displayed in fig. 5.5. Figure 5.5a Represents a failure at the corners of the plate that is related to eq. (5.8a) as failure criteria. Figure 5.5b Represents a failure at the longitudinal edges of the plating. This failure criterion is described with eq. (5.8b). The last possible failure is located at the transverse edge of the plate and is linked to failure criterion eq. (5.8c), which can be seen in fig. 5.5c. The parameters described in those equations are the maximum and minimum membrane stresses in the stiffened panel due to applied force and bending of the structure. If residual stress is incorporated within the model, this will influence the membrane stresses.

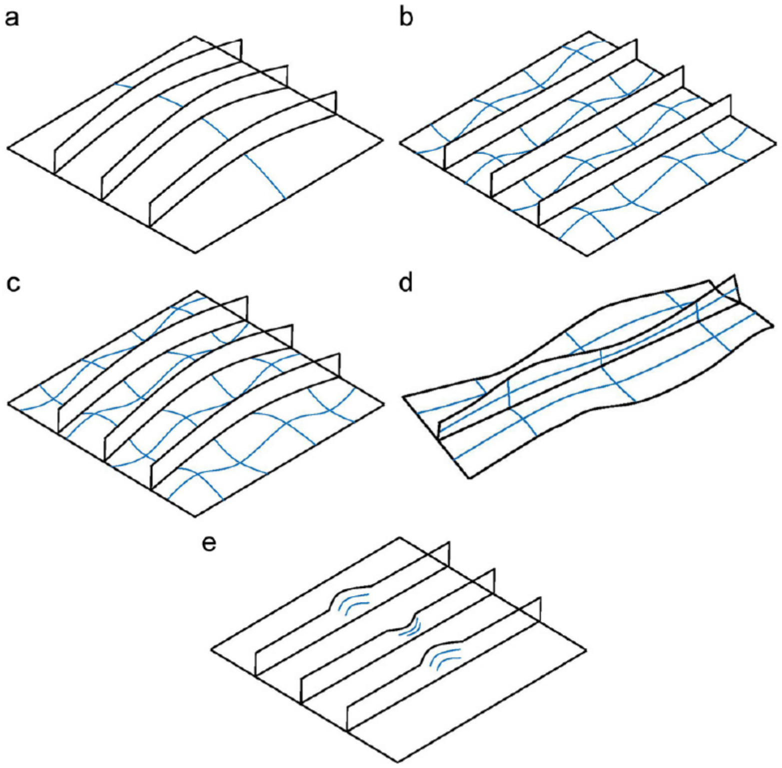

Figure 5.4: Five different failure modes of stiffened panels. (a) Overall buckling of the plate and stiffeners. (b) Buckling of the plating between stiffeners without collapse of the stiffeners. (c) Beam-column type buckling of the stiffener with attached plating. (d) Buckling in the stiffener web. (e) Tripping of the stiffener. Image taken from [31].

$$\sigma_{x,max}^2 - \sigma_{x,max}\sigma_{y,max} + \sigma_{y,max}^2 = \sigma_y^2 \tag{5.8a}$$

$$\sigma_{x,max}^2 - \sigma_{x,max}\sigma_{y,min} + \sigma_{y,min}^2 = \sigma_y^2 \tag{5.8b}$$

$$\sigma_{x,min}^2 - \sigma_{x,min}\sigma_{y,max} + \sigma_{y,max}^2 = \sigma_y^2 \tag{5.8c}$$

The individual modes of failure, displayed in fig. 5.4, will now be discussed.

**Mode 1** is the failure of the entire stiffened panel, sometimes referred to as Euler-type buckling of stiffened panels. Both the plate and stiffeners buckle together. This failure mode is often caused by stiffeners with low stiffness compared to the plate’s stiffness. For this buckling mode, the plate is often simplified by mapping the stiffeners onto the plating such that the stiffened panel can be seen as an orthotropic plate by making use of eq. (5.2). This mode of failure is not specifically linked to one of the failure criteria described in eq. (5.8a), eq. (5.8b) and eq. (5.8c). Therefore, the von Mises failure criteria in all three locations will be tested if they trigger structural collapse. The first criteria that will be satisfied will determine the ultimate strength.

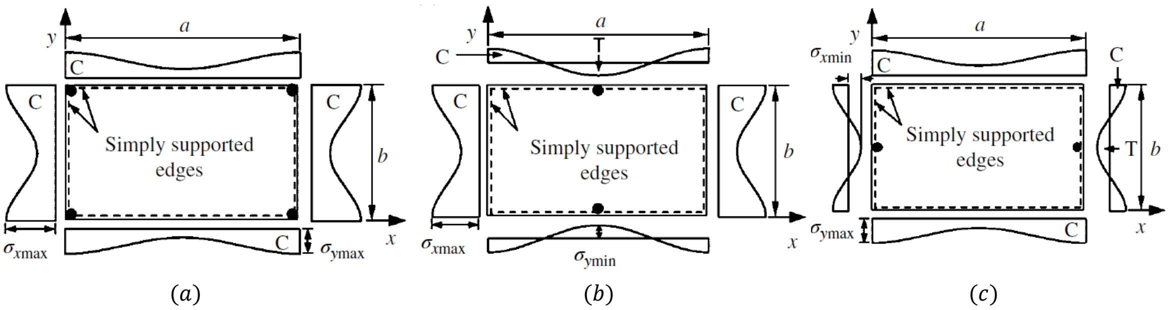

Figure 5.5: Three possible failure locations possible due to membrane stresses. (a) Yielding at the corners of the plate. (b) Yielding at the longitudinal edge of the plating in between stiffeners. (c) Yielding of the transverse edge of the plating in between stiffeners. Image taken from [7].

**Mode 2** is defined by the failure of the plate corners between the stiffeners, also called plate-induced failure. The stiffeners show little to no deflection in this buckling mode. For this failure mode, it is assumed that yielding will start at the corners of the plates between the stiffeners. Therefore only eq. (5.8a) will be tested for this buckling mode.

**Mode 3** is caused by failure in the middle of the plate edges between the stiffeners. For mode 3, none of the failure criteria that have previously been described are used. This failure mode is considered a beam-column type buckling. For this mode of failure, the modified Perry-Robertson formulation can be used since it is assumed that the stiffened panel is subjected to both longitudinal axial compression and lateral pressure [7]. The modified Perry-Robertson equation calculates two minimum values. The first one is related to plate induced failure, and the second one is related to stiffener induced failure. The Perry-Robertson equation is initially not designed to work for stiffened continuous panels. For this reason, it may give low ultimate strength predictions for stiffener-induced failure compared to results obtained with, for example, FEA. For continuous stiffened plates in shipbuilding, stiffener-induced failure is often neglected [7]. In this research, stiffener-induced failure is calculated, but it will only have the purpose of showing the stiffener induced failure behavior. It is not incorporated in the generation of the geometrical parameter set, which is the goal of this analytical model.

**Mode 4** is dominated by the failure of the stiffener's web, also categorized as stiffener induced failure. As soon as plasticity occurs in both the web of the stiffener and the connected bottom plating, the stiffened panel will lose rigidity, which will cause collapse. For this buckling mode, the ultimate strength is determined by an averaging of the plating's ultimate strength as well as the ultimate strength of the stiffeners. The ultimate strength of both the plating and the stiffener will be determined for this buckling mode. The plating's ultimate strength in between the stiffeners is determined with the same principles as mode 2, except eq. (5.8b) will be incorporated as well. Equation (5.8c) will not be incorporated since under longitudinal compression combined with lateral pressure the longitudinal edge will develop plasticity before the transverse edge will [27, 85]. The ultimate strength of the stiffeners is determined by making use of the Johnson-Ostenfeld equation eq. (2.16).

**Mode 5** is caused by tripping of the stiffener, also called flexural-torsional buckling. Tripping causes a rotation of the stiffener around its weld seam. A weighted average of the ultimate strength of the stiffener and ultimate strength of the plating is used to determine the ultimate strength related to mode 5. The same principle is applied as for mode 4. The ultimate strength of the plating between the stiffeners is determined by the same equations used for mode 4. The ultimate strength of the stiffener is determined by applying the Johnson-Ostenfeld equation, eq. (2.16). The flexural torsional buckling strength determines the elastic buckling strength. The flexural torsional buckling strength is different from the elastic buckling strength that is used for calculating the ultimate strength in mode 4.

## 5.4. Initial Deflection and Residual stress

This section describes the initial deflection and residual stress of the stiffened panels used within this analytical model in section 5.4.1. The initial deflection is described for every individual buckling mode. The next section, section 5.4.2, will discuss how the residual stress is implemented for every individual buckling mode.

### 5.4.1. Initial Deflection

As described in section 2.1.4, it is often assumed that the initial deflection is described by a Fourier series in both directions of the panel. For stiffened plate buckling, three types of initial deflection within this analytical model are present. The first initial deflection is the initial deflection of the plating between the stiffeners ($w_{opl}$). The second deflection is the initial deflection of a stiffener due to the entire panel's deflection, also called column-type initial deflection ($w_{oc}$). The third initial deflection is the initial sideways deflection of the stiffener ($w_{os}$). Which initial deflection is taken into account depends on the mode of failure. The initial deflection per mode shape is discussed in section 5.3. Initial deflection tends to lower the ultimate strength of the structure, therefore in all calculations, the maximum initial deflection is assumed, taking the worst-case scenario possible, setting the initial deflection equal to the amplitude of the initial deflection function. Therefore, the amplitude of the initial deflection ($A_{0mn}$), described in eq. (2.21), is often assumed either $w_{opl}$ or $w_{oc}$ depending on the governing mode of failure. The column-type initial deflection is assumed to depend on the length of the stiffened panel, as described in eq. (5.9). The initial sideways deflection of the stiffener is assumed to be equal to the column-type initial deflection. The initial deflection of the plating in between the stiffeners is assumed to be dependent on the plate slenderness ($\beta$) and the plate thickness, as described in eq. (5.10). Classification societies assume the plate initial deflection to be a function $C_1 b$, which for an average level of initial imperfection is assumed to be equal to $0.005b$ [86]. The function used by classification societies tends to give inaccurate initial deflections for thin and thick plates [14]. In contrast, eq. (5.10) should give a good prediction for a much wider variety of thicknesses of plates [7]. In this research, it is not yet known what the thickness range will be. Therefore, eq. (5.10) is used for the initial deflection prediction in this model. This set of equations is based on extensive experimental research, as described in the research of Smith et al. [15].

$$w_{oc} = w_{os} = 0.0015a \tag{5.9}$$

$$w_{opl} = \begin{cases} 0.025\beta^2 t & \text{For slight initial deflection} \\ 0.1\beta^2 t & \text{For average initial deflection} \\ 0.3\beta^2 t & \text{For severe initial deflection} \end{cases} \tag{5.10}$$

Within this research, the average initial deflection is assumed for both the plating in between the stiffeners as for the column-type buckling. This assumption is valid unless other initial deflections are mentioned.

The initial deflection is incorporated within the functions as a single parameter. There is no difference between $w_{oc}$ and $w_{opl}$ within the set of equations. Therefore, it is important to take the correct initial deflection related to every mode of failure. As mentioned in section 5.3, some buckling modes are related to stiffener buckling, and some modes are related to the plating in between stiffeners. Depending on which failure mechanism is dominating the mode of failure, the initial deflection is incorporated that influences this failure mode in the most negative way possible.

**Mode 1** is buckling of the entire stiffened panel. This buckling mode spans the entire width of the panel. Therefore, the worst possible deflection occurs when the top of the column-type initial deflection aligns with the top of the initial deflection of the plating in between stiffeners. Therefore the initial deflection for mode 1 ($w_{o,1}$) is given by eq. (5.11).

$$w_{o,1} = 0.1\beta^2 t_p + 0.0015b \tag{5.11}$$

**Mode 2** is caused by buckling of the plating in between stiffeners. Therefore, only the initial deflection for the plating between the stiffeners is used eq. (5.12).

$$w_{o,2} = w_{o,4p} = w_{o,5p} = 0.1\beta^2 t_p \tag{5.12}$$

**Mode 3** is considered beam-column type buckling. Therefore, the column-type initial deflection is assumed for this buckling mode. The assumed initial deflection ($w_{o,3}$) for both plate and stiffener induced failure is the same and given by eq. (5.13).

$$w_{o,3} = 0.0015a \tag{5.13}$$

**Mode 4** is dominated by the failure of the stiffener web. The ultimate strength of the plating between the stiffeners and of the stiffener itself is determined. The initial deflection of the plating between the stiffeners is the same as for mode 2. The Johnson-Ostenfeld equations and the required elastic buckling strength do not incorporate any initial deflection in the equations.

**Mode 5** uses the same principles that are used within mode 4. For the plating between stiffeners, again, the same initial deflection has been used as in mode 2 and 4. Since the principles of calculating the elastic buckling strength of the stiffener are different than in mode 4, no initial deflections are assumed for the stiffener.

### 5.4.2. Residual Stress

As mentioned in section 2.1.3, residual stress can have a significant impact on the ultimate strength of a stiffened panel. Therefore, it is chosen to incorporate the residual stress within the model to obtain a geometrical parameter set that contains realistic models. Residual stress is incorporated differently depending on the mode of failure. This section will describe how the residual stress is implemented and what the effect is of the residual stress for those buckling modes.

**Mode 1** is buckling of the entire stiffened panel. It is often assumed that residual stress has a negligible impact on the ultimate strength of mode 1 buckling due to the present significant compressive and tensile residual stresses over the entire plate. These stresses are caused by the welding of the stiffeners to the main plating. A significant part of the residual stress will cancel each other out [7].

**Mode 2** is the collapse of the plating between the stiffeners. If only the plating between the stiffeners is considered, residual stress will play a role in the stiffened panel's ultimate strength. Residual stress is incorporated the von Mises failure criteria described by eq. (5.8a). As can be seen in fig. 2.3, the tensile residual force in x-direction ($\sigma_{rtx}$) influences the maximum compressive force in x-direction ($\sigma_{x,max}$) located at the corner of the plate. The same principle applies to the maximum force in the y-direction ($\sigma_{y,max}$). The tensile force counteracts the compressive force, causing the corners of the plate to fail at a higher load compared to when residual stress is not incorporated.

**Mode 3** is the beam-column type failure. Mode 3 is determined by making use of the modified Perry-Robertson equation. This equation does not directly allow the addition of residual stress. A knockdown-factor is applied to the result of the Perry-Robertson ultimate strength prediction. The knockdown-factor is based on the ratio between the equivalent compressive residual stress and the yield stress. When average compressive residual stress is assumed within mild structural steel, the knockdown-factor becomes 1, so it is assumed that residual stress will not influence the result of mode 3 within this research.

**Mode 4** is stiffener-induced failure. Mode 4 is based on the ultimate strength of the plating between stiffeners and the stiffener. For the plating between the stiffeners, the same principles as for mode 2 are used regarding the residual stress. Besides adding residual stress to failure criteria eq. (5.8a), the compressive residual stress in the x-direction also influences $\sigma_{y,min}$ in eq. (5.8b). The residual stress also affects $\sigma_{y,min}$. As described in section 5.3, failure criteria eq. (5.8c) is not adopted when the panel is loaded with longitudinal compression and lateral pressure. If incorporated, it would develop wrong results in the model since it is assumed that the tensile residual stress is equal to the yield strength of the material. When the residual stress is equal to the yield strength of the material, the criteria described in eq. (5.8c) will be met instantaneously since there is no loading present in the transversal direction. The residual stress will not only affect the plating between the stiffeners. The ultimate strength of the stiffener itself will be reduced by the compressive residual stress to incorporate welding residual stress effects in the stiffener.

**Mode 5** is also considered stiffener-induced failure. Mode 5 uses the same principles as for mode 4. The ultimate strength of the stiffener is differently determined than in mode 4 and has two possibilities to be corrected for the ultimate strength. The ultimate strength of the stiffener can be corrected by either the compressive residual stress or by the Danielson compressive correction given in eq. (5.14) [14]. This correction depends on the plate stiffener combination moment of inertia $I$, the spacing between stiffeners, and the bottom plate thickness. The correction represents an effective residual stress factor. The difference between both corrections is only visible at stiffeners, where the height/thickness-ration of the stiffener becomes large. Therefore the simple correction of the compressive residual stress has been used within this model.

$$\sigma^*_{rsx} = \sigma_{rcx}\left(1 + \frac{2\pi^2 I}{b^3 t_p}\right) \tag{5.14}$$

## 5.5. Analytical Model Verification

The model described in Hughes and Paik [7] is widely proven to give an accurate prediction of the ultimate strength. Therefore, it is only necessary to verify that the model is correctly rebuilt and the results that are obtained with the model are in correspondence with the results obtained in literature.

The analytical model is verified by comparing the obtained results with several graphs available from the literature. The graphs from the literature are digitized and compared with graphs obtained by the built model. Figure 5.6a shows the results of all five individual buckling modes. The lines represent the ultimate strength per buckling mode depending on the $h_w/t_w$-ratio. The x-axis shows the ratio between the height of the web and the thickness of the web. The height of the web is varied and the thickness is kept the same through all iterations. The y-axis shows the ratio between the ultimate strength and the yield strength of the stiffened plate. Stiffener induced failure is plotted to compare the results, but it is not taken into account in the final optimization process. Besides the colored lines, the results from the literature are plotted as dotted lines. As can be seen in fig. 5.6a, the graphs show a good similarity between the model and the literature.

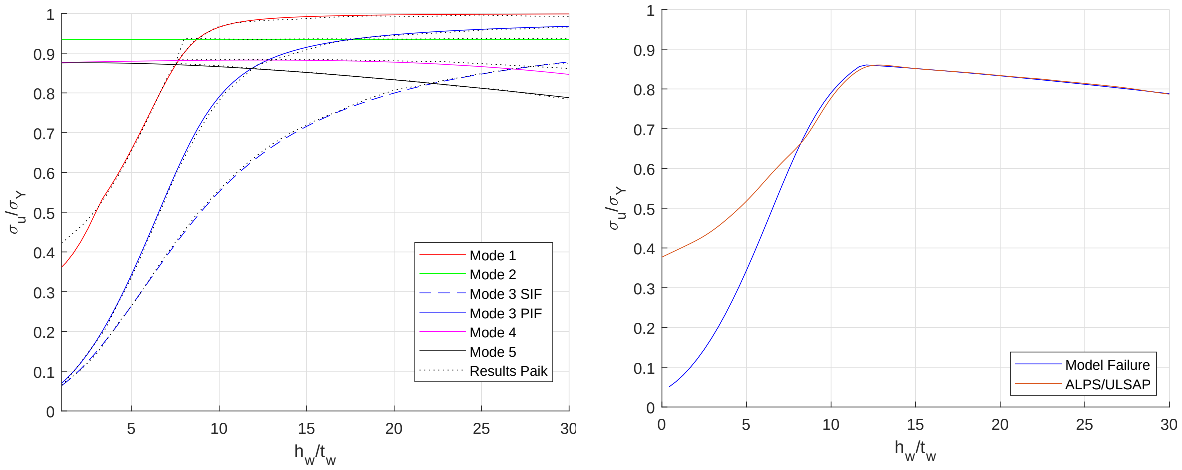

(a) The five different buckling modes compared with results obtained by the models used in literature. Lateral pressure and residual stress are not incorporated.

(b) The Failure curve compared with ALPS/ULSAP results in the literature. Lateral pressure and residual stress not incorporated.

Figure 5.6: Comparison of the model with data available from literature. Plots are for a T stiffened panel: $a$=2640 mm, $B$=3600 mm, $t_p$=21 mm, $n_s$=3, $t_w$=12 mm, $t_f$=15 mm, $b_f$=100 mm, $w_opl$=0.05$\beta^2 t$, $w_{os}$=$w_{oc}$=0.002$b$. Both lateral pressure and residual stress are not incorporated.

Figure 5.6b uses the same axis. From the five different modes in fig. 5.6a, the dominating mode is selected for every $h_w/t_w$-ratio. The dominating buckling mode is the mode that fails the first; this is the buckling mode with the lowest ultimate strength. This line is shown in blue. The failure line is compared to literature results that are obtained with ALPS/ULSAP [85]. The results from the model show good accuracy with the results obtained by ALPS/ULSAP. The results by ALPS/ULSAP is a verified program to perform ultimate strength and limit state analysis of plates and stiffened plates. In this figure, a difference between the results for lower $h_w/t_w$-ratios are observed. This difference is caused by a transition between failure mode 1 and failure mode 3 used in ALPS/ULSAP, ignoring the plate induced failure for low $h_w/t_w$-ratios. This transition is not incorporated into this analytical model.

Few data is available in the present literature about the analytical model that takes residual stress and lateral pressure into account. The model is compared to two ALPS/ULSAP graphs. Both figures in fig. 5.7 use the same geometry as in fig. 5.6. This time the panel is also subjected to lateral pressure, and residual stress is taken into account. Figure 5.7a shows the failure line of a stiffened panel subjected to both longitudinal compression and lateral pressure. A 20-meter water column is used as hydrostatic pressure. The 20-meter water column is also used to obtain the ALPS/ULSAP curves. Residual stress is still neglected in this figure. Again, the model shows great accuracy with the results obtained in ALPS/ULSAP. The only difference is again the transition from failure mode 1 to failure mode 3 in ALPS/ULSAP.

Figure 5.7b shows the failure line for stiffened panels subjected to both compressive residual stress and lateral pressure that is equivalent to a 20-meter water column. Also, compressive residual stress is incorporated within this model. Some deviation can be seen for structures with a $h_w/t_w$-ratio lower than 15. This deviation is caused by the knockdown-factor, as discussed in section 5.4.2, has little influence on mode 3 in the present analytical model. Therefore there is little to no correction for the residual stress in mode 3. For $h_w/t_w$-ratios higher than 15, it can be seen that the current model slightly underestimates the performance of the stiffened panels. The peak in the ultimate strength line is close to the peak in the line obtained with ALPS/ULSAP.

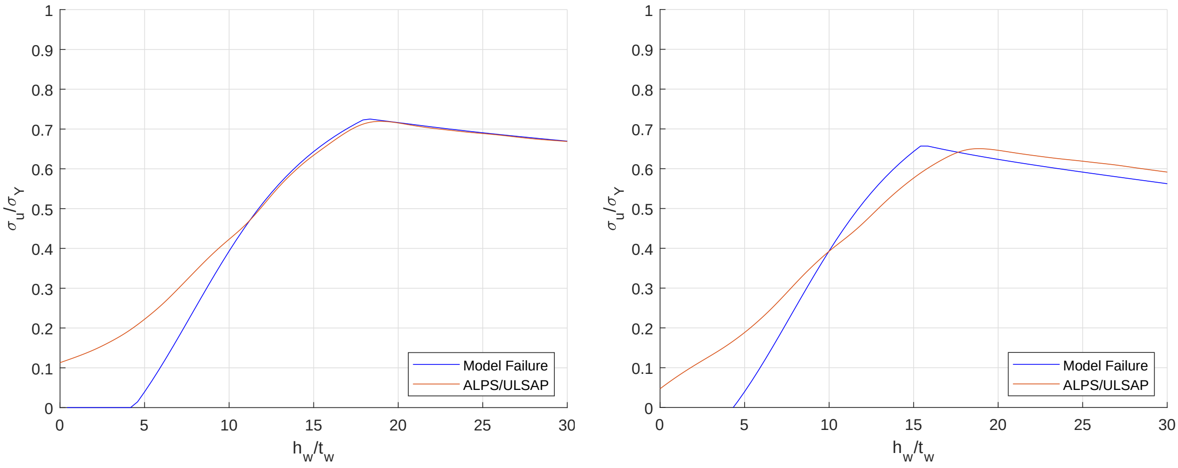

(a) Failure curve compared with ALPS/ULSAP results in literature. 20 meter hydrostatic pressure as lateral pressure added. Residual stress is not incorporated.

(b) Failure curve compared with ALPS/ULSAP results in literature. 20 meter hydrostatic pressure as lateral pressure added. $\sigma_{rcx}$=0.15$\sigma_y$

Figure 5.7: Comparison of the model with data available from literature. Plots are for a T stiffened panel: $a$=2640 mm, $B$=3600 mm, $t_p$=21 mm, $n_s$=3, $t_w$=12 mm, $t_f$=15 mm, $b_f$=100 mm, $w_opl$=0.05$\beta^2 t$, $w_{os}$=$w_{oc}$=0.002$b$. 20m hydrostatic as lateral pressure is added. Residual stress is taken as $\sigma_{rcx}$=0.15$\sigma_y$

Overall it can be said that the model works as it should. It shows near-perfect results if the individual buckling modes are compared with the results obtained in fig. 5.6a. A similar graph with all the individual failure modes is unavailable for stiffened panels subjected to both longitudinal compression and lateral pressure. Therefore, the results are compared with ALPS/ULSAP results from the literature. The application of lateral pressure also shows near-perfect results with the literature. When applying residual stress, small differences are observed in the results, but this can be explained by how residual stress is implemented within the model. Overall, a good similarity is observed between results obtained from the analytical model and the results found in the literature.

## 5.6. Optimization

The previously described analytical model can give an accurate prediction of the ultimate strength of a stiffened panel loaded with longitudinal compression and lateral pressure with residual stress and initial deflection taken into account. Optimization is used to obtain a realistic set of geometrical parameters. Besides that fact that a structure is designed to withstand a specific loading, often the most economically favorable solution will be chosen of all structures that can withstand the required load. The most economical solution will depend on a combination of material costs and production costs. Production costs are difficult to incorporate and are therefore neglected. Since the production costs are neglected, the stiffened panels will be optimized based on the material costs. The pseudocode in algorithm 1 gives the outline of the model. This algorithm determines if the desired ultimate strength ($\sigma_{req}$) has been met for a stiffened panel. Then, the panel's geometry is subjected to some constraints based on rules developed by classification societies to prevent the selection of unrealistic models.

The geometrical range for the optimizer are predefined. The lower and upper bounds are discussed in section 5.6.1. The constraints defined by classification societies and the constraints of the geometry are given in section 5.6.2. The optimization algorithm used and the final obtained parameter set will be discussed in section 5.6.3.

**Algorithm 1** Ultimate strength and weight optimization. First, the ultimate strength for a specific stiffened panel is determined. The predicted ultimate strength is then compared with the requested ultimate strength ($\sigma_{req}$). The structural model is then compared with the limitations by classification societies and geometry. If a solution it passes, it is stored as a suitable model.

```
function ULS-Weight-Predict($n_s, t_p, h_w, t_w, b_f, t_f, \sigma_{req}, E, \sigma_y, \nu, P$)
    Initialize:
        Geometry
        $k \leftarrow$ interpolate $\sigma_y$
        $b \leftarrow B/(n_s + 1)$ Determine stiffener spacing
        $w_{opl} \leftarrow 0.1\beta^2 t_p$ Determine plate initial deflection
        $w_{os}, w_{oc} \leftarrow 0.0015b$ Determine column-type and stiffener initial deflection
    function Mode-1($t_p, b, a, h_w, t_w, b_f, t_f, n_s, w_{opl}, w_{oc}, E, \nu, \sigma_y, P$)
        $m \leftarrow 1; int(1 \dots m)$
        $A_{mn} \leftarrow$ solve
        $\sigma_{x,u} \leftarrow A_m; crit_{VM} = 1, 2, 3$
    function Mode-2($t_p, b, a, w_{opl}, E, \nu, \sigma_y, k, P$)
        $m \leftarrow a/b > \sqrt{m(m+1)}; int(1 \dots m)$
        $A_{mn} \leftarrow$ solve
        $\sigma_{x,u} \leftarrow A_m; crit_{VM} = 1$
    function Mode-3($t_p, b, a, h_w, t_w, b_f, t_f, w_{oc}, E, \nu, \sigma_y, P$)
        $\sigma_{x,u} \leftarrow$ Perry-Robertson equation
    function Mode-4($t_p, b, a, h_w, t_w, b_f, t_f, w_{opl}, E, \nu, \sigma_y, k$)
        $\sigma_{u,web} \leftarrow$ Johnson-Ostenfeld, $\sigma_E^w$
        $\sigma_{u,plate} \leftarrow A_m; crit_{VM} = 1, 2$
        $\sigma_{x,u} \leftarrow \sigma_{u,web}, \sigma_{u,plate}$
    function Mode-5($t_p, b, a, h_w, t_w, b_f, t_f, w_{opl}, E, \nu, \sigma_y, k$)
        $\sigma_{u,web} \leftarrow$ Johnson-Ostenfeld, $\sigma_E^t$
        $\sigma_{u,plate} \leftarrow A_m; crit_{VM} = 1, 2$
        $\sigma_{x,u} \leftarrow \sigma_{u,web}, \sigma_{u,plate}$
    $\sigma_{low} \leftarrow min(\sigma_{x,u})$
    if $\sigma_u < \sigma_{req}$ then
        $solution \leftarrow Rejected$
    else
        if $geo \neq B.C.$ then
            $solution \leftarrow Rejected$
        else
            $savemodel$
```

### 5.6.1. Optimization Parameter Range

The optimizer solves between a predefined range for all the individual geometrical parameters. The limitations used are based on stiffened panels used within different studies on stiffened panels used in shipbuilding. Cases outside this range might occur in reality, but this is done to obtain an initial realistic range of geometrical parameters. The ranges are discussed below:

- Parameters $a$ and $b$, the length and width of the plating betweens stiffeners respectively, are chosen as fixed values. Length $a$ Is chosen to be 2500 mm, $b$ is picked to be 4000 mm. These lengths are based on the research of Paik and Seo [87], where $a$ is 4300 mm, and $b$ is 16000 mm. Both parameters are scaled-down to reduce the size of the FEM models that will later be developed. This is done to reduce the computation time per individual model, allowing for more data to be generated within the same amount of time.
- The number of stiffeners ($n_s$) is based on the research of Paik and Seo [87] as well. The width of the plate is scaled down with a factor four. The down-scaled model would have around 5 stiffeners if compared with the models in the research of Paik and Seo [87]. This number of stiffeners might not be an optimal design, and therefore the optimization is given a significant amount of possibilities by ranging the number of stiffeners from 1 to 10.
- The height of the web ($h_w$) ranges from 50 mm to 500 mm. This range gives the possibility to find small and large stiffeners. Within the literature, often smaller stiffeners are used for cross-stiffened panels. Cross-stiffened panels are panels that have stiffeners in both longitudinal and transverse directions. With only stiffening in the longitudinal direction, sometimes stiffeners beyond 450 mm are used [87].
- The thickness of the web ($t_w$), plate ($t_p$), and flange ($t_f$) are limited by the thinnest plate that is found in the literature, which rounded to 4 mm [85]. Smaller thicknesses are also difficult to produce and are unrealistic in use. The thickest plating found is 25.4 mm thick, a margin is adopted to extend the maximum thickness to 30 mm. [88]
- The flange width ($b_f$) is limited by the minimum plate thickness. It is assumed that the minimum must be a 1:4 ratio between thickness and width. Therefore a lower limit of 20 mm is adopted for $b_f$. The upper limit is based on the maximum that is possible without creating an overlap of the flanges, which is a case where the largest flange and the most number of stiffeners are used. $b$ is 400 mm when the plate has ten stiffeners. Therefore 400 mm will be the upper limit of $b_f$.

### 5.6.2. Limitations and Classification Society

During testing of the optimizer, the optimizer showed to be excellent in exploiting the model, finding some highly unlikely results. Therefore, several constraints are added that are provided by classification societies to improve the stability of the model. The rules defined by classification societies differ slightly between different societies and between vessel types. Since the hydrostatic pressure is taken from the Maersk E class, it is decided that the rules will be adopted for container vessels published by DNV GL.[86] DNV GL is one of the main classification societies related to the maritime industries.

For T-stiffeners, there are some rules defined relating the $h_w/t_w$ and $b_f/t_f$ to a maximum value and the material factor $k$ which is described in table 2.1. Those rules are described in eq. (5.15), eq. (5.16), and eq. (5.17).

$$\frac{h_w}{t_w} \leq 60\sqrt{k} \tag{5.15}$$

$$\frac{b_f}{t_f} \leq 19.5\sqrt{k} \tag{5.16}$$

$$b_f t_f < \frac{h_w t_w}{6} \tag{5.17}$$

Also, a few geometrical constraints are defined in this research that are not based on rules given by any classification society. The first constraint is related to the width of the flange. It is assumed that the flange might span half the width of the spacing between stiffeners. This spacing is assumed because otherwise, it would counter the effect of spatial stiffening, and a closed-form structure could be used. Also, it is assumed that the flange's width must be at least four times the thickness of the flange. Otherwise, the flange will be more of a block welded on top of a stiffener instead of welding a plate on top of the stiffener. The boundaries are displayed in eq. (5.18).

$$4t_f < b_f < 0.5b \tag{5.18}$$

### 5.6.3. Genetic Algorithm and Parameter Set

The optimizer's goal is to find structures that are the can withstand a specific predefined load and are also economical to build. This optimization is done to obtain a representative geometrical parameter set to train the ML model. Six parameters are variable in the optimization process, making it challenging to optimize without using standard available optimizers. The optimizations space turned out to have a significant number of local maxima and minima, making it hard for most solvers to find consistent results. Therefore, a Genetic Algorithm (GA) optimizer has been used within Matlab, which is an evolutionary type algorithm. One advantage of the GA is that it can solve for integers only. The minimal step size of the geometry is set to be 0.1 (mm). The number of stiffeners is equal to the integers 1 to 10. The GA generates a population of randomly picked points on the optimizations space. Then, every randomly selected point gets rated on their performance. The best points will continue to the next generation. Other points will be mutated, and some new points will be a crossing between two other points of the previous generation. This process is repeated until the stopping criteria of the GA are met. For example, if the generations are not getting better or if a runtime limit is reached, the model will stop searching. The stochastic behavior of the optimization in the GA makes that the GA performs well on overcoming local minima most other solvers failed to do, which are gradient-based methods. The downside is that the use of the GA comes at the cost of significant computational time. Therefore, a trade-off has been made between the population size and the required computational time. A larger population size will increase the change of finding the global optimum, while with a small population size the change might be that all points will be close to a local minimum.

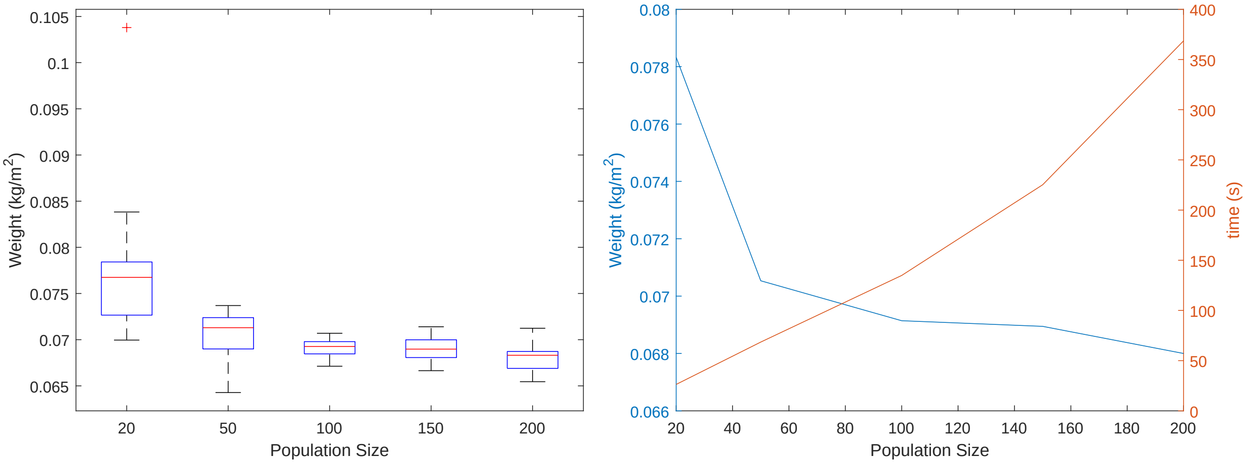

(a) Box plot of the performance of the genetic algorithm per population size. In total, 10 iterations are executed for every population size.

(b) On the blue axis is the mean predicted weight plotted per 10 iterations. On the red axis the mean time is plotted for a single optimum to be found.

Figure 5.8: Performance of the genetic algorithm. In (a) a boxplot is given on the spread of the 10 different iterations. (b) is the mean result plotted against the mean required time to find a single optimum.

The GA is tested with a single stiffened panel with a fixed required strength. One of the parameters defining how the GA works is the population size. The population size describes how many starting points will randomly be distributed on the data optimization space to find an optimum. The GA has been run ten times with a population sizes of 20, 50, 100, 150, and 200. Figure 5.8a shows a box plot of the ten different iterations. It can be seen that with a larger population size, the model has is more likely of finding a local minimum. This behavior can be observed as the large spread of the box and whiskers. It can be seen that with a population size of 100, the spread becomes small, and the algorithm is likely to find a minimum close to the global minimum. From fig. 5.8b, it is observed that an increase in population size significantly increases the computation time for every single solution. For this research, a population size of 100 is chosen since the spread is small, and the required computation time per model is acceptable.

The GA is then used on algorithm 1. Algorithm 1 requires as input an ultimate strength that must be met by the chosen structure. The lower bound of the required ultimate strength is chosen to be 30% of the yield strength of the stiffened panel material. The upper bound is chosen to be 85% of the yield strength. This upper bound is used since it is close to the maximum performance obtained according to testing with the GA. Beyond 85% of the yield strength, the GA is not able to find a solution to the problem that meets all the constraints. This ultimate strength range is subdivided into 200 equally spaced steps. This subdivision means that every loop over the different required forces will result in 200 models. Five loops will be made in total, resulting in a set of 1000 different optimized models. Some iterations the GA failed to find a solution that was according to the boundary conditions or the required ultimate strength. These results were filtered, creating a final set of 960 models. The models where then sorted based on the number of stiffeners $n_s$. The amount of models found per amount of stiffeners is displayed in table 5.1.

Table 5.1: Number of models found per number of stiffeners $n_s$ by the genetic algorithm. The models can withstand a predefined loading ($\sigma_{req}$) and are optimized to have the smallest weight possible.

| Number of Stiffeners | Number of Models |
|---|---|
| $n_s = 3$ | 13 |
| $n_s = 4$ | 225 |
| $n_s = 5$ | 297 |
| $n_s = 6$ | 155 |
| $n_s = 7$ | 41 |
| $n_s = 8$ | 16 |
| $n_s = 9$ | 64 |
| $n_s = 10$ | 129 |

Most of the GA optimized models have either four, five, or six stiffeners. Also, a large group can be observed with 10 stiffeners. The models with 10 stiffeners are all located near the lower bounds of the geometrical parameters. This can be clearly seen in fig. 5.9, fig. 5.10 and fig. 5.11 by the dots which are coloured dark blue. Most of the points are located near the black dotted lines. If the minimum plate thickness is increased from 4 mm to 5 mm, most of the models with 10 stiffeners would be invalid. From all three figures, it can be seen that the parameters show good relations with each other.

Figure 5.9b shows the $h_w/t_w$ plot with the 95% confidence ellipse. The confidence ellipse is drawn to show the spread in both directions of the mean geometry for a certain amount of stiffeners. The confidence ellipse makes clear how well the models are grouped. It can be seen that the points belonging to stiffened panels with 4, 5, or 6 stiffeners show a small spread following a linear relationship. The ellipse of 7 and 8 stiffeners are not drawn because they are too large. The ellipses are too large since geometries belonging to those panels are scattered around in the big and small clusters. It can be seen that a significant amount of the models is capped by the extra constraints described in section 5.6.2. A a substantial number of stiffeners is capped by the line, which prevents too large $h_w/t_w$-ratios. Stiffeners with higher ratios are structures that become prone to tripping.

The figure containing the relation between breadth and thickness of the flange, fig. 5.10, shows that the results are scattered between the boundaries described in section 5.6.2. Figure 5.10a shows that there is a certain diagonal line for the models related to a number of stiffeners that form a ‘lower bound’. The rest is spread from this line over the rest of the cone drawn from the boundary conditions. The diagonal line shifts further up the cone for models with fewer stiffeners. This bound is observed for models with 4, 5, 6, or 7 stiffeners. Those lower bounds are likely caused by a combination of boundaries applied to other parameters of the model. This same behavior can be observed from the confidence ellipses in fig. 5.10b. The width of both ellipses are similar, but they tend to shift further up the cone for models with fewer stiffeners. The models with 8, 9, or 10 models are all located at the tip of the cone.

Figure 5.11 shows the thickness of the bottom plate related to the height of the web. In the figure,

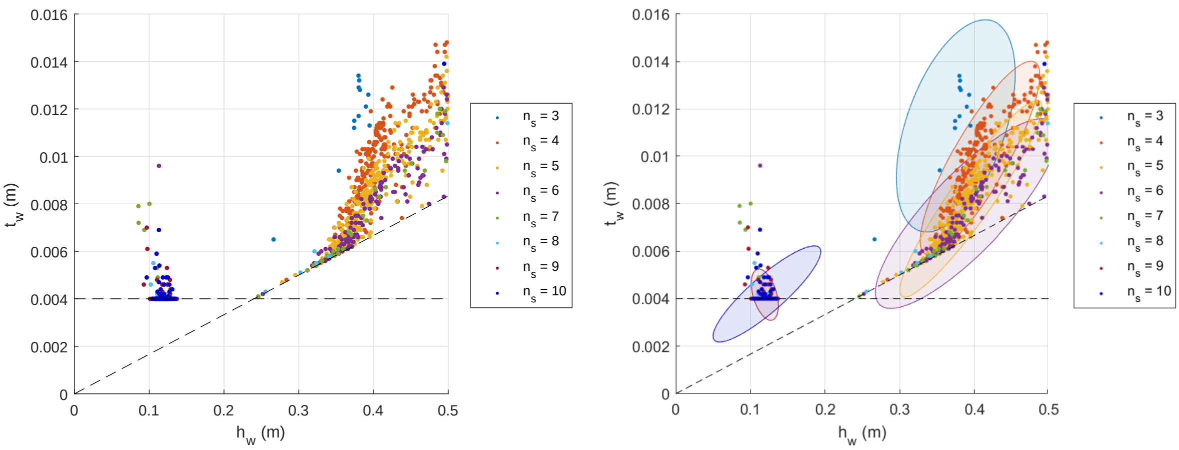

(a) $h_w/t_w$ scatter of the 960 models optimized by the GA. The black line represent the boundary conditions that are described in section 5.6.2

(b) Same plot as (a), but also with the 95% confidence ellipses plotted. The confidence ellipses of $n_s = 7$ and $n_s = 8$ are not plotted since the points are scattered over both clusters.

Figure 5.9: A $h_w/t_w$ scatter of the 960 models optimized by the genetic algorithm. (a) shows the individual points and the boundary conditions. (b) shows the same scatter but with the 95% confidence ellipses drawn to display the grouping of the points.

it can be seen that the results show a similar result as in fig. 5.9a. Again, it can be seen that the minimal plate thickness also caps the models with 10 stiffeners. The diagonal lines in fig. 5.10a can now be observed as horizontal lines, which form a lower bound of the models with 3, 4, 5, and 6 stiffeners. The confidence ellipses of those models are small showing little scatter of the geometrical parameters.

As can be seen in the previously discussed figures, linear trends can be observed. Therefore, a correlation study is applied based on linear regression and the calculation of the Pearson correlation coefficient ($\rho_p$) [89]. The coefficient is a value between -1 and 1, which is calculated by dividing the covariance over the standard deviations. The values -1 and 1 represent a strong linear correlation, negative and positive, respectively. When the correlation factor becomes closer to zero, there is little to no correlation between the parameters.
A correlation plot and matrix are made between every individual parameter. This correlation plot is made on the large group of data points, mainly the models with 6, 5, 4, and 3 stiffeners. The small group near the boundaries of the model is neglected since it is located at the limitations of the model. Therefore, they are considered less likely to occur. Determining the correlation factor with both groups will lead to high correlation factors since the relative standard deviation will decrease, but the linear regression will not be accurate. Outliers are filtered for the same reason. The correlation matrix, with all the individual Pearson correlation coefficients, is given in table 5.2.

Table 5.2: Pearson correlation coefficient matrix for all the different variables within the model. A coefficient of -1 and 1 represents a strong correlation. A correlation near 0 implies that there is no correlation.

| | $t_p$ | $h_w$ | $t_w$ | $b_f$ | $t_f$ | $n_s$ |
|---|---|---|---|---|---|---|
| $t_p$ | 1.0000 | 0.8647 | 0.8695 | 0.8693 | 0.6811 | -0.3697 |
| $h_w$ | 0.8647 | 1.0000 | 0.8355 | 0.6116 | 0.8121 | -0.1146 |
| $t_w$ | 0.8695 | 0.8355 | 1.0000 | 0.6539 | 0.9259 | -0.4260 |
| $b_f$ | 0.8693 | 0.6116 | 0.6539 | 1.0000 | 0.3603 | -0.3674 |
| $t_f$ | 0.6811 | 0.8121 | 0.9259 | 0.3603 | 1.0000 | -0.3144 |
| $n_s$ | -0.3697 | -0.1146 | -0.4260 | -0.3603 | -0.3144 | 1.0000 |

There is no real criterion available when a correlation factor is considered highly correlated. Therefore, the correlation plots are made, drawing the linear regression fitted through the data points. In Appendix A, the correlation plot is given. Low correlation factors are obtained for every parameter related to the number of stiffeners. It is expected that there is a correlation between the number of stiffeners and the

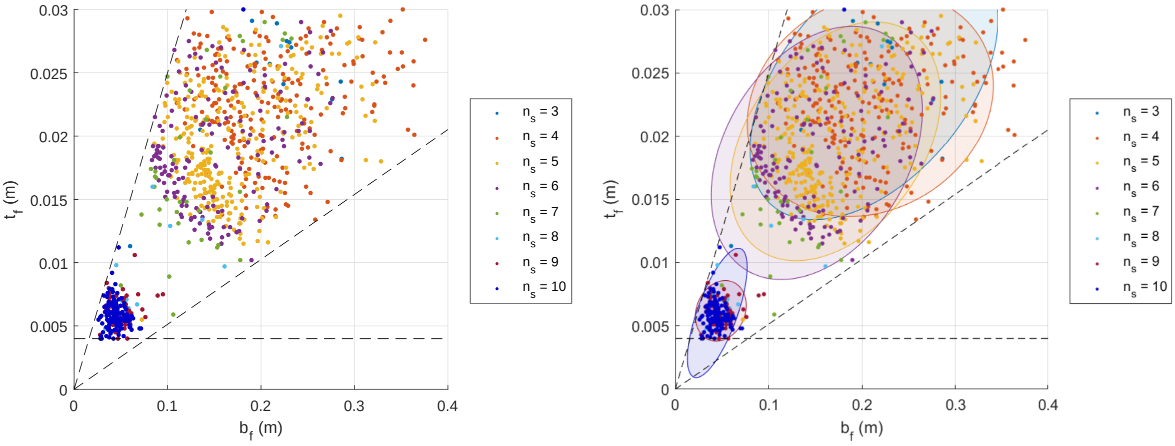

(a) $b_f/t_f$ scatter of the 960 models optimized by the GA. The black line represent the boundary conditions that are described in section 5.6.2

(b) Same plot as (a), but also with the 95% confidence ellipses plotted. The confidence ellipses of $n_s$ = 7 and $n_s$ = 8 are not plotted since the points are scattered over both clusters.

Figure 5.10: $b_f/t_f$ scatter of the 960 models optimized by the genetic algorithm. (a) shows the individual points and the boundary conditions. (b) shows the same scatter but with the 95% confidence ellipses drawn to display the grouping of the points.

other geometrical parameters. This correlation is expected since the number of stiffeners determines the spacing between stiffeners, which plays an essential role in the ultimate strength calculations. Low correlation numbers are obtained because the number of stiffeners is only ranged from 1 to 10, generating the lines in the correlation plot. The parameters with a correlation greater than 0.8 show a good correlation and fit with the linear regression. The parameters that have a coefficient between 0.6 and 0.8 show also some linear trend but are wider spread around the linear regression. Overall it can be concluded that most parameters show a good relationship with each other. Since all parameters show good correlation, it is difficult to obtain an equation that should give ‘optimal’ stiffened panel geometries. Therefore this is not done within this research.

The use of variable-sized input data for ML algorithms is currently possible. However, the use will complicate the ML model significantly. Therefore the choice has been made to use a fixed-sized input for the machine learning models that will be discussed later in this report. The models will have a fixed input size if the number of finite elements in the model is the same. Therefore, the model with the number of stiffeners that occurs the most in the results will be used. This selection will mean that the models with five stiffeners will form the dataset, which will later be used as input for the ML algorithm. The selection only contains 297 models that are generated by the genetic algorithm. A random noise will be added to those 297 models to extend the size of the dataset. A random noise of maximum 10% is added to the existing models. By adding noise the data is extended to 9207 different models.

By adding noise, some of the models are outside the diagonal constraint line. If the models are past the constraint line, they do not comply with regulations described by the classification society. There are two reasons why those models are kept within the research. The first reason is that, as mentioned in section 5.6.2, those rules are vessel-type dependent, and they differ slightly between classification societies. The data points might not fall within the regulations initially applied, but they may be accepted for different vessel types. The second reason is that it will probably improve the accuracy of the data points that do comply with the rules of classification societies. This improvement is because ML algorithms generally show accurate predictions on data within the range of training. If the models outside the boundary condition were not used, a significant amount of the models would lay on the boundary of what the ML algorithm learned. Therefore, the models beyond this drawn boundary condition are still taken into account.

The distributions of every individual geometrical parameter can be found in appendix A. It can be seen that a widespread of every parameter is incorporated, giving an excellent variety of stiffened panel geometries.

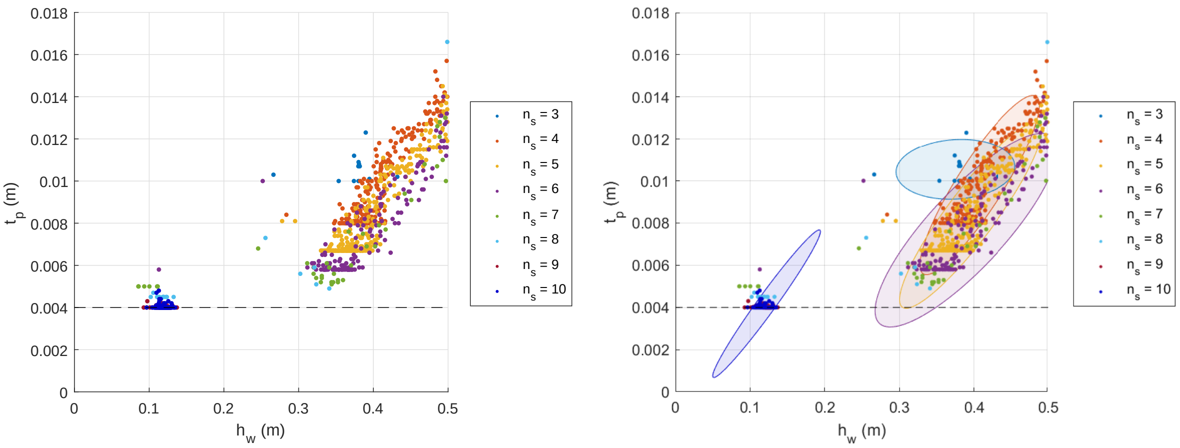

(a) $h_w/t_p$ scatter of the 960 models generated by the GA. The black dashed line represent the boundary conditions that are described in section 5.6.2

(b) Same plot as (a), but also with the 95% confidence ellipses plotted. The confidence ellipses of $n_s = 7$ and $n_s = 8$ are not plotted since the points are scattered over both clusters.

Figure 5.11: $h_w/t_p$ scatter of the 960 models generated by the genetic algorithm. (a) shows the individual points and the boundary conditions. (b) shows the same scatter but with the 95% confidence ellipses drawn to display the grouping of the points.

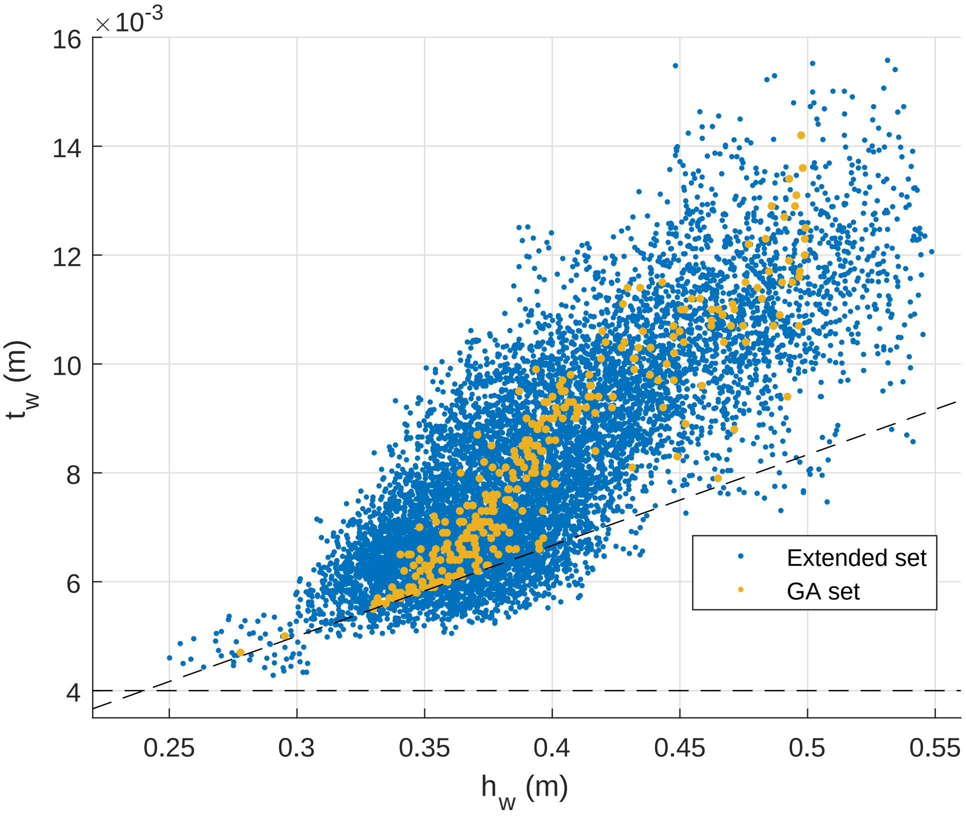

Figure 5.12: $h_w/t_w$ plot of the original data set optimized by the genetic algorithm in yellow. The set is extended to 9207 models by adding random noise to the parameters with a maximum of 10%. Some models are below the constraints, but may be accepted for different types of vessels. Also will the models improve the predictive capabilities of the ML for models that lay on the dotted line. Therefore those models are still accepted within the data set.

# 6

# Numerical Large Deflection Model

This chapter expands upon the data generation, which will be used to train the machine learning (ML) algorithm. In chapter 5, an analytical model is developed to obtain a representative geometrical parameter set. This chapter will describe how this geometrical parameter set is converted to the actual input and output data for the machine learning algorithm. A numerical method will be used to create accurate ultimate strength predictions and obtain stress distributions over the stiffened panel at the moment of failure. The numerical method will be Finite Element Method (FEM), currently one of the most commonly used tools in structural analysis. Finite Element Methods are briefly introduced in section 2.1.6 and section 2.1.7. It is assumed that these sections are prior knowledge to this chapter.

This chapter will start with an introduction of the structural model in section 6.1. Next, the use of eigenvalue buckling and why this is performed in this research will be discussed. This elaboration can be found in section 6.2. After explaining the eigenvalue buckling, the quasi-static analysis used within this research will be explained in section 6.3. Since all the analyses are executed many times, this process will be automated. How this process is automated is described in section 6.4. In the last section, the Finite Element Analysis (FEA) results will be verified and validated in section 6.5.

## 6.1. Finite Element Model

This section will describe the structural model. The geometry will be discussed in section 6.1.1. The material properties of the model and the mesh elements used are discussed in section 6.1.2. Finally, a mesh convergence study is performed to obtain quick solvable models with an acceptable loss of accuracy. The results of the mesh convergence study are given in section 6.1.3.

### 6.1.1. Geometry

The geometry used in this analysis will be the same as described in section 5.2. In section 3.2, it became clear that all kinds of different setups are available to model the boundary conditions as realistically as possible. Section 4.1 made clear that it is not straightforward to model the boundary conditions of continuous stiffened panels. In reality, the boundaries behave if they are partially rotation restrained, which is complex to model. Therefore, the current analysis practice is to extend the stiffened panel in both longitudinal and transverse directions by adding half bays and spans so the partial rotation restrained behavior of the large longitudinal and transverse stiffeners can be incorporated. By adding the half bays and spans, the model size becomes more than four times larger, significantly increasing computational time. Therefore only 1-bay and 1-span will be used in this FEA analysis.

### 6.1.2. Material and Element Properties

The material that will be used in the model is mild structural steel S235. The material properties are given in table 4.1. For the quasi-static analysis, non-linear material properties also have to be added to the model. These non-linearities will require the tangent modulus ($E_t$) to be added. The tangent modulus is difficult to determine correctly. In ultimate strength analysis, elastic-perfectly plastic material properties are often assumed. Elastic-perfectly plastic implies that the material is free to flow without the effect of hardening. It turned out that using an elastic-perfectly plastic material with $E_t$ set to zero, performs less stable than a material with a low conservative tangent modulus of 0.1% of the Young's modulus. The average difference obtained in the ultimate strength of elastic-perfectly plastic material with a tangent modulus of 0.1% of the Young's modulus compared to elastic-perfectly plastic material with a tangent modulus of 0 is around 0.05%. This approach is also used in other studies, like the research of Li et al. [90].

For the modeling of thin-walled structures, shell elements are often used instead of solid elements. Shell elements follow the theory of thin plates, while solid elements also incorporate the lateral direction the same as the longitudinal and transverse direction. Due to the requirement for fewer elements, shells are computationally more efficient than solid elements. Modeling thin structures with solid elements might also cause difficulties in the computations performed. For this research, Ansys is used as FEM.

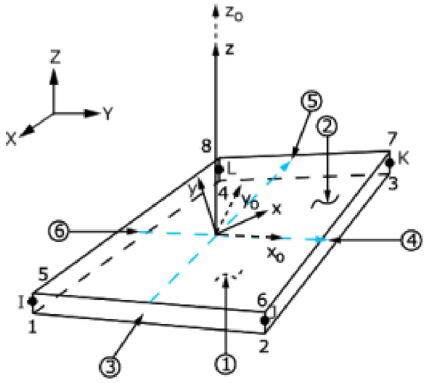

Figure 6.1: A graphical representation of the first-order shell181 element used in Ansys. Four nodes can be observed at the corners of the element. Image taken from [16]

The element shell181, a first-order shell element capable of large displacements, strains, and rotations was used. The shell181 element is graphically represented in fig. 6.1. An alternative is the second-order element shell282. Both first- and second-order elements are tested on several stiffened panel models, and no significant difference in results is obtained. Therefore shell181 elements are chosen. Five through-thickness integration points were used due to better accuracy during large deformations [16]. The standard number of through-thickness integration points is three.

### 6.1.3. Mesh Convergence

The mesh density of the model is an essential factor for the accuracy of the prediction. A higher mesh density will often yield a more accurate prediction of the stresses and deformations in most cases. More elements in the model also increase the size of the stiffness-matrix calculated in FEA, being the reason for an increase in computation time and expense. The numerical models used in this research are used as input for the machine learning model. Because a substantial amount of data is required to obtain a well trained ML model, it is desired to have a mesh that has low computational time but also yields accurate results. Therefore, a mesh convergence study is performed.

For the T-stiffened panel in this research, four different edges can have different mesh sizes. The mesh division in the longitudinal direction ($a$), in the transverse direction ($b$), over the height of the web ($h_w$), and over the width of the flange ($b_f$). Square elements are used to mesh the model. The mesh convergence is applied to a stiffened panel selected from the dataset developed in chapter 5. The material parameters are the same throughout the mesh convergence study and are displayed with the geometrical parameters in table 6.1.

The chose mesh has: 20 elements over the stiffened panel length ($a$), 10 elements over width ($b$), 8 elements for both the height of the web ($h_w$) and the width of the flange ($b_f$). These are determined by performing the mesh convergence study. This study is done by varying the individual mesh densities of just one of the parameters, or by varying multiple parameters with a similar ratio. While changing the mesh density on one or two sides, the mesh density on the other sides is kept the same. The y-axis in all the graphs will have the same values. The y-axis is kept the same to make the difference between the individual graphs more clear. It is noted that a smaller number of elements in the model overestimates the ultimate strength prediction. Therefore, a lower $\sigma_u \backslash \sigma_y$ ratio in the upcoming graphs implies better performance.

Table 6.1: Geometrical and material properties of the stiffened panel used in the mesh convergence study. The material used is mild structural steel S235.

| Parameter | Value | Units |
|---|---|---|
| $\sigma_y$ | 235 | MPa |
| $E$ | 206 | GPa |
| $E_t$ | 206 | MPa |
| $a$ | 2.5 | m |
| $b$ | 0.667 | m |
| $h_w$ | 0.338 | m |
| $t_w$ | 0.0057 | m |
| $b_f$ | 0.149 | m |
| $t_f$ | 0.0133 | m |

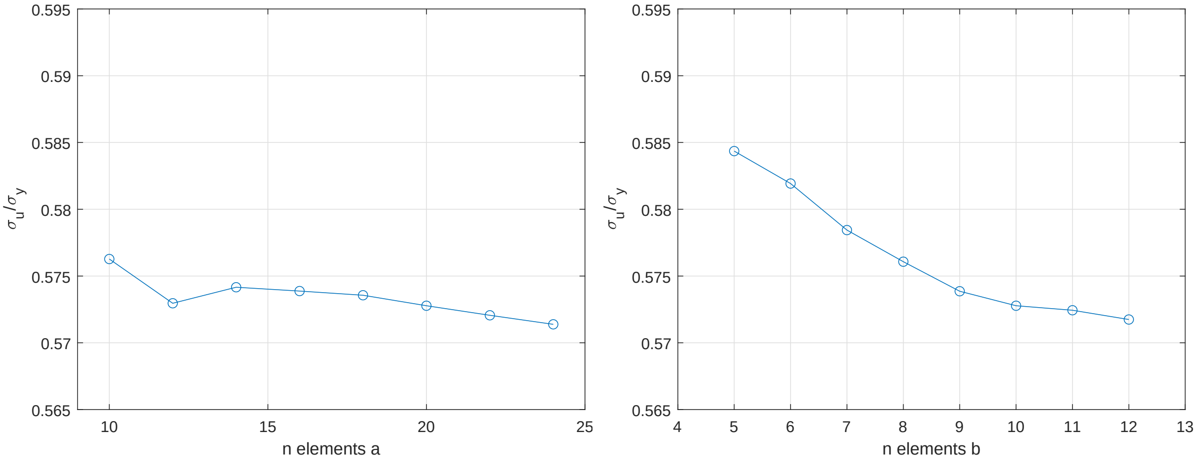

(a) Number of elements over the longitudinal edge of the plating in between stiffeners plotted against the ratio between ultimate strength and the yield strength of the parent material.

(b) Number of elements of the transverse edge of the plating in between stiffeners plotted against the ratio between ultimate strength and the yield strength of the parent material.

Figure 6.2: Mesh convergence plot of the plating in between the stiffeners. (a) shows the mesh convergence of the number of elements on the longitudinal edge of the plating. (b) shows the mesh convergence of the number of elements on the transverse edge of the plating.

First, a mesh convergence has been performed on both the longitudinal and transversal edge of the plating between stiffeners. The results are displayed in fig. 6.2. Figure 6.2a shows the influence of the mesh density on the longitudinal edge of the plating between stiffeners. The mesh density is tested with 10 to 24 elements over that edge. The mesh density is increased in steps of two elements. It can be concluded that the mesh density on the longitudinal edge does not significantly influence the obtained ultimate strength. It can be seen that more elements slightly increases the prediction. Figure 6.2b shows the effect of the number of elements on the transversal edge. Mesh densities with 5 to 12 elements are tested with steps of one element. It is observed that increasing the number of elements significantly improves the predicted ultimate strength. The curve slightly flattens when more than 10 elements are used.

Next, the influence of the mesh density in the stiffener is tested in fig. 6.3. First, the number of elements is changed in the direction of the height of the web. The results are displayed in fig. 6.3a. The range of elements used is 2 to 16 elements in steps of two elements added per step. Also, an improving curve can be seen in this graph. The curve tends to flatten with more than 8 elements; only a small increase in performance is observed with more elements. From fig. 6.3b, it can be seen that there is little improvement made by adding more elements over the width of the flange. The number of elements over the width of the flange is varied from 2 to 12 elements in steps of adding two elements.

With the change of individual mesh densities, elements vary between long rectangles and squares. For this reason, it might be that the previously-discussed graphs do not represent the ef-

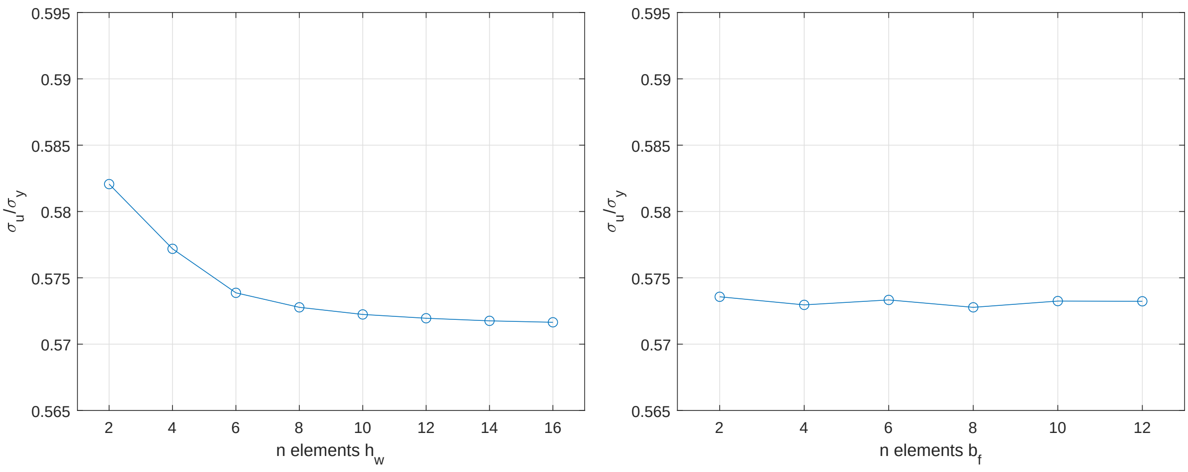

(a) Number of elements over the height of the web plotted against the ratio between ultimate strength and the yield strength of the parent material.

(b) Number of elements over the breadth of the flange plotted against the ratio between ultimate strength and the yield strength of the parent material.

Figure 6.3: Mesh convergence plot of the stiffener. (a) shows the mesh convergence of the number of elements on the height of the web. (b) shows the mesh convergence of the number of elements on the width of the flange.

fect of mesh density completely. Therefore, a mesh density study is also performed by varying the mesh density on both the longitudinal and transverse edge of the plating between stiffeners simultaneously. The number of elements on the x-axis represents the number of models on the longitudinal edge only. The number of elements on the transverse edge is the number of elements on the longitudinal edge halved. The results are displayed in fig. 6.4a. A significant decreasing curve can be observed. It is essential to mention that by increasing the mesh density on two edges, the number of elements in the model increases exponentially, increasing the required computation time quadratically. The mesh density in the flange and web is also varied at the same time. The results are displayed in fig. 6.4b. An improving curve can be observed, which flattens out around 8 elements for both the height of the web and the flange's width.

Figure 6.2b shows flattening of the curve beyond 10 elements. Figure 6.2a shows little improvement by adding more elements in the longitudinal direction. However, fig. 6.4a shows a decreasing curve with even more elements beyond 10 elements in the transverse direction. Therefore, it can be concluded that the elements' rectangular shape also influences the performance of the model. Therefore, 20 elements in the longitudinal direction and 10 elements in the transverse direction are used within the final models. Adding more elements still increases the accuracy of the final result but also exponentially increases the computation time. Beyond the chosen setup, the computational time increases significantly compared to the accuracy increase achieved. With 20 and 10 elements in the length and width of the plating between stiffeners, an error of 4.3% is obtained. This error is based on results that are obtained using a model with a high mesh density. The obtained error is considered acceptable for the current research. The curve of fig. 6.4b flattens out beyond 8 or more elements. Although fig. 6.3b shows no improvement by adding more elements, it is chosen to have the same amount of elements in both the flange and the web. This choice is made because the tested model has the most deflection in the bottom plating and the web of the stiffener. The deflection in the flange is limited. The effect of mesh density on the flange is expected to play an important role similar to that is observed in all other mesh density parameters when a model will develop large deflections in the flange. For this reason, the final mesh density has been picked.

## 6.2. Eigenvalue Buckling

This section will give a short overview of the eigenvalue buckling analysis that has been performed. Section 2.1.6 already made clear why eigenvalue buckling is used; to obtain the initial deflection for the quasi-static analysis. This section will discuss the used boundary conditions and how they are implemented within Ansys in section 6.2.1. The loading conditions will be described in section 6.2.2.

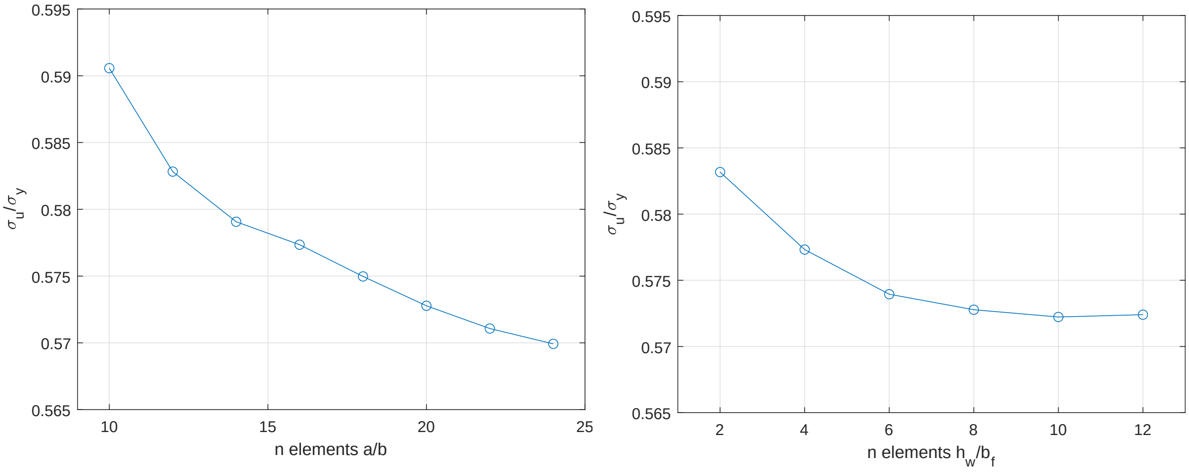

(a) Number of elements over the longitudinal edge of the plating plotted against the ratio between ultimate strength and the yield strength of the parent material. The number of elements on the transverse edge is half the number of elements on the longitudinal side.

(b) Number of elements over the height of the web and width of the flange plotted against the ratio between ultimate strength and the yield strength of the parent material.

Figure 6.4: Mesh convergence plot of the stiffener and the plating in between stiffeners. (a) shows the mesh convergence of the number of element on both the longitudinal and the transverse edge. There are always twice the number of elements on the longitudinal edge. (b) shows the mesh convergence of the number of elements on the height of the web and the width of the flange. The number of elements on both edges is the same.

At last, a description is given about how the results from eigenvalue buckling are used to obtain the initial deflection for the quasi-static analysis in section 6.2.3.

### 6.2.1. Boundary Conditions

The boundary conditions used for the FEM are the same as described in section 5.2. However, section 5.2 only mentions the boundary conditions at the edges of the bottom plate. Also, boundary conditions must be applied on the stiffeners' sides, as can be seen in fig. 6.5. The face of the stiffened panel at $x = 0$ is prevented from moving in x (longitudinal) direction ($u_x = 0$). The face is constrained because only one face of the stiffened panel is loaded, as described in section 6.2.2. Also, the entire face is restrained from rotating around the x-axis ($\theta_x = 0$). This boundary condition is applied since the stiffener is, in reality, welded to a large transverse frame preventing rotation around the x-axis. The edge of the bottom plating on this face of the stiffened panel is prevented from moving in z-direction due to the simply supported plate edges ($u_z = 0$). The boundary conditions for this face of the model also make sure the edges remain straight during deformation.

The face of the stiffened panel at $x = a$ has different boundary conditions since this is the face that will be loaded with compressive force. The face is prevented from rotating around the x-axis ($\theta_x = 0$). The edge of the bottom plating is prevented from moving in the z-direction ($u_z = 0$). The movement of the face is coupled in the x-direction for all nodes on the face. The coupling makes sure the edges remain straight during loading. The edges remain straight because all nodes move with the same displacement in the x-direction ($u_x = coupled$). Coupled nodes follow the displacement of the node with the lowest node number.

The edges at $y = 0$ and $y = B$ have the same boundary conditions. The sides are allowed to move in-plane but have to remain straight. Preventing rotation around the y-axis and the z-axis keeps the edges straight ($\theta_y = \theta_z = 0$). Also, the displacement in the z-direction is constrained. The displacement in the z-direction is constrained to impose simply supported boundary conditions ($u_z = 0$).

Since none of the stiffened panel edges are constrained to move in the y-direction, rigid body motion can occur. Rigid body motion is when the entire stiffened panel starts to move through space since it is not adequately constrained. The origin of the model is constrained to move in the y-direction to prevent rigid body motion ($u_y = 0$). The boundary conditions are displayed in fig. 6.5. Only the node coupling of the nodal displacement in the x-direction is not displayed on the face of side A-B; this would make the other boundaries difficult to show. The boundary conditions are also summarized in table 6.2.

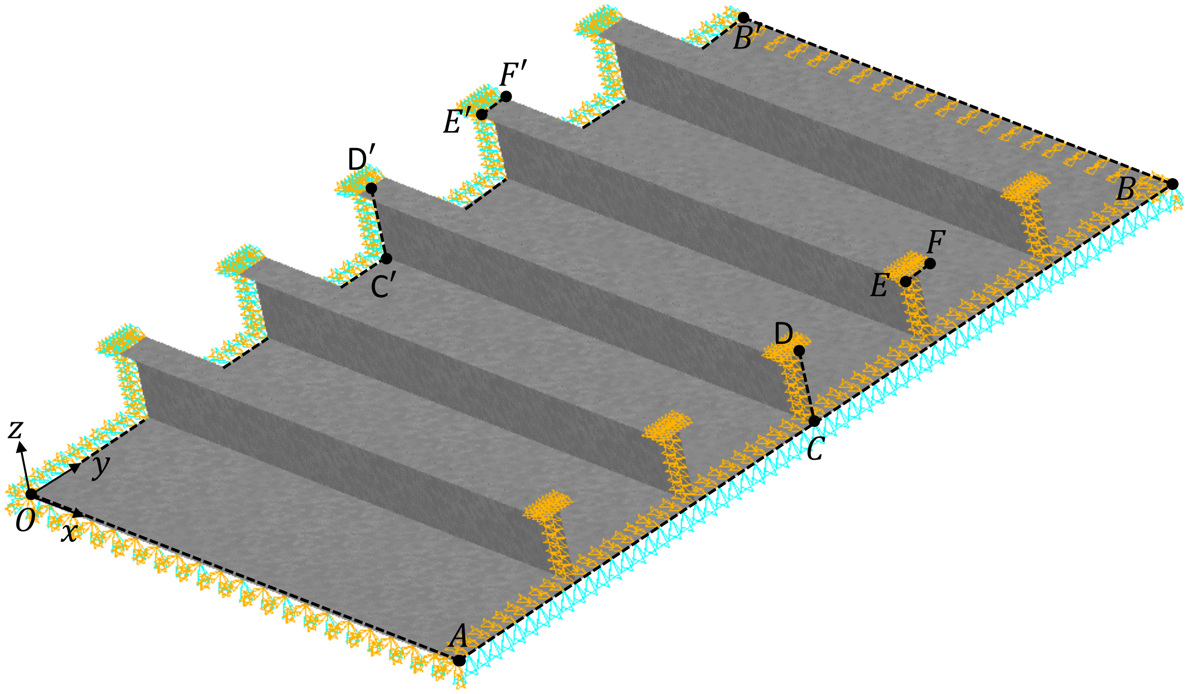

Figure 6.5: Boundary conditions of the eigenvalue stiffened panel in Ansys. Orange arrows indicate a rotational restrained in the direction of pointing. Blue arrows indicate a displacement constrained in the direction of pointing.

Table 6.2: Boundary conditions for the stiffened panel used for eigenvalue buckling analysis

| Segment | Constrained |
|---|---|
| Line C'-D', E'-F' | $u_x = \theta_x = 0$ |
| Line C-D, E-F | $\theta_x = 0$ |
| Line O-B' | $u_x = u_z = \theta_y = \theta_z = 0$ |
| Line B'-B, O-A | $u_z = \theta_y = \theta_z = 0$ |
| Face A-B | $u_x = coupled, u_z = 0$ |
| Node O | $u_y = 0$ |

### 6.2.2. Loading Conditions

This research looks into stiffened panels subjected to both longitudinal uni-axial compression and lateral pressure, as mentioned in section 4.2. In FEA, one side of the stiffened panel is often prevented from moving in the direction of loading, the other side of the panel is loaded. These boundary conditions prevent rigid body motion. For eigenvalue buckling, it does not matter what the actual magnitude of the applied load is, since the results consist of normalized eigenvectors. The magnitude becomes essential when there are loads applied that do interact with each other. The longitudinal compression and lateral pressure both influence the ultimate strength of the stiffened panel. Therefore, it is essential to apply the correct ratio between the magnitude of the compressive force and the lateral pressure. The compressive force is the dominant buckling force and is set equal to the material's yield strength. Because the model is made of shell elements, it is impossible to model the compressive force as a pressure on the edges of the stiffened panel. The compressive force is added as a line force over the loaded edges of the panel. Since it is a line load, the pressure load must be projected onto the edges of the shell by multiplying it with the thickness of the structure. The web may have a different thickness than the bottom plating. Therefore, the pressure is projected on the edge by multiplying it with the weighted average thickness of the material. The lateral pressure is equal to a 16-meter water column. The magnitudes described are used in the eigenvalue analysis of this research. The ratio between the compressive force and lateral pressure could be determined more accurately, but this would require an iterative procedure. The compressive load can iteratively be changed to obtain an eigenvalue of close to one. When the eigenvalue is one, it means that the applied loads will exactly cause the structure to buckle. Since the lateral pressure is constant, this will result in the perfect ratio between compressive and lateral loads. There is no easy solution to obtain a more accurate ratio between the loads than solving it with an iterative process. Therefore, it is assumed that the initial deflection predicted with the current load ratio will be accurate enough to perform the quasi-static analysis.

### 6.2.3. Initial Deflection

The main goal of the eigenvalue buckling analysis is to obtain the initial deflection of the stiffened panel. The same initial deflection equations will be used as the one described in section 5.4.1. Average initial deflection is assumed. The results obtained from eigenvalue buckling are normalized eigenvectors containing a maximum value of one. This maximum value is either displacement or rotation. The obtained results need to be scaled to the correct initial deflection amplitude before it can be used as the stiffened panel's initial deflection. In the analytical model, three types of initial deflection were assumed. The fact that three types of initial deflection are assumed makes the process of scaling difficult. Thus, it is assumed that the plating between stiffeners will contain deflections or rotation equal to one in the eigenvalue. After performing the eigenvalue buckling, the most significant deflection of the bottom plate nodes will be obtained. This deflection is scaled to have the maximum amplitude of the average initial deflection in eq. (5.10). The factor required for scaling will be applied to all the deflections obtained with the eigenvalue buckling analysis. The scaled deflection will form the initial deflection for the quasi-static buckling analysis.

## 6.3. Quasi-Static Analysis

This section will describe the model used to obtain the prediction of the ultimate strength and the corresponding stress distribution over the plate at the moment of failure. Quasi-static buckling analysis is shortly discussed in section 2.1.7. A quasi-static analysis is an analysis where the displacements and forces are incremented with small steps. These load steps cause the inertial terms to become negligibly small and thus simplifies the analysis performed. The application of boundary conditions and loading is slightly different than during eigenvalue buckling due to the non-linear behavior and pushing the structure beyond failure. Therefore, those two topics are discussed in section 6.3.1 and section 6.3.2, respectively. In the final section, section 6.3.3, how the ultimate strength is obtained from the analysis will be discussed.

### 6.3.1. Boundary Conditions

The boundary conditions of the stiffened panel are, for the most part, the same as discussed in section 6.2.1. In eigenvalue buckling, which is a linear analysis, it is sufficient to allow in-plane movements over the edges O-A and B-B', indicated in fig. 6.5, and forcing those edges to remain straight with rotational constraints. During non-linear analysis, which the quasi-static analysis is, this can lead to unstable results. Sometimes, individual nodes at the boundaries tend to move unexpectedly. Thus, the in-plane movement is coupled with the nodes on the opposite side of the stiffened panel. With the node coupling, every node will have the same deflection in edge normal direction as the node on the opposite edge. This coupling still allows the stiffened panel to deform in-plane but forces it to deflect with the same magnitude and prevents unexpected results from individual nodes. In this coupling the opposite nodes follow the same deflection and the nodes do not follow the node with the lowest node number. This response is also in line with the fact that both sides of the stiffened panel are generally connected to another stiffened panel. The origin is constrained as in the eigenvalue buckling analysis to obtain stability. Due to the coupled in-plane deflection, it is not needed to restrain the rotation around the z-axis for edge O-A and B'-B. The boundary conditions are summarized in table 6.3.

### 6.3.2. Loading Conditions

The loading conditions are different from the eigenvalue buckling analysis. In eigenvalue buckling analysis, a constant force is applied. For quasi-static analysis, applying a force is not suitable. Instead of applying a force on the structure, enforced displacement will be used to obtain the maximum applicable force. This way, it is possible to push the structure beyond the ultimate strength into the post-buckling regime.

The stiffened panels in this research are loaded with both longitudinal uni-axial compression and

Table 6.3: Boundary conditions for the stiffened panel used for quasi-static buckling analysis.

| Segment | Constrained |
|---|---|
| Line C'-D', E'-F' | $u_x = \theta_x = 0$ |
| Line C-D, E-F | $\theta_x = 0$ |
| Line O-B' | $u_x = u_z = \theta_y = \theta_z = 0$ |
| Line B'-B, O-A | $u_y = coupled, u_z = \theta_y = 0$ |
| Face A-B | $u_x = coupled, u_z = 0$ |
| Node O | $u_y = 0$ |

lateral pressure. The lateral pressure is always present in this research, and it is assumed that the panel is loaded under compression due to the hogging of the ship. For this reason, the load is applied in two stages for the quasi-static analysis. The lateral pressure is instantaneously initiated at the first time step. The enforced displacement will then be slowly incremented after the lateral pressure is applied. This order of loading prohibits the model from failing at a lateral pressure lower than the hydrostatic pressure.

### 6.3.3. Ultimate Strength

The force-displacement curve is required to obtain the ultimate strength of the structure. The reaction force at the nodes of the enforced displaced face is used to obtain the force-displacement curve. Dividing the total reaction force on that face by the surface area of the entire face, the applied stress on the face of the stiffened panel can be obtained. The peak of the force-displacement curve represents the ultimate strength of the stiffened panel.

Near the ultimate strength, the buckling analysis might become unstable when using Newton-Raphson solvers, which are often standard in FEA. This instability is due to the rapid increase in deflections and rotations by yielding of the structure when assuming elastic-perfectly plastic material properties. To correctly obtain the ultimate strength of the stiffened panels, the arc-length method, as described in section 2.1.7, is used.

## 6.4. Automation

The dataset obtained in chapter 5 consists of 9207 models. Therefore, automation of the entire buckling analysis is required. Ansys saves the results of an analysis at every single load step. The process is capped by storage and write/writing processes on the hard drive. Therefore, the data generation is run in batches of 24 models at the same time.

First, the required parameters of the FEA model will be loaded by the automation algorithm. These consist of the geometry parameters, the material parameters, and the mesh properties. After defining the geometry, the mesh will be created. These geometry files are automatically generated in Python based on the input parameters of the structural model. Next, files are created that contain the analysis information and the boundary conditions for the eigenvalue buckling. The eigenvalue buckling analysis is then executed to obtain the eigenvalues and the corresponding buckling mode-shapes. The mode-shape with the lowest eigenvalue is then extracted and stored. The mode-shape is loaded, and all the nodes corresponding with the bottom plating are selected. The node with the highest deflection is selected, and a scaling factor $\zeta_{\lambda,min}$ is determined such that the scaled deflections comply with eq. (5.10).

It is now possible to update the geometry with the scaled initial deflection. The updated geometry forms the input for the quasi-static analysis. A file containing the updated geometry, boundary conditions, arc-length parameters, applied lateral pressure, and load/time steps are generated. The quasi-static analysis is performed, and the stress distributions, deformations, applied force, and displacement at every load step are stored. The maximum force and the stress distribution at the time of maximum force is then found and stored. All other unnecessary data will be removed. The initial mesh, ultimate strength, and stress distribution at the moment of failure are then all known. This process is schematized in algorithm 2.

In this process, the FEA may fail to produce the requested results. One of the major issues is when Ansys fails to converge when solving a model. This will cause Ansys to terminate and save

**Algorithm 2** Overview of the automation of the finite element analysis. First the geometries are generated from the geometrical parameters. Then the eigenvalue code is generated and executed obtaining the initial deflection. The initial deflection is scaled and stored for the quasi-static analysis. The quasi-static analysis is performed and the required data is stored.

```
for $i = 1 : n_{models}$ do
    Initialize:
        Geometry: $a, b, t_p, h_w, t_w, b_f, t_f, n_s$
        Material properties: $E, E_t, \nu$
        Mesh properties: $a_{msh}, b_{msh}, h_{w,msh}, b_{f,msh}$
    $Geo.ans, Geo\_qs.ans$ ← Write APDL geometry and mesh files
    $Eig.ans$ ← Write APDL eigenvalue analysis file

    $Run$ → Perform eigenvalue analysis ← Store deflections and eigenvalues
    $\lambda_{min}$ ← Retrieve lowest eigenvalue
    $u_{\lambda,min}(x, y, z), \theta_{\lambda,min}(x, y, z)$ ← Retrieve corresponding deformations and rotations
    $\zeta_{\lambda,min}$ ← Obtain initial deflection scaling factor

    $Qs.ans$ ← Write APDL quasi-static with correct scaling of initial deflection
    $Run$ → Perform quasi-static analysis ← Store data
    $F_u, t_u$ ← Obtain ultimate strength from reaction force and the corresponding load step
    $Save, del$ → Store the required data, delete all other data
```

the results before the structure's ultimate strength is reached. Therefore, the force-displacement data is checked to see if the last value generated is the highest value of the load-displacement data. If this is the case, the model did not run beyond the ultimate strength, resulting in a high probability that the results are incorrect. This model is rejected and run again with different load increments to see if convergence can be obtained. If this is not the case, the model is entirely rejected and not incorporated in the final dataset.

There is also the risk that the numerical analysis cannot solve a time step but also does not meat the criteria of non-convergence. To prevent the analysis from running excessively long, Python monitors the total running time and terminates the process if it takes to long to execute. These models are re-initiated with a different load increment to see if convergence can be obtained.

## 6.5. Verification and Validation

It is important to validate the results obtained from FEA with results from both experiments and FEM results of other studies. It is also important to look at the estimates given by the many available empirical and analytical sets of equations. The validation of this study is based on an experimental set of stiffened plates subjected to either only axial compression or a combination of axial compression and lateral pressure in the research performed by Smith et al. [15]. These are the models 1a to 7 in table 6.4. Three FEM models from the research of Li et al. [91] are also used, displayed by the Y models in table 6.4. The developed FEA models are run with the geometry and material properties described in table 6.5. The results are displayed in table 6.4. This table also displays the results that are available from the literature. Also, the analytical models of Zhang and Khan [92], Faulkner [93] are used to obtain an estimate for the ultimate strength. The empirical formula from Paik [14] is also used as a comparison. For the models 1a to 7, also ULSAP results are available in the research of Paik et al. [85].

The Faulkner equation, Zhang's equation, and Paik's empirical equation are given by eq. (6.1) [93], eq. (6.2) [92], and eq. (6.3) [14], respectively. In table 6.4, the last column is the average of the three equations mentioned. This average value is also used because, for some of those equations, the predicted values are significantly different. It is also important to note that all three equations are for longitudinal uni-axial compression only. Since the lateral pressure in the models is low, the equations are still used as an indicator.

$$\left(\frac{\sigma_{xu}}{\sigma_y}\right)_F = \frac{2}{\beta} - \frac{1}{\beta^2} \tag{6.1}$$

$$\left(\frac{\sigma_{xu}}{\sigma_y}\right)_Z = \frac{1}{\beta^{0.28}}\frac{1}{\sqrt{1+\lambda^{3.2}}} \tag{6.2}$$

$$\left(\frac{\sigma_{xu}}{\sigma_y}\right)_P = \frac{1}{\sqrt{0.995 + 0.936\lambda^2 + 0.170\beta^2 + 0.188\lambda^2\beta^2 - 0.067\lambda^4}} \tag{6.3}$$

The plate slenderness coefficient $\beta$ and the stiffeners slenderness coefficient are given by respectively eq. (6.4) and eq. (6.5)

$$\beta = \frac{b}{t}\sqrt{\frac{\sigma_y}{E}} \tag{6.4}$$

$$\lambda = \frac{a}{\pi\rho}\sqrt{\frac{\sigma_y}{E}} \tag{6.5}$$

For the stiffener slenderness coefficient, the radius of gyration $\rho$ is needed, which requires the cross-sectional area of the stiffener and plating, given by eq. (6.7). Also, the cross-sectional moment of inertia of the stiffener with plating is required, which can be determined by making use of eq. (6.8) and eq. (6.9).

$$\rho = \sqrt{\frac{I}{A}} \tag{6.6}$$

$$A = bt_p + h_w t_w + b_f t_f \tag{6.7}$$

$$z_0 = \frac{0.5bt_p^2 + h_w t_w\left(t_p + 0.5h_w\right) + b_f t_f\left(t_p + h_w + 0.5t_f\right)}{bt_p + h_w t_w + b_f t_f} \tag{6.8}$$

$$I = \frac{bt_p^3}{12} + bt_p\left(z_o - \frac{t_p}{2}\right)^2 + \frac{h_w^3 t_w}{12} + h_w t_w\left(z_o - t_p - \frac{h_w}{2}\right)^2 + \frac{b_f t_f^3}{12} + b_f t_f\left(t_p + h_w + \frac{t_f}{2} - z_o\right)^2 \tag{6.9}$$

Table 6.4: Ultimate strength ratios for validation of the FEM model. Results are compared with the analytical formulas from Faulkner [93] and Zhang and Khan [92], the empirical formulation of Paik [14], ULSAP and experimental results from Paik et al. [85], Smith et al. [15], and Li et al. [91]

| Structure | $\left(\frac{\sigma_{xu}}{\sigma_y}\right)_{FEM}$ | $\left(\frac{\sigma_{xu}}{\sigma_y}\right)_{lit}$ | $\left(\frac{\sigma_{xu}}{\sigma_y}\right)_F$ | $\left(\frac{\sigma_{xu}}{\sigma_y}\right)_Z$ | $\left(\frac{\sigma_{xu}}{\sigma_y}\right)_P$ | $\left(\frac{\sigma_{xu}}{\sigma_y}\right)_U$ | $\left(\frac{\sigma_{xu}}{\sigma_y}\right)_{FPZ}$ |
|---|---|---|---|---|---|---|---|
| 1a | 0.66 | 0.76 | 0.61 | 0.76 | 0.67 | 0.76 | 0.68 |
| 1b | 0.70 | 0.73 | 0.60 | 0.75 | 0.67 | 0.62 | 0.67 |
| 2a | 0.93 | 0.91 | 0.91 | 0.90 | 0.86 | 0.79 | 0.89 |
| 2b | 0.92 | 0.83 | 0.89 | 0.89 | 0.85 | 0.79 | 0.88 |
| 3a | 0.86 | 0.69 | 0.84 | 0.87 | 0.83 | 0.69 | 0.85 |
| 3b | 0.88 | 0.61 | 0.84 | 0.87 | 0.83 | 0.58 | 0.85 |
| 4a | 0.95 | 0.82 | 0.92 | 0.91 | 0.87 | 0.80 | 0.90 |
| 4b | 0.94 | 0.83 | 0.92 | 0.91 | 0.87 | 0.81 | 0.90 |
| 5 | 0.61 | 0.72 | 0.52 | 0.72 | 0.60 | 0.52 | 0.61 |
| 6 | 0.63 | 0.49 | 0.50 | 0.71 | 0.58 | 0.37 | 0.60 |
| 7 | 0.59 | 0.65 | 0.48 | 0.70 | 0.56 | 0.52 | 0.58 |
| Y3 | 0.62 | 0.64 | 0.57 | 0.74 | 0.64 | - | 0.65 |
| Y4 | 0.72 | 0.73 | 0.58 | 0.75 | 0.65 | - | 0.66 |
| Y8 | 0.67 | 0.67 | 0.67 | 0.79 | 0.72 | - | 0.73 |

If the results obtained with the developed FEM model are compared to the experimental results, it can be observed that the FEM model, in most cases, overestimates the ultimate strength of the structure.

The reason for this might be that no residual stress was incorporated within the FEM models, but the research by Smith et al. [15] mentions significant compressive residual stresses that negatively influence the ultimate strength. So it is expected that the FEA will overestimate the ultimate strength of the stiffened panel. Similar results can be found when comparing the obtained results with the ULSAP results. The results obtained in the research of Li et al. [91] shows excellent agreement with the results obtained within this research. When the results are compared with the estimates from both the analytical and empirical models, a good agreement between the results of this research and the predicted estimates can be observed. The obtained results show on average the best agreement with the empirical equation given in eq. (6.3).

For some of the models, a significant difference between the predicted values by the different analytical and empirical models is observed. Thus, the results from the analytical and empirical models are averaged and compared with the obtained FEA results. Nearly all obtained results are within 5% of the average estimate ultimate strength.

Table 6.5: Geometries of the stiffened panels used for validation of the FEM model. Geometries are taken from Smith et al. [15] and Li et al. [91]

| Structure | $a$ (m) | $b$ (m) | $t_p$ (m) | $h_w$ (m) | $t_w$ (m) | $b_f$ (m) | $t_f$ (m) | $n_s$ (-) | $\sigma_y$ (Mpa) | $P$ (Pa) |
|---|---|---|---|---|---|---|---|---|---|---|
| 1a | 1.219 | 0.610 | 0.008 | 0.154 | 0.007 | 0.079 | 0.014 | 6 | 2.52 | 0 |
| 1b | 1.219 | 0.610 | 0.008 | 0.152 | 0.007 | 0.076 | 0.014 | 6 | 2.56 | 103421.4 |
| 2a | 1.524 | 0.305 | 0.008 | 0.116 | 0.005 | 0.046 | 0.010 | 11 | 2.70 | 48263.32 |
| 2b | 1.524 | 0.305 | 0.007 | 0.114 | 0.005 | 0.045 | 0.010 | 11 | 2.73 | 0 |
| 3a | 1.524 | 0.305 | 0.006 | 0.078 | 0.005 | 0.026 | 0.006 | 11 | 2.48 | 20684.28 |
| 3b | 1.524 | 0.305 | 0.006 | 0.077 | 0.005 | 0.028 | 0.006 | 11 | 2.48 | 0 |
| 4a | 1.219 | 0.254 | 0.006 | 0.077 | 0.005 | 0.028 | 0.006 | 3 | 2.50 | 0 |
| 4b | 1.219 | 0.254 | 0.006 | 0.077 | 0.005 | 0.026 | 0.006 | 3 | 2.51 | 55158.08 |
| 5 | 1.524 | 0.610 | 0.006 | 0.116 | 0.005 | 0.046 | 0.010 | 6 | 2.44 | 0 |
| 6 | 1.219 | 0.610 | 0.006 | 0.076 | 0.005 | 0.027 | 0.006 | 6 | 2.55 | 0 |
| 7 | 1.524 | 0.610 | 0.006 | 0.115 | 0.005 | 0.045 | 0.010 | 6 | 2.85 | 0 |
| Y3 | 0.800 | 0.300 | 0.004 | 0.025 | 0.006 | 0.025 | 0.013 | 8 | 3.15 | 0 |
| Y4 | 0.900 | 0.360 | 0.005 | 0.040 | 0.010 | 0.025 | 0.014 | 8 | 3.15 | 0 |
| Y8 | 0.780 | 0.320 | 0.005 | 0.025 | 0.006 | 0.025 | 0.014 | 8 | 2.73 | 0 |

It can be concluded that the model shows good agreement with the analytical and empirical estimates. Also, an excellent agreement is obtained compared with other FEA results from the literature. An overestimation is observed on the real experimental data. Because compressive residual stress was not incorporated in the developed FEM model, this is expected. Therefore, it is accepted that the developed FEM model gives results as expected.

# III

# Machine Learning

# 7

# Prediction of Structural Failure

The optimization process described in chapter 5 and the numerical analysis performed in chapter 6 are all part of the generation, which is required to train the machine learning model (ML). From executing the numerical analysis, the following information is obtained: The meshed geometry of the stiffened panel, the ultimate strength of stiffened panels by incorporating initial deflections and non-linear material properties, and the stress distribution over the entire stiffened panel at the moment of failure.

The obtained data is used to train a Convolutional Neural Network (CNN). In section 7.1, it is explained what the goal of the developed ML model is. In the next section, section 7.2, it is described how the developed model is built and how the individual components are chosen. Section 7.3 will describe what assumptions are made regarding the learning process of the ML model. In this section the used optimizer and loss functions will be discussed. The next section, section 7.4, will explain the obtained results of the developed ML model. It is also important to obtain information on how well the model performs on data that is not within the scope of training, the so-called scalability. The scalability will be explained in section 7.5. After the discussion on the scalability of the model, the developed ML model's performance is tested with different amounts of available trainings data, see section 7.6. The ML model is also tested on curved stiffened panels to check whether the model is capable of generalization in section 7.7. At the end of the chapter, the conclusions of the developed ML-model and the obtained results are given in section 7.8.

## 7.1. Model Definition

Before developing a ML model, it is essential to determine what data will be used for the ML model to train and what the model's output data looks like. The shape of the input and output data will influence what type of ML is suitable and what kind of model architecture should be used.

As the title of the report says, the goal of this research is to predict the ultimate strength and stress distribution at the moment of failure of meshed stiffened panels. In section 2.2, it became clear that the ultimate strength is a numerical value, so the problem is considered a regression problem. A wide variety of regression models is available. Accurately predicting the ultimate strength is a highly non-linear process that depends on many different parameters for which FEA is often used. Therefore, the choice has been made to make use of a Neural Network (NN), which can be used as a versatile regression method to perform non-linear regression analysis. By changing the architecture of a NN, a whole different regression performance can be obtained, giving the developer many different possibilities to solve complex regression problems. As explained in chapter 6, the input for the numerical analysis is the geometry of the stiffened panel. This introduces multiple possibilities for the input of the ML model.

It is also possible to use a Deep Neural Network (DNN) as described in section 2.2, which has the geometrical and material parameters as individual input parameters for the ML model. It is expected that this is a suitable option, but it has a significant downsides regarding further research and generalizability. The dataset developed in Part II of this research contains only flat T-stiffened panels with the same material used for both the plating and the stiffeners because they are one of the primary building blocks of many ships as well as offshore structures. The panel is only stiffened longitudinally with a fixed spacing, while a stiffened panel can also be cross-stiffened or have different spacing between the individual stiffeners. If it is desired to extend the data with curved stiffened panels that do not have evenly distributed stiffeners, it becomes difficult to put this information in single parameters. Because this type of ML model will not be easily extendable for further research, it will not be used within this research.

Another option would be to use the entire mesh of the stiffened panel as input for a DNN and not only the individual geometrical parameters. A plain plate meshed with 10 nodes will already have 30 values related to the individual nodes' locations: 10 points related to x-coordinates, 10 points related to the y-coordinates, and 10 points related to the z-coordinates. When adding more parameters to the model, this would significantly increase the size of the input. A solution to large input data is to use Principal Component Analysis (PCA) as used in the research by Liang et al. [75]. The PCA maps the input data to a small vector; a compact representation of the initial data. This compression could be a viable option, although there is a drawback to this solution; the loss of spatial information. In a mesh, the nodes adjacent to each other will interact and influence the results of both nodes. This interaction between nodes in the mesh will be lost when making use of standard DNNs. Since this interaction is an essential factor for structures, it is chosen not to use this model.

Using the geometrical data of all the individual nodes in the mesh is a good way of incorporating spatial information, which is not possible when using individual geometrical and material parameters as input. CNNs can maintain spatial information between the individual data points, as described in section 2.2.2, which makes it an excellent alternative to the application of DNNs. Keeping this spatial information is possible because CNNs uses kernels that 'slide' over the data, keeping information on the surrounding data points. A single point in the output can contain information about a significant amount of surrounding points in the original set, which is called the receptive field, as described in section 2.2.2. Kernels are also explained in that section. Since CNNs can capture spatial information and is efficient in handling large-sized input, it is chosen to use CNNs within this research. The input that will be used is the mesh of the stiffened panel.

CNNs are developed to operate on images. An image consists of pixels with color. Let us assume a figure of $10 \times 20$ pixels. RGB values define colors in a picture. The RGB colors contain three values representing the amount of red, green, and blue in an image. This data means the input data of an image is $10 \times 20 \times 3$ large. The mesh of a structure can be seen as the same sort of data, a mesh of $10 \times 20$ nodes. The RGB values can be compared to the x-, y- and z-coordinate of the mesh, giving a $10 \times 20 \times 3$ large data set. CNNs can also function for more than three layers of information. These 3-D layers are called channels. Since CNNs can handle more than three layers, it is also possible to add a channel with the material properties or the thickness of the structure at that node. In this way, it is possible to incorporate a significant amount of information in a 'figure'-like data set, which would be difficult to do with a standard NN where all data is split in individual points of information. Also, the CNN includes the spatial information which results in choosing this type of model within this research.

In this research, only flat T-stiffened panels are used as data for the ML to train. The material is assumed isotropic over the entire model. For this reason, the following parameters are incorporated in the input data:

1. The x-coordinate of the node.
2. The y-coordinate of the node.
3. The z-coordinate of the node.
4. The thickness of the material at the location of the node.

These parameters will result in a dataset of the size $n \times m \times 4$, where $n$ and $m$ are the dataset's length and width. This dataset can be extended to incorporate material properties by adding more channels to this dataset.

The desired output of the model should be the ultimate strength of the stiffened panel. The output could be the total reaction force obtained in section 6.3, but this total reaction force could also be converted to the ultimate applied stress. This conversion is done by dividing the total reaction force by the cross-sectional area where the total reaction force is obtained. In this research, both types of output have been tested.

## 7.2. Model Architecture

Now that the shape of the actual input and output is known, the model architecture can be discussed. The shape of the architecture will be similar to the ones often used in literature. The input data will be fed to a series of convolutional and pooling layers that will transform the data into a compressed dataset. This compressed dataset contains values that are a representation of the original dataset. Compression is performed to reduce the number of parameters in the network [94]. This process is often called data-encoding and is described in section 7.2.1. After the encoding process, this reduced data will put through a flattening layer. The flattening layer reshapes the multidimensional data from the convolutional layers to a single array. This flattened array then forms the input to a series of fully connected layers, which will finally produce the ultimate strength of the input data. This process is described in section 7.2.2. A schematic overview of the model architecture is given in fig. 7.1.

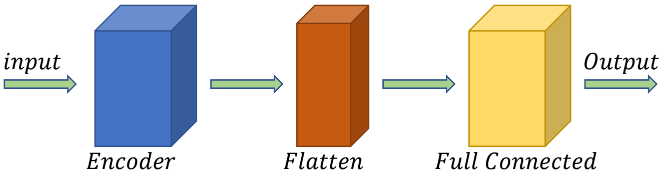

Figure 7.1: Basic overview of the ML model that is used for predicting the ultimate strength of a stiffened panel. In blue the encoder is represented. In orange the flattening module which transforms the data to the input for the fully connected layers represented by the yellow block.

### 7.2.1. Geometry Encoder

The input data for the ML model has a significant size. As mentioned in section 6.1.3, the stiffened panel has 10 elements over the width of the plating between stiffeners. Over the length of the panel, 20 elements are present. In the height of the web, 8 elements are used. The same amount of elements is present over the width of the flange. Nowadays, convolutional layers are developed, which could be applied to 3-D spaced data [95]. This 3-D spaced data means that the actual data will be 4-D when multiple channels are used. If the example in section 7.1 would be extended from a plate to a block of $10 \times 20 \times 10$ nodes and the coordinates of the individual nodes are added as data, that the data would become $10 \times 20 \times 10 \times 3$, which is 4-D data. The stiffened panel is a 3-D structure, so made up of 3-D spaced data. The stiffened panel can be considered a sparse structure. A sparse structure means that if a stiffened panel would be placed in a box, the largest part of the space will be filled by air, so it would not contain much data. Due to the sparse nature of the stiffened panels, it is chosen not to use 3-D convolutional layers. Using 3-D convolutional layers will be viable when the structure would contain more material or if the structure has a complex shape.

The stiffened panels in this research are entirely built with rectangular plates. Therefore the mesh obtained by FEA is transformed into a 2-D data set. This transformation is done by transposing all the stiffener webs to the right side of the bottom plating, rotating them horizontally. When all the webs are transposed to the xy-plane of the bottom plating, the similar process will be repeated for the stiffeners' flanges. It is not required to rotate the flanges because they are already oriented in the xy-plane. By this procedure, the 3-D stiffened panel is transformed into a 2-D data plate. The dataset contains stiffened panels with five stiffeners. With the previously mentioned mesh densities, it can be seen that the bottom plating contains $60 \times 20$ elements. All the webs together will contain $40 \times 20$ elements, and the flanges together will also contain $40 \times 20$ elements. If these are transformed together, a $140 \times 20$ dataset is obtained from the stiffened panel. Instead of using the elements as data, the nodes will be used. The set will contain the nodes' coordinates and the corresponding thickness, as described in section 7.1. This means that the input data's size is $141 \times 21 \times 4$ nodes, which is 11,844 individual data points. The data $(141 \times 21 \times 4)$ is difficult to divide by two, which is useful when using convolutional layers. Therefore, the dataset is extended by adding zeros to all the sides of that data to transform it into a $144 \times 24 \times 4$ data set. Zero-padding the data is also essential to prevent loss of information on the edges of the data. The amount of zero-padding is described by eq. (2.32). The convolutional layers use $3 \times 3$ kernels with a stride of 1. After a convolution, the data is padded to the input size of the convolutional layer. For the convolutional layers, it can be seen that with a $3 \times 3$ kernel and stride of 1, padding of 1 is needed. The original is padded with either 1 or 2 zeros on the edges to turn it into the required shape $(144 \times 24 \times 4)$, so no information will be lost at the edge of the panel and the number are dividable by two.

The best practice is to normalize or scale the input of NNs. The weights and biases in the model are standardly initialized with random values between -1 and 1. They perform best for inputs that are close to this range. Without normalizing or scaling the input, it takes longer to adapt the weights to the correct weight [96]. Normalizing, as described in eq. (7.1), is often used when input data uses consists of different units. In this dataset, everything is in meters, therefore, it is chosen to scale the input by the largest value in the dataset, which is represented by $x_{scaled} = x/x_{max}$.

$$x_{norm} = \frac{x - x_{min}}{x_{max} - x_{min}} \tag{7.1}$$

The dataset is put through a series of convolutional and pooling layers to keep the spatial information and reduce the number of parameters. The series of layers is shown in fig. 7.2. In blue are the convolutional layers represented, and in purple are the pooling layers represented. If the reader is not known with convolutional layers and pooling layers, it is recommended to read section 2.2.2.

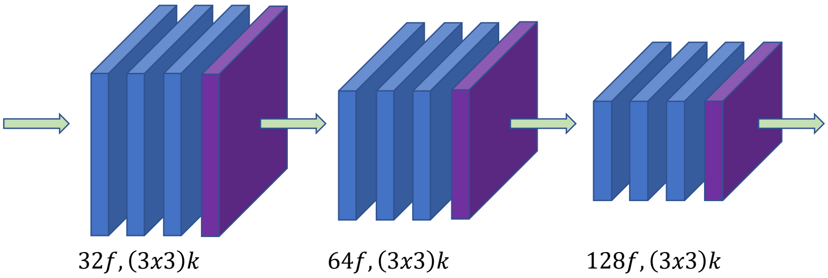

Figure 7.2: Basic overview of the encoder of the ML model that is used for predicting the ultimate strength of stiffened panels. The blue elements represent the convolutional layers. The pooling layers are displayed as purple elements. The first series of convolutional layers uses 32 filters. The second series uses 64 filters and the last series uses 128 filters. All convolutions use 3 × 3 kernels.

As can be seen from fig. 7.2, two or three consecutive convolutional layers are used before a single pooling layer. After each convolutional layer, the output is put through a Rectified Linear Unit (ReLU) activation function to introduce non-linearity. ReLU activation functions are used to prevent the vanishing gradient problem from occurring [22]. The vanishing gradient problem is where the gradient of the nodes in the first layers of the model becomes so small that the model is prevented from learning quickly or failing to learn at all. After the network is fully developed, other activation functions are tested, and it became clear that with other activation functions the model is prone to slow learning.

The network is built in three groups of convolutional layers, the first and second group contain two convolutional layers. The third group contains three layers. Between every group, that data size is reduced by 75% by using a max-pooling layer with a $2 \times 2$ kernel.

This architecture is based on the well known VGG-16 architecture [97]. During testing of the ML model developed in this research, larger kernel sizes $(7 \times 7)$ and $(9 \times 9)$ showed better learning performance and lower errors compared to smaller kernel sizes $(3 \times 3)$. There are two main benefits of using multiple layers with smaller kernel sizes over single convolutional layers with large kernel sizes. The first reason is the introduction of more non-linearities. After every single convolutional layer, a non-linear transfer function is applied to introduce non-linearities. These non-linearities make it possible for the network to learn highly non-linear problems more efficiently. The second reason is related to the number of model parameters in the model. As mentioned in the paper of Simonyan and Zisserman [97], three consecutive convolutional layers with a $3 \times 3$ kernel and $C$ filters will have $3(3^2C^2) = 27C^2$ weights. A single convolutional layer with a $7 \times 7$ filter and $C$ filters uses $7^2C^2 = 49C^2$ parameters. It can be concluded that multiple consecutive convolutional layers reduce the number of model parameters. three consecutive convolutional layers with $3 \times 3$ kernels will have the same receptive field as a single convolutional layer with a $7 \times 7$ kernel according to eq. (2.31), this means that the same result is obtained with fewer calculations when using multiple consecutive $3 \times 3$ kernels.

After each convolutional layer, and before the signal is put through the non-linear activation function, the convolutional layer's output is fed through a so-called batch normalization layer. During learning, the weights in the model get changed many times, which may cause shifting of the prediction of the distribution the inputs of a layer will have. The batch normalization prevents weights from making drastic changes by normalizing the output of the previous layer limiting this change in distributions. This is done by subtracting the mean of the previous batch and then dividing by the variance. Batch normalization is proven as an effective way to speed up the learning process and can help to prevent overfitting behavior [98]. Overfitting is when the networks start to learn how to exactly fit the data where it is trained on, causing bad predicting performance on other data that is not within the set of training. The developed CNN is developed by making use of Keras with Tensorflow backend. The batch normalization layer allows for setting a momentum parameter; a parameter that influences how much the previous batch is used to apply the batch normalization. Most models use almost all the effects of the previous batch. Which means the momentum is close to one. In this research, the momentum is set to 0.7 because a batch of models is randomly selected, and there is the possibility that a large part of the models fails in the same buckling mode. This will cause substantial updates in the model. Limiting the amount of momentum reduces the effect of these kinds of batches, producing a smoother loss curve during learning.

### 7.2.2. Ultimate Strength Prediction

After the data is passed through the three convolutional blocks described in fig. 7.2, the output of the last max-pooling layer is fed through a flattening layer. A flattening layer is nothing more than a reshape operation. The output is reshaped to an array. The output of the last max pooling layer is $3 \times 18 \times 128$. Flattening this layer will result in an array with 6912 points.

After flattening, the data is put through a series of fully connected layers. Fully connected layers, or dense layers, are the type of layers used in fig. 2.5. These layers do have a predefined number of neurons. In between the fully connected layers, all neurons are connected to the next layer's neurons. These connections are the reason why they are called fully connected or dense. In this research, three fully connected layers are used with every 64 nodes. The output of every layer is sent through a ReLU activation function. The activation function of the last layer is a linear unit. The reason for this is that a ReLu only allows positive values, while the model must also be able to predict negative values. The output of the linear unit is summed together in a single neuron of which the output is the predicted ultimate strength of the stiffened panel.

A schematic overview of the model is presented in section 7.2.2. This overview includes the encoder, the flattening layer, and the fully connected layers. The activation functions and the batch normalization layers are not presented in the figure.

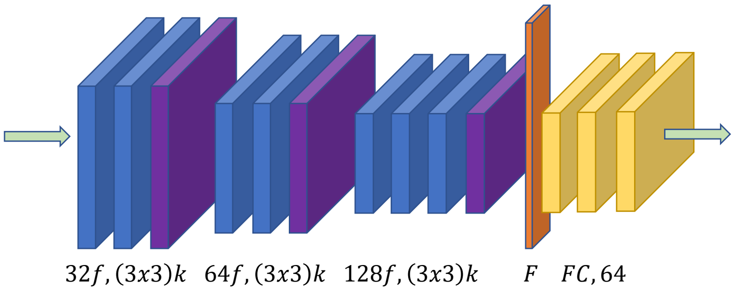

Figure 7.3: Overview of the entire ultimate strength prediction mode. The encoder consists of three convolutional blocks made of multiple convolutional layers with batch normalization and a max pooling layer. The output of the encoder is flattened ($F$) and send through three fully connected ($FC$) layers with 64 neurons to predict the ultimate strength

## 7.3. Optimization and Evaluation

The previous sections described the architecture of the network. The network requires an optimizer and a loss function. These will be explained within this section. As mentioned in section 2.2.2, multiple optimizers are available. The research of Choi et al. [99] shows that it is not straightforward to pick an optimizer. The optimizer's performance is highly dependent on the tuning of the individual parameters that can be changed in the optimizer. Their research showed a good overall performance of the Adaptive Moment Estimation (Adam). In this research, the performance of different optimizers is tested, and the Adamax optimizer, which is based on the Adam optimizer, shows the best performance. Adamax is like Adam, an optimizer that has an adaptive learning rate. With an adaptive learning rate, the optimizer itself regulates the learning rate. An initial learning rate is set to 0.0001. Both Adam and Adamax have two parameters ($\beta_1, \beta_2$), which determine how heavily the gradients in the previous batch are used to change the weights after the current batch. Both beta parameters are set high, which means that the previous gradients do not significantly influence the weight update. The high beta parameters are used because of the same principle described in section 7.2.1. With the dataset of stiffened panels, it is possible that a batch can be selected with a set of similar structural models, resulting in excessively large gradients during the batch. Therefore $\beta_1$ is set to 0.99 and $\beta_2$ is set to 0.999.

The optimizer needs a defined loss function. For regression analysis, often the Mean Squared Error (MSE) will be used as the loss function. This loss function is used because outliers create a more distinctive error compared to using the Mean Absolute Error (MAE). This way, wrong predictions get corrected more drastically. The MSE is calculated by eq. (7.2).

$$MSE = \frac{\sum_{i=1}^{n} (y_i - \hat{y}_i)^2}{n} \tag{7.2}$$

The entire dataset generated in chapter 5 consists of 9207 models. Some of the models failed to converge end resulted in a final set of 9194 models. A total of 80% (7355 models) of this dataset will be used for training the model. The other 20% will be used to validate the performance of the model during learning and for tuning the hyper-parameters of the ML model. This set contains 1839 models. This split is made such that the distribution in both sets remains close to the original set's distribution. The distributions of the individual parameters within the set can be seen in fig. A.3 in the appendix. Besides the training and validation data, a test set is created of random models within the distribution of the original data set. The test set contains 1782 models that the network has never seen during its training phase. The test set is only used to test the final performance of the model after it is fully trained. The distribution of the individual geometrical parameters is displayed in fig. A.4

When training the model, batches are used. The use of mbatches means that the full dataset is randomly sampled in smaller predefined batch sizes. After the batch is put through the network, the weights in the model will get changed. This way, multiple updates will be performed before passing through the entire dataset once. Every pass through the model by the entire dataset is called an epoch. With a large dataset, it slows down the learning process if the weights only get updated after putting all the available data through the network. With large input data in convolutional networks, significant computational power is required to load and process all the data at once. In this research, batches of 256 models are used. The network is trained for 20000 epochs. After training, the model weights are used from the epoch with the lowest error on the validation set.

## 7.4. Results

The previous sections of this chapter gave an overview of the network architecture, and the principles used to train the model. The model shows bad performance when predicting the ultimate strength or the ratio between the ultimate strength and the yield strength of the parent material ($\sigma_u/\sigma_y$). The model shows excellent performance when it is trained in predicting the total reaction force on the structure. This total reaction force can easily be transformed into the ultimate strength by dividing it with the cross-sectional area on which the total reaction force acts. Therefore it is decided that it is possible to use the total reaction force as the output of the model.

Initially, the model is trained for 5000 epochs. After 5000 epochs, it was observed that the model still showed improvements. Therefore, it is decided to train the model for 10000 epochs. After this moment, still, an improvement was observed. It is chosen to increase the number of epochs to 20000. Figure 7.4a shows the MSE of the model at every epoch. This figure shows a rapid decrease in error after a few epochs. A log-plot of the same results is displayed in fig. 7.4b to make the model's performance clearer. The x-axis, which contains the epochs, is still linearly scaled. It can be observed that the loss still shows a steady decreasing trend. The obtained results are already considered accurate enough, and it is decided that the model will not be trained longer. The improvement of increasing the number of epochs is not considered sufficient enough compared to the required computational time.

Table 7.1: Error created by the ultimate strength predicting ML model. The Mean Squared Error (MSE), Mean Absolute Error (MSE), and Mean Average Percentage Error (MAPE) are given. The train data consists of 7355 models which are used to train the model. The validation data consists of 1839 models and is used to tune the model hyper-parameters and validate the performance during learning. The test set contains 1782 models and is used to test the performance after training. Similar performance between all dataset can be observed.

| Error | MSE ($N^2$) | MAE (N) | MAPE (-) |
|---|---|---|---|
| Validation data | $0.938 \cdot 10^9$ | 13011 | 0.125% |
| Test data | $1.005 \cdot 10^9$ | 14079 | 0.139% |
| Train data | $0.655 \cdot 10^9$ | 12345 | 0.124% |

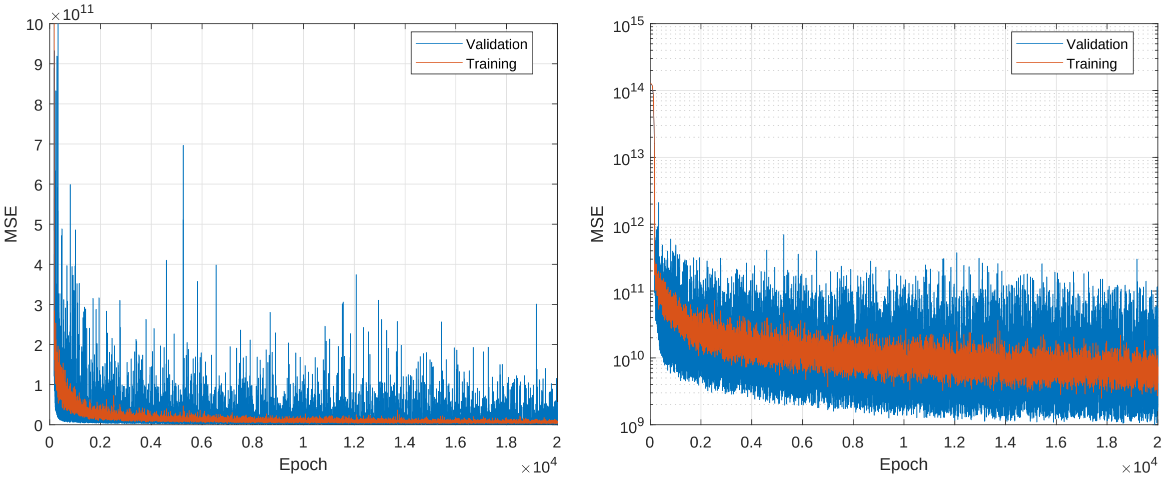

(a) MSE plot of the model developed to predict the ultimate strength of stiffened panels. Red shows the error on the training set. Blue shows the error on the validation set.

(b) MSE log plot of the model developed to predict the ultimate strength of stiffened panels. Red shows the error on the training set. Blue shows the error on the validation set.

Figure 7.4: The MSE of the model developed to predict the ultimate strength of stiffened panels. A clear decreasing trend can be observed. It can also be observed that there are a significant amount of spikes available in the model. The spikes are cause to the random batch selection. The training set consists of 7355 models. The validation set is contains 1839 models.

From fig. 7.4, it can be observed that the data oscillates heavily. It is difficult to observe the exact behavior if 20000 iterations are plotted in a small figure. Therefore fig. 7.5 shows a part of the loss plot in fig. 7.4a. This figure shows the results for epoch 10000 to 10100. From the figure, it can be seen that most of the epochs, the obtained loss oscillates, as expected, around the loss on the training data. Some of the epochs show a significantly larger error. During the testing of the network, it is observed that the number of models in the batch size influences the number of weight updates that cause an excessively high loss compared to the training loss. An increase of models in a single batch shows a decrease in the number of spikes. Similar behavior was observed by changing the amount that the optimizers use the gradients from the last step in updating the weights. Based on these observations, it is assumed that those spikes would be caused by the selection of 'bad' batches. The batches are randomly drawn from the whole training set every single epoch. The random selection of batches makes it possible for a batch only to contain similar models, which might create a relatively high error. The spikes in the loss are reduced as much as possible without influencing the network's learning performance. The obtained figures show that even with the spikes in the loss function, the networks show a steady decrease in loss over the number of epochs.

The network is trained and during training the performance of the network is tested by the validation set. The validation set is also used to optimize the model. After training the model, the performance of the model is tested on a set the network has never seen. This set is called the test set. If the network shows excellent performance on the training and validation data, it is still possible to obtain bad performance on the test data, which is called overfitting. Overfitting is when the network learns to fit the training and validation data to accurately, showing bad performance on other data. The individual losses on the training, validation, and test data are displayed in table 7.1. Next to the MSE, the Mean Absolute Error

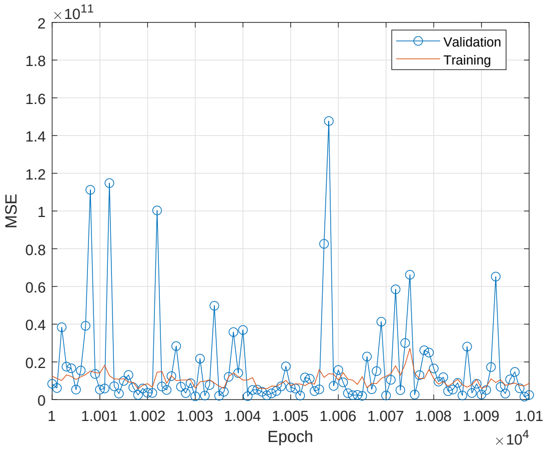

Figure 7.5: Zoomed in plot of the loss function of the ultimate strength prediction model for epoch 10000 to 10100. It can be observed that most results from the validation set are close to the curve of the trainings loss although some models have a significant larger error compared to the error on the training set.

(MEA) and the Mean Absolute Percentage Error (MAPE) are displayed. These are displayed since the output is a numerical value, and the MSE has no physical meaning since it has $N^2$ as unit. It can be concluded that similar results are obtained on all three datasets.

## 7.5. Scalability

As became clear from the literature review in chapter 3, good performance of predicting the ultimate strength with the use of ML is not completely new. In the literature, no clear information is available on the performance of the ML model on data that does not fall within the scope of data used for training the model. For that reason, a scalability study is performed with the trained model.

In the scalability study, every individual parameter of the stiffened panel that can change between the models is tested. These parameters are: The plate thickness ($t_p$), the height of the web ($h_w$), the thickness of the web ($t_w$), the width of the flange ($b_f$) and the thickness of the flange ($t_f$). As can became clear from section 5.6.3, some of the models are already at the limits by what classification societies allow or on the limitations of the production. Therefore, the choice has been made to only scale the individual parameters positively, so increasing their size. From the original training set, 288 models are randomly selected, such that they are spread over the entire distribution of the training set. The distributions of the 288 models of the scalability test set are displayed in fig. A.5. The model contains five variable geometrical parameters, which are increased in steps of 5%. The individual variables are increased to a maximum of 25%. This will result in a dataset of 7200 models. From this dataset, the individual losses are obtained for every single parameter and per step of 5% increase. These losses are displayed in fig. 7.6. The performance of the ML model is not tested on data in which all variables are scaled. This is not done because then it is not possible to see te effect of individual variables and it is already expected that by changing the individual variables the average error will increase significantly.

Figure 7.6 shows that the model can still accurately predict the outcome of the models, which are increased by 5% and 10%. The loss on the models increased with 5% is lower than the loss obtained on the test and validation set, displayed by the dashed lines in the graph. The reason for this is that the average loss on the 288 selected models is lower than the loss on the full test, training, and validation set which contain significantly more models. The loss on the full validation and test data is plotted since it is more representative than the scalability errors. If a more extensive dataset would have been picked for the scalability test, it is expected that the loss of the 5% and 10% increase is higher than the mean loss of the test and validation set. Beyond the 10% increase of the parameters, a definite increase in a mean loss of all individual parameters is observed. Increasing the flange parameters causes less increase in loss compared to the other parameters. Therefore, the flange will probably have a less significant impact on the ultimate strength of stiffened panels compared to the impact of the other three

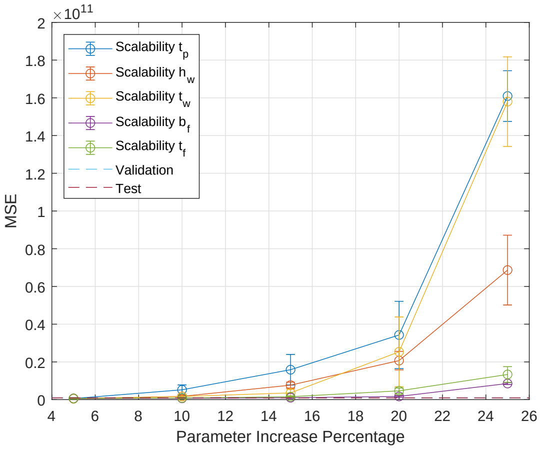

Figure 7.6: MSE plot of the model developed to predict the ultimate strength of the stiffened panels. The errorbars represent the SE. It can clearly be observed that $t_p$, $t_w$ and $h_w$ are the most sensitive to an increase in parameters.

parameters. The plot also shows error bars which show the Standard Error which can be determined by dividing the standard deviations by the square root of the number of data examples.

Table 7.2 shows the exact losses of the individual parameters with the percentage of parameter increase. Figure B.4c shows a box plot of all the individual increments and individual parameters. The box plot make the distribution of the predicted results more clear. The figure also shows that with increasing the individual parameters the number of predictions that are considered outliers increases. For a 10% increase in the variables, more models are considered outliers and the median of the error shows a small increase. Therefore, it is concluded that predictions 10% outside the range of training do not provide reliable results.

Table 7.2: Error created by the ultimate strength predicting ML model. The results are the errors obtained by the scalability testing. The individual parameters are increased in steps of 5%. It can be observed that some parameters are less susceptible for an increase, although every parameters shows an increase in error.

| Percentage | $t_p$ MSE ($N^2$) | $h_w$ MSE ($N^2$) | $t_w$ MSE ($N^2$) | $b_f$ MSE ($N^2$) | $t_f$ MSE ($N^2$) |
|---|---|---|---|---|---|
| 5% | $0.589 \cdot 10^9$ | $0.571 \cdot 10^9$ | $0.480 \cdot 10^9$ | $0.618 \cdot 10^9$ | $0.644 \cdot 10^9$ |
| 10% | $0.522 \cdot 10^9$ | $1.724 \cdot 10^9$ | $1.666 \cdot 10^9$ | $6.959 \cdot 10^9$ | $0.851 \cdot 10^9$ |
| 15% | $1.587 \cdot 10^9$ | $7.679 \cdot 10^9$ | $3.563 \cdot 10^9$ | $1.024 \cdot 10^9$ | $1.544 \cdot 10^9$ |
| 20% | $3.428 \cdot 10^{10}$ | $2.070 \cdot 10^{10}$ | $2.543 \cdot 10^{10}$ | $1.694 \cdot 10^9$ | $4.662 \cdot 10^9$ |
| 25% | $1.610 \cdot 10^{11}$ | $6.868 \cdot 10^{10}$ | $1.580 \cdot 10^{11}$ | $8.548 \cdot 10^9$ | $1.334 \cdot 10^{10}$ |

## 7.6. Available Training Data

The literature review in chapter 3 also made clear that the size of the training data in structural engineering is often limited. Therefore, the effect of the number of training examples is tested. The same network has been trained with less training data. The minimal amount of training data tested is 10% of the original amount of training data. The training set is obtained by randomly sampling the original training set. This procedure can cause inaccurate results due to the random sampling of the full data set. For every size of the training set, the model is trained eight times. This means that model is trained 72 times. The obtained results are displayed in fig. 7.7.

Figure 7.7a shows the loss on the full validation set. It can be observed less training data influences the obtained loss negatively. Also, it can be observed that the spread in the obtained error becomes larger for smaller amounts of training data. The same behavior can be seen in fig. 7.7b, which is the loss plot on the full test data. From both figures, it can be concluded that the obtained loss increases with less trainings data. However, if the obtained losses are compared to the results of the scalability test in table 7.2, the obtained losses do not increase as significantly. With even a small

Table 7.3: The median of the error created by the ultimate strength predicting ML model. The results are the errors obtained by decreasing the size of the dataset used for training. A fixed percentage of models is selected from the original dataset. It can be observed that less training data increases the predicted error on all datasets. The curve flatten near the 50% use of data.

| Percentage | Validation MSE (N$^2$) | Test MSE (N$^2$) | Training MSE (N$^2$) |
|---|---|---|---|
| 10% | $1.077\cdot10^{10}$ | $1.033\cdot10^{10}$ | $1.039\cdot10^{10}$ |
| 20% | $7.607\cdot10^{9}$ | $7.624\cdot10^{9}$ | $7.637\cdot10^{9}$ |
| 30% | $6.110\cdot10^{9}$ | $6.345\cdot10^{9}$ | $6.112\cdot10^{9}$ |
| 40% | $4.783\cdot10^{9}$ | $5.333\cdot10^{9}$ | $5.119\cdot10^{9}$ |
| 50% | $4.515\cdot10^{9}$ | $5.164\cdot10^{9}$ | $4.881\cdot10^{9}$ |
| 60% | $4.039\cdot10^{9}$ | $4.674\cdot10^{9}$ | $4.575\cdot10^{9}$ |
| 70% | $4.26\cdot10^{9}$ | $4.950\cdot10^{9}$ | $4.629\cdot10^{9}$ |
| 80% | $3.268\cdot10^{9}$ | $3.826\cdot10^{9}$ | $3.561\cdot10^{9}$ |
| 90% | $3.156\cdot10^{9}$ | $3.827\cdot10^{9}$ | $3.380\cdot10^{9}$ |

amount of training data, a good accuracy is obtained on models within the range of training data. This does not imply that similar scalability behavior would be observed when the model is trained with less training data. Although the loss is not that high for small sets of training data, it is important to note that the spread is larger, which means that the network's performance becomes more dependent on the selected data. This means that for smaller datasets, the quality of the training data becomes more important compared to the larger datasets.

The exact values of the median of obtained losses are displayed in table 7.3. This table also gives the losses obtained on the full training set (7355 models).

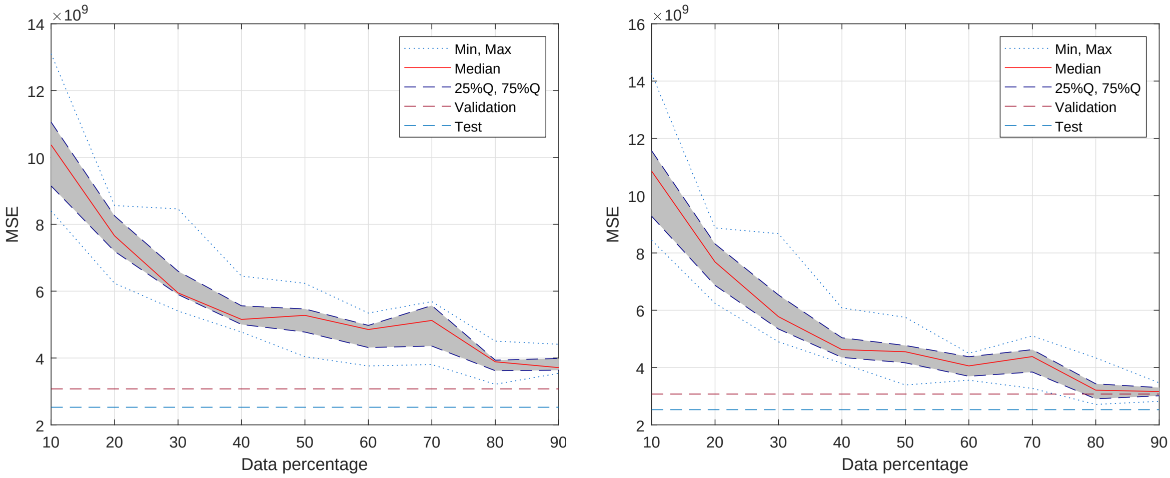

(a) MSE plot of the model developed to predict the ultimate strength of stiffened panels. The MSE is obtained on the full validation set. An increase can be observed with less training examples. The network is trained 72 times.

(b) MSE plot of the model developed to predict the ultimate strength of stiffened panels. The MSE is obtained on the full test set. An increase can be observed with less training examples. The network is trained 72 times.

Figure 7.7: MSE plot of the model developed to predict the ultimate strength of stiffened panels. The network is trained a total of 72 times. The figures show the minimum and maximum obtained errors. Also the median and the 25% and the 75% quartile are displayed

The table and the graphs make clear that above 50% the obtained loss starts to flatten. The spread becomes less with the addition of more models. It can be concluded that for this dataset, around 4000 training examples would make it possible to obtain a well trained ML model. A dataset of 4000 models is more than most researches mentioned in chapter 3 used.

## 7.7. Generalizability

In the previous sections, the developed ML model's performance is tested on the scalability and its performance when varying the available amount of training data. The developed ML model's performance is also tested on data that show some similarity with the original data but are geometrically different, which is called testing the generalizability. In the previous tests, only flat stiffened panels are used, but in shipbuilding curved plates are also widely used. Stiffened panels used in ships can be curved in multiple directions. In this research, only transverse curved stiffened panels are tested with a fixed radius of curvature over the entire stiffened panel. Transverse curved plates occur, for example, in the bilge of the ship.

To test the ML model's generalizability, the same set of models is used as the set used for the scalability. This set contains 288 models that lay within the training parameter range of the ML model. The entire set is curved by increasing the mid-panel height in steps of 0.2 meter until a height of 1 meter is reached. This implies that in total five steps are used, creating a dataset containing 1440 models. Since a fixed radius of curvature is used, the curve can be considered an arc of a circle. This means that the radius of curvature ($R$) can be determined from the height ($H$) mid-plate and the width of the stiffened panel ($B$) by eq. (7.3). The stiffened panels are curved such that the stiffeners point towards the center of the curvature, as can be seen in fig. 7.8. It is important to note that the stiffened panel does not have the same width as all the flat stiffened panels. The stiffened panel van be seen as an arc of a circle. The arc-length is different depending on the height of $H$. The chord length is kept at 4 meter, just like all the flat stiffened panels. The reason for this is that in this way the curvature will only be new for the ML. When the plating length is kept at 4 meters, the y-value range is changed, introducing more new information for the ML model, probably influencing the performance of the predictions. It is expected that with changing the curvature the obtained error will already show a significant increase.

$$R = \frac{H}{2} + \frac{B^2}{8H} \tag{7.3}$$

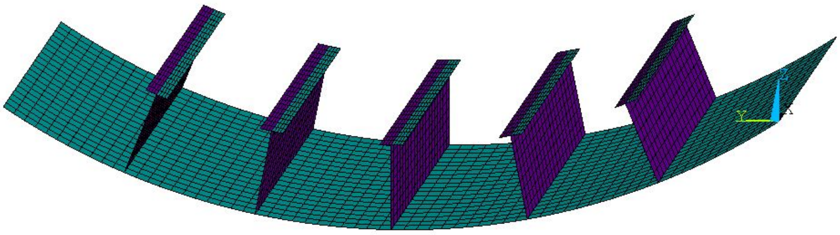

Figure 7.8: Mesh of a transverse curved stiffened panel with a mid panel height of 0.6 meter. A fixed radius of curvature is present over the stiffened panel. The width over the y-axis is kept at 4 meter, which is similar to the flat stiffened panels.

The trained ML model learned no information on the curvature of stiffened panels since this information is not present in the used training data. The only information the ML model learned about the z-direction (height) of the stiffened panel is related to the stiffeners. Therefore, it is already expected that the ML model will generate a significant error in the predicted ultimate strength. The check whether this hypothesis is correct, the performance is determined for every individual curvature, and the results are displayed in table 7.4.

Table 7.4: Mean error create by the ultimate strength predicting ML model. The generalizability data consists of 1440 models transverse curved stiffened panels. The results are obtained by increasing the height of mid-plate in steps of 0.2 meter. It is observed that the error is large and keeps increasing by increasing the amount of curvature.

| $H$ (M) | MSE ($N^2$) | MAE (N) | MAPE (-) |
|---|---|---|---|
| 0.2 | $4.651 \cdot 10^{13}$ | $6.330 \cdot 10^{6}$ | 77.656% |
| 0.4 | $2.444 \cdot 10^{14}$ | $1.522 \cdot 10^{7}$ | 184.076% |
| 0.6 | $5.462 \cdot 10^{14}$ | $2.310 \cdot 10^{7}$ | 255.597% |
| 0.8 | $9.612 \cdot 10^{14}$ | $3.079 \cdot 10^{7}$ | 316.711% |
| 1.0 | $1.605 \cdot 10^{15}$ | $3.986 \cdot 10^{7}$ | 388.678% |

From the obtained losses, it can be concluded that the hypothesis on the generalizability is correct. even with a small curvature, a significant error is obtained. This error is large enough to conclude that the results from curved stiffened panels are not suitable for usage. Besides looking at the mean losses, the individual predictions are also inspected and displayed in fig. 7.9. Figure 7.9a shows a box plot of MSE on the curved stiffened panels. The mean error on the test and validation set is also displayed, but these are substantially lower than those obtained on the generalizability models. The box plot shows a definite increase in the obtained error when increasing the stiffened panel's curvature. Also, the spread increases, as can be observed by the increase of the box size and the whiskers. Figure 7.9b shows the predicted values against the real values obtained with FEA. The individual predictions should lay on the red line if they are correctly predicted. This figure clarifies that the ML overestimates the ultimate strength of the stiffened panel significantly since the predictions are located right of the red line. It is interesting to see that results shift to the right quite linearly without too much distortion in the distribution of the results. The reason for this behavior is not apparent.

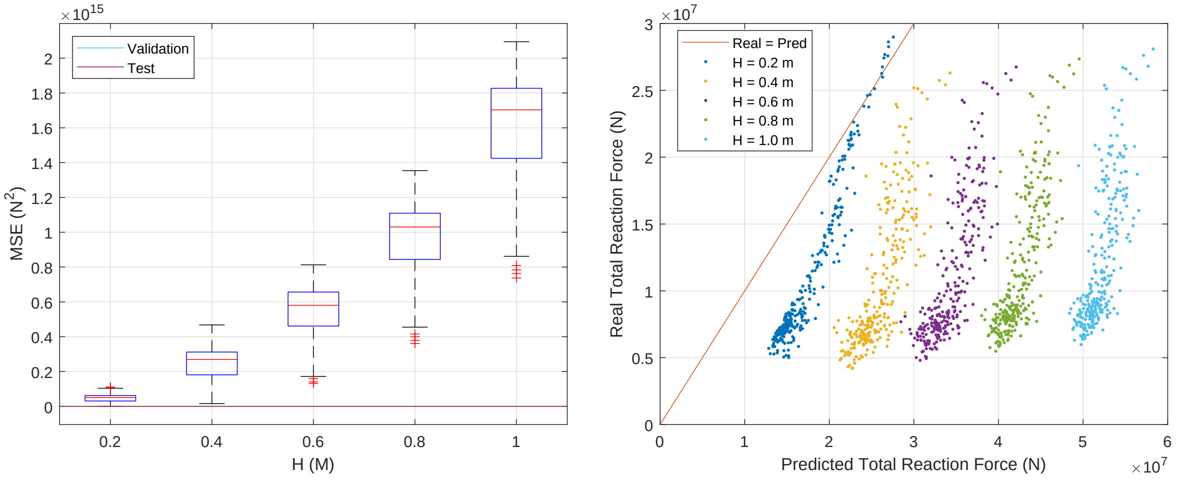

(a) MSE box plot of the model developed to predict the ultimate strength of stiffened panels. The results are obtained on the curved stiffened panels. A clear increase in error can be observed when increasing the amount of curvature of the panel.

(b) Plot of the predicted results compared to the real solution. A clear overestimation of the ML can be seen by increasing the curvature of the stiffened panel since the results are all on the right side of the red line.

Figure 7.9: Graphical representation on the generalizability by the ultimate strength predicting ML model. Figure (a) shows a box plot of the individual prediction per value of $H$. Figure (b) shows the prediction of the individual models compared to the real value.

Overall it can be concluded that the developed ML model does not perform well on generalizability. The obtained error for slightly curved plates is already significant and unusable. This was already expected since the training data did not contain any information about the stiffened panel's curvature.

## 7.8. Conclusion

The developed model shows that it can learn to predict the ultimate strength of stiffened panels. The loss on the predicted ultimate strength values is well below 1%, which is considered an excellent prediction.

When testing data that is not within the range of training, it could be observed that the loss rapidly increases. If the results are within a 5% margin of the dataset used for training, decent predictions are still obtained. Beyond this percentage, the error becomes significantly large, and the prediction is likely to become inaccurate.

The model is also repeatedly trained with different amounts of training data to see how much data is at least required to obtain good predictions. With a set of 4000 models in the training set, good results are obtained from learning. Also, learning is considered stable with this amount of data available. Stable learning is considered when the model converges to the same result independent of the dataset selected from the full-sized dataset used for training. Below the 4000 models, this spread increases significantly, and the ML-model performance is going to depend highly on the spread of the input data. Also, the average obtained loss rapidly increases below the use of 4000 models in the training set. Beyond the 4000 model mark, a substantial amount of new data is required to reduce the error significantly. This 4000 model mark is suitable when the dataset contains five geometric variables. If the dataset has more than five variable parameters, it would probably be required to have more data in the training set.

At last, the ML model's performance is tested on a variety of curved stiffened panels to see how well the developed model's generalizability is. Even with a small curvature, the ML model cannot accurately predict the ultimate strength of the stiffened panel. However, this is expected as no curvature information is present in the training set. An increase in curvature keeps increasing the obtained error. Therefore, it can be concluded that the generalizability of the developed model is inadequate.

# 8

# Prediction of Localized Stress Distribution

In the previous chapter, chapter 7, a convolutional neural network (CNN) has been developed to predict the ultimate strength of stiffened panels loaded under longitudinal uni-axial compression and lateral pressure. In this chapter, a new model is developed, which is partially the same as the model used in the previous chapter. This model will be developed to predict the stress distribution over the stiffened panel. The same model is trained twice, one time it is used to predict the individual stress components, the other time it is used to predict the von Mises stress distribution.

The Machine Learning (ML) model developed to predict the stress distribution is described in section 8.1. The encoder will not be discussed since this is described in chapter 7. In the next section, section 8.2, the used optimizer, and the loss functions will be discussed. Section 8.3 will provide the results obtained from the trained model. The developed model will also be tested on how well it performs on results outside the training range, called scalability. This is described in section 8.4. The ML model is also tested on generalizability by performing tests with curved stiffened panel in section 8.5. The last section will provide the conclusions in section 8.6.

## 8.1. Model Architecture

The developed ML model is partially the same as the model used in chapter 7. The input of the model is the mesh of the stiffened panels. This input is again pulled through the encoder described in section 7.2.1 to compress the input data to a smaller array that is a representation of the original input. In the previously developed model, this compressed input is sent to fully connected layers. In this developed model, that data is not put through the fully connected layers. Instead, it is fed to ResNet bottleneck modules with identity mapping developed by He et al. [100]. The idea of using ResNet modules is based on the research of Nie et al. [77]. The description of the ResNet bottleneck modules is given in section 8.1.1. After the ResNet modules, the data is sent through a similar structure as the encoder but then inverted. The compressed representation will be transformed back to a mesh with the stresses at each node. This is called decoding, described in section 8.1.2.

### 8.1.1. ResNet Bottleneck

In this research, ResNet bottleneck modules are used. The use of ResNet modules is based on research by Nie et al. [77]. They also used a CNN to predict the stress distribution over small 2-D mesh. With the use of ResNet modules combined with Squeeze and Excitation (SE) modules [101], they obtained good results. Therefore, it is decided to use a similar network architecture. When using the same modules as in the research of Nie et al. [77], the loss function showed significant noise, and the modules caused unstable learning. After testing several architectures and different modules, it was concluded that the SE modules would not be used within this research. Besides the ResNet modules, it is also tried to directly connect the encoder to the decoder, described in section 8.1.2. The model showed fast learning, but the model quickly stopped improving. A series of fully connected layers have been tested between the encoder and the decoder module. After the fully connected layers, the output is reshaped so the decoder could use it. This architecture is also capable of learning, but was outperformed by the ResNet modules. After testing many different architectures, the best results were obtained with ResNet bottleneck modules.

The bottleneck modules consist of three consecutive convolutional layers, as is shown in fig. 8.1. The first convolutional layer is a convolutional layer with a $1 \times 1$ kernel and a fourth of the filters of the layer before the ResNet module. The second layer uses a $3 \times 3$ kernel and the same number of filters as the first layer. The last layer is again a $1 \times 1$ convolution, but to restore the original input size of the ResNet module, it uses the same number of filters as the input of the module. The output of the encoder contains 128 filters. So the bottleneck module will have 32 filters in the first and second layers and again 128 filters in the last convolutional layer. After every convolutional layer, batch normalization is used, followed by a ReLU activation function, as described in section 7.2.1. After the last convolutional layer, no activation function is used. The output of this layer is added to the ResNet module's input, also called identity mapping. After the summation of both signals, a final ReLU activation function is applied. In the paper of He et al. [100], the researchers mention that the primary goal of the bottleneck modules is to reduce network dimensionality. Bottleneck modules roughly contain the same amount of trainable parameters as a module with two consecutive convolutional layers with the same amount of filters and $3 \times 3$ kernels. In this research, both modules have been tested. The bottleneck version with three convolutional layers showed better results compared to its two layer counterpart. The bottleneck module showed the best performance of all the different tried modules in this research. Therefore bottleneck modules will be used in the developed model. In total, five consecutive bottleneck modules are used in between the encoder and the decoder.

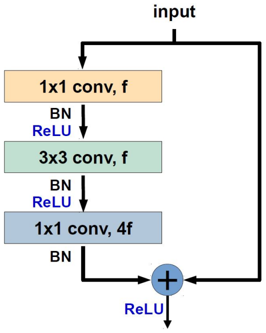

Figure 8.1: ResNet bottleneck module. The input of the bottleneck contains $4f$ filters. The first layer reduces dimensionality with a convolutional layer with a $1 \times 1$ kernel and $f$ filters. Then a convolutional layer with a $3 \times 3$ kernel is applied with $f$ filters. The last convolutional layer restores the original dimensions by using a $1 \times 1$ kernels with $4f$ filters. The output of the last convolutional layer is added to the input of the ResNet modules, also called identity mapping. Image taken from [102].

### 8.1.2. Stress Distribution Decoder

After applying the ResNet bottleneck modules, the data still has the same size as after the encoder. This data will then be used to feed into a decoder, which is the encoder's inverse process. In the previously developed model in chapter 7, the model had to output a single value, the ultimate strength of the stiffened panel. The newly developed model needs to predict an output with the same size as the input. Therefore, the decoder has to output the same sized mesh with one or six channels of data depending on the fact if only the von Mises stress is predicted or if the individual stress components are predicted. Hence the compressed data has to be transformed back to its original size. In the encoder, a combination of convolutional layers and pooling layers is used to compress the data. In the decoder, transposed convolutional layers will be used in combination with the upsampling layers.

Transposed convolutional layers apply the same principles as the convolutional layers used in the encoder. In the convolutional layers, the kernel is used to map a part of the original data with the kernel's size to a single point of data. In the transposed convolution, this single point of data is mapped back to a larger set of data by multiplying the weights in the kernel with the individual point of data. By applying this principle, the compressed dataset can be decompressed.

In the encoder, max-pooling layers are used to downsample the data with 75%, as described in section 2.2.1. In the decoder, upsampling layers are used to upscale the size of the data by a factor of four or more depending on the size of the layer. This is a simple, efficient linear process. With a $2 \times 2$ layer, every single point is turned into 4 points in a $2 \times 2$ shape with the same value as the original point. An alternative to this could be the use of transposed convolutional layers with a stride of 2. By using transposed convolutional layers, the network has more weights to learn to perform this operation, which allows predicting of the outcome better. The use of transposed convolutional layers is tested and did not show any improvement in the obtained losses compared to the upsampling layers' linear process. The use of convolutional transposed layers is computationally more extensive and is therefore not used.

The architecture of the decoder is the same as the architecture from the encoder. The convolutional layers are transformed into transposed convolutional layers with the same amount of filters. The max pooling layers are now upsampling layers. In the decoder, no batch normalization is used. The batch normalization prevents te model from learning. The reason for this is probably that the network needs to predict values in the range of 1e+6, while the batch normalization normalizes the signal between -1 and 1.

## 8.2. Optimization and Evaluation

This network uses the same principles as in section 7.3. In the end, Adamax showed the best performance of all the tested optimizers. In this network, batches are used with a size of 256 models. The loss function used by the optimizer is again the Mean Squared Error (MSE). The network is trained for 5000 epochs. After 5000 epochs, the training loss still shows a notable decreasing trend, but there is little improvement in the validation set's loss. Therefore, it is decided not to extend the number of epochs. The training of this model significantly takes longer than the training of the ultimate strength predicting model. In this network, there are 25% more trainable weights than in the network described in the previous chapter. Also, the size of the data is much larger. The size is two times larger when predicting the von Mises stresses and seven times larger when predicting the individual stress components. After training for all the epochs, the best performing epoch on the validation set is used to determine the weights in the trained model.

## 8.3. Results

The previous sections of this chapter and the explanation of the encoder in section 7.2.1 gave an overview of the network architecture, and the principles used to train the model. The network is trained for two different types of outputs. First, the model is used to predict the von Mises stress described by eq. (8.1). The model is trained for 5000 epochs. The obtained losses are displayed in table 8.1. The corresponding loss over all the epochs is displayed in fig. 8.2

$$\sigma_{\mathrm{VM}} = \sqrt{\frac{1}{2}\left[\left(\sigma_x - \sigma_y\right)^2 + \left(\sigma_y - \sigma_z\right)^2 + \left(\sigma_z - \sigma_x\right)^2\right] + 3\left(\tau_{xy}^2 + \tau_{yz}^2 + \tau_{zx}^2\right)} \tag{8.1}$$

In fig. 8.2, it can be seen that the error on the training set shows a notable stable decreasing trend. It is observed that the loss on the validation set also shows a steady decrease, but the loss stays significantly larger than the loss on the training set. This behavior also becomes clear from the displayed results in table 8.1. These obtained losses are not as expected. If the loss of the training and validation set starts to deviate, the model is overfitting the data. Overfitting often causes the error on the validation data to increase after more epochs. In this graph, the loss of the validation set still decreases. Therefore it is assumed that overfitting is not the cause for this deviation in the loss graph. The predictions are all converted to VTK-files so they can be graphically inspected. It quickly became clear that the ML model sometimes predicted the result reasonably accurate, but flipped along the longitudinal edge as displayed in fig. 8.4. The buckling of flat plates is an unstable analysis. The plate might buckle up or down, but the response is the same. After inspecting the predicted results more in detail, it became clear that the ML model partially learned when the plate should buckle up or down according to what the results are from the numerical analysis. In most of the models, the ML model was able to predict the correct direction of buckling. This observation is interesting since this mechanism is described by unstable behavior and there is no apparent reason why a plate should buckle up or down.

After this conclusion, the individual loss values of all the structural models are inspected. Also, the loss of the individual points in structural models with a significant high error are thoroughly investigated. It became clear what the reason is for the difference in the average loss obtained between the training data and the data from the test and validation loss, as could be observed from table 8.1. It is observed that most of the models have a loss of less than 1e+13, which does not follow the values given in the table. The average loss is affected by some of the models which are predicted to buckle in the wrong direction. It is concluded that the percentage of wrong predicted models is significantly

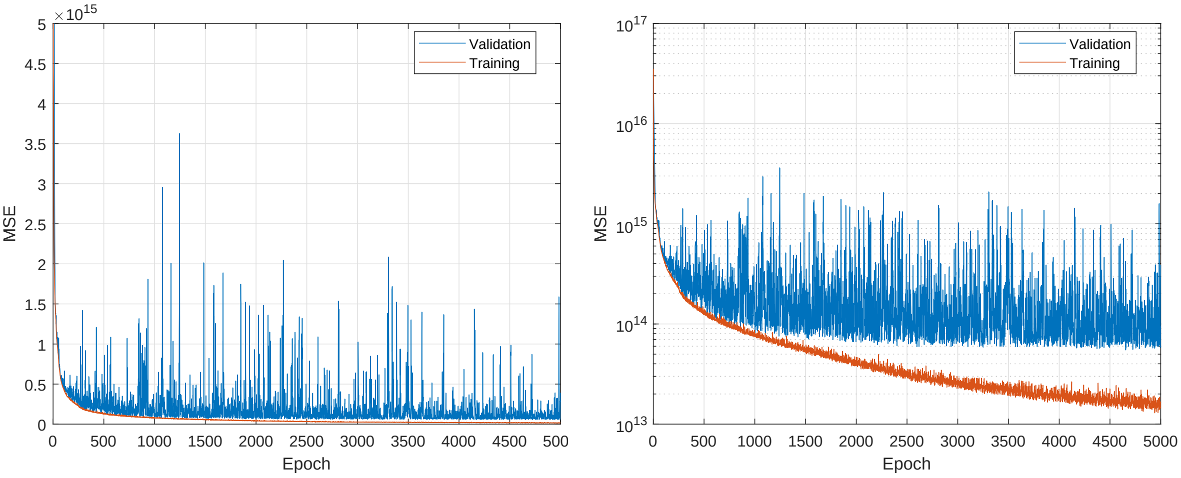

(a) MSE plot of the model developed to predict the von Mises stress distribution at the moment of failure. Red shows the error on the training set. Blue shows the error on the validation set.

(b) MSE log plot of the model developed to predict the von Mises stress distribution at the moment of failure. Red shows the error on the training set. Blue shows the error on the validation set.

Figure 8.2: The MSE of the model developed to predict the von Mises stress distribution. A clear decreasing trend can be observed in the loss function, while the validation set does not improve significantly. It is also be observed that there are a significant amount of spikes available in the model. The training set consists of 7355 models. The validation set contains 1839 models.

larger in the test and validation data compared to the training data. In the training set, only 0.14% of the results had a loss higher than 1e+15, while in the test and validation set, those percentages were respectively 1.29% and 1.80%. This makes clear why there is a difference between the loss obtained by the training data and the loss obtained by the test and validation set.

It was also observed that some of the models had a high loss while the actual overall prediction looks accurate. The problem that occurs in those models is that a few nodes in a single structural model were mispredicted. Sometimes positive stress was predicted, while strong negative stress should be predicted, creating a large difference between the two values. This prediction resulted in excessively large loss predictions, while the actual model was predicting quite accurately for the majority of the structural model. It was also interesting to observe that often the ML model failed to predict only a single node while the surrounding nodes were predicted accurately. There is no clear reason for these results.

Table 8.1: Error created by the von Mises stress predicting ML model. The trained data consists of 7355 models which are used to train the model. The validation data consists of 1839 models and is used to tune the model hyper-parameters and validate the performance during learning. The test set contains 1782 models and is used to test the performance after training. It can be observed that the MSE obtained on the training set is twice as low as the error obtained on the test and validation data set.

| Error | MSE (Pa$^2$) | MAE (Pa) | MAPE (-) |
|---|---|---|---|
| Validation data | $5.496 \cdot 10^{13}$ | $2.981 \cdot 10^{6}$ | 1.699% |
| Test data | $4.462 \cdot 10^{13}$ | $2.823 \cdot 10^{6}$ | 1.584% |
| Train data | $2.018 \cdot 10^{13}$ | $2.414 \cdot 10^{6}$ | 1.326% |

Figure 8.2b also shows spikes in the predicted losses. Similar spikes were observed in the results obtained in chapter 7. Figure 8.3a shows the zoomed-in loss data for epoch 2500 till 2600. Again, most of the points follow the same curve as the points in the training data. This time, the validation loss is higher than the training loss. It is also tested if the number of spikes is influenced by both the batch size and the amount last batch's gradient is taken into account by the optimizer. Similar results are obtained as for the model developed in chapter 7. Therefore, it can be concluded that these spikes are due to the random selection of the batches.

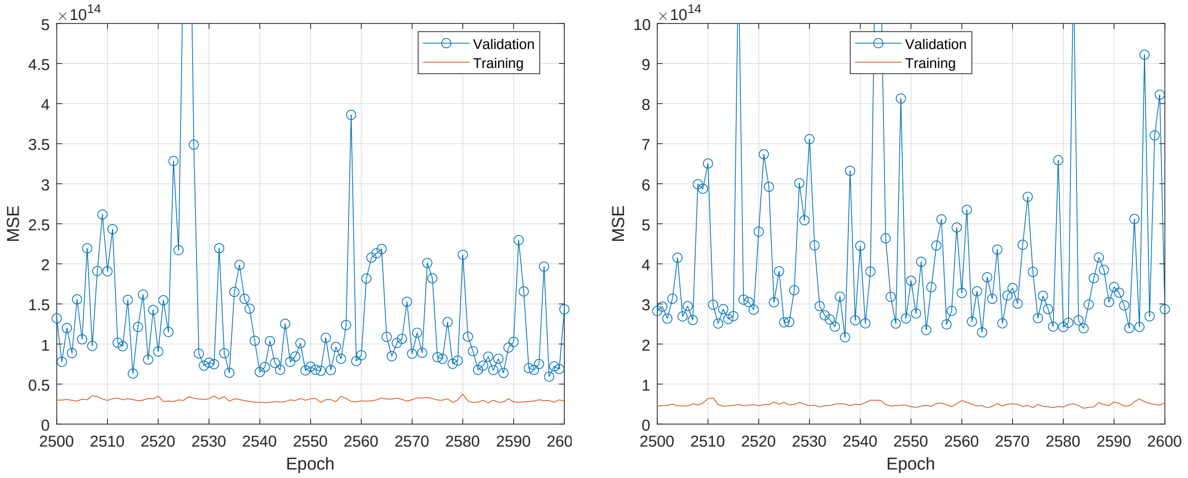

(a) Zoomed in plot of the loss function of the von Mises stress prediction model from epoch 10000 to 10100. It can be observed that most results from the validation set are close to the curve of the trainings loss although some models have a significant larger error compared to the error on the training set.

(b) Zoomed in plot of the loss function of the individual stress prediction model from epoch 10000 to 10100. It can be observed that most results from the validation set are close to the curve of the trainings loss although some models have a significant larger error compared to the error on the training set.

Figure 8.3: Predicted and real von Mises stress distribution over the stiffened panel. This model has an excessively large error according to the loss function. It can clearly be observed that the prediction is actually similar, but mirror along the longitudinal edge.

(a) Predicted von Mises stress distribution over the stiffened panel. This model has an excessively large error according to the loss function.

(b) Real von Mises stress distribution over the stiffened panel determined by the use of Finite Element Analysis (FEA) in Ansys.

Figure 8.4: Predicted and real von Mises stress distribution over the stiffened panel. This model has an excessively large error according to the loss function. It can clearly be observed that the prediction is actually similar, but mirrored along the longitudinal edge. The images shows the flat representation of the 3-D stiffened panel. The left section of the plate represents the plating in between stiffeners. The middle section of the image contains the webs of the stiffeners. The right side of the image contains the flanges of the stiffened panel.

The same ML model has been trained to predict the individual stress components of the stiffened panel. The used output is 6-D data containing all the individual stress components: the stress in x-direction ($\sigma_x$), the stress in y-direction ($\sigma_y$), the stress in z-direction ($\sigma_z$), the shear in xy-direction ($\tau_{xy}$), the shear in yz-direction ($\tau_{yz}$), and the shear in zx-direction ($\tau_{zx}$). The idea behind training the network on 6-D data is that it would be interesting if the ML-model would be capable of learning the interaction between the individual stress components to more accurately predict the stresses. The loss curves are displayed in fig. 8.5. Similar behavior is observed as in the results from fig. 8.2a. A zoomed in plot is displayed in fig. 8.3b for epoch 10000 to 10100. More spikes are observed in the loss curve compared to the results in fig. 8.3a, but the main trend can still be observed. When predicting the individual stress components, some models are again predicted to buckle in the wrong direction. To verify the reason for the difference between the loss on the training data and the loss on the test data, it is investigated how many of the models were predicted inversely related to the size of the whole data set. 2.7% of the test set has a loss higher than 1e+15. A similar 2.77% was obtained for the validation set. The number of models that had a loss higher than 1e+15 in the training set was only 0.34%. It can again be concluded that this is the reason for the large difference between the training and the two other data sets.

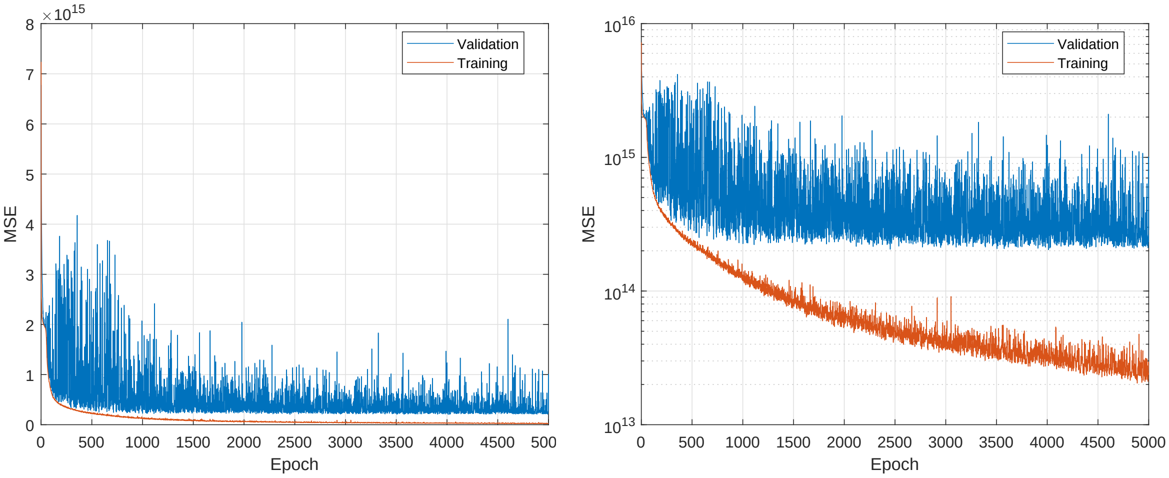

(a) MSE plot of the model developed to predict the individual stress distributions at the moment of failure. Red shows the error on the training set. Blue shows the error on the validation set.

(b) MSE log plot of the model developed to predict the individual stress distributions at the moment of failure. Red shows the error on the training set. Blue shows the error on the validation set.

Figure 8.5: The MSE of the model developed to predict the individual stress distributions. A clear decreasing trend can be observed for the training and test data. The loss on the trainings data is significantly lower than the loss on the validation data. It can also be observed that there are a significant amount of spikes available in the model. The training set consists of 7355 models. The validation set contains 1839 models.

The model is also used to predict the individual stress components, but the main reason for this is to see if the model was able to learn the interaction between the individual stress components. This test was done to see if the von Mises stress could be obtained more accurately from the individual stress components than directly predicting the von Mises stresses. The error on the von Mises stress prediction based on the individual stress components is given in table 8.2. It can be observed that the predicted von Mises distributions are quite accurate, although the obtained loss is higher than the loss obtained by directly predicting the von Mises stress distribution. Therefore, with this amount of training data, it is better to predict the stress distribution directly.

Table 8.2: Error created by the stress distribution predicting ML model. The individual stress components are used to determine the von Mises stress distribution. The trained data consists of 7355 models which are used to train the model. The validation data consists of 1839 models and is used to tune the model and validate the performance during learning. The test set contains 1782 models and is used to test the performance after training. It can be observed that the MSE obtained on the training set is twice as low as the error obtained on the test and validation data set.

| Error | MSE (Pa$^2$) | MAE (Pa) | MAPE (-) |
|---|---|---|---|
| Validation data | $9.229 \cdot 10^{13}$ | $4.948 \cdot 10^{6}$ | 2.649% |
| Test data | $8.035 \cdot 10^{13}$ | $4.771 \cdot 10^{6}$ | 2.525% |
| Train data | $4.673 \cdot 10^{13}$ | $4.292 \cdot 10^{6}$ | 2.246% |

It cannot be directly concluded that the model does not learn the interaction between the individual stress components since the calculation of the von Mises stress will cause an addition of individual losses. Therefore, the losses of the individual stress components are given in table 8.3. It can be observed that the losses of the individual stress components are larger than the losses of the calculated von Mises stress distribution in table 8.2. The reason is the excessive error in some of the model nodes. In some structural models, some individual nodes are predicted with a significant difference from the actual value. These losses increase some of the structural models' losses because the error gets squared in the MSE calculation. By determining the von Mises stress from those wrongly predicted individual nodes, the average loss gets less. This is why the losses of the individual stress components are higher than those obtained on the calculated von Mises stress distribution.

Table 8.3: Error created by the stress distribution predicting ML model. The MSE of all individual stress components are given. The trained data consists of 7355 models which are used to train the model. The validation data consists of 1839 models and is used to tune the model and validate the performance during learning. The test set contains 1782 models and is used to test the performance after training.

| Error (Pa$^2$) | $\sigma_x$ MSE | $\sigma_y$ MSE | $\sigma_z$ MSE | $\tau_{xy}$ MSE | $\tau_{yz}$ MSE | $\tau_{zx}$ MSE |
|---|---|---|---|---|---|---|
| Validation data | $4.239 \cdot 10^{14}$ | $3.438 \cdot 10^{14}$ | $2.445 \cdot 10^{14}$ | $1.743 \cdot 10^{14}$ | $1.124 \cdot 10^{12}$ | $3.411 \cdot 10^{13}$ |
| Test data | $3.496 \cdot 10^{14}$ | $2.748 \cdot 10^{14}$ | $2.277 \cdot 10^{14}$ | $1.470 \cdot 10^{14}$ | $1.114 \cdot 10^{12}$ | $3.308 \cdot 10^{13}$ |
| Train data | $7.828 \cdot 10^{13}$ | $4.876 \cdot 10^{13}$ | $3.818 \cdot 10^{13}$ | $3.219 \cdot 10^{13}$ | $1.092 \cdot 10^{12}$ | $1.203 \cdot 10^{13}$ |

From table 8.3, it can also be observed that the error on the stresses $\tau_{yz}$ and $\tau_{zx}$ is lower than the other individual stress components. This lower error is not directly related to the accuracy of the prediction. Those stresses have already a lower magnitude compared to the other stress components. The stress is lower because a large part of the stiffened panels is located in the xy-plane. Also, these parts are thin.

## 8.4. Scalability

For the developed model, the scalability study is also performed similarly to the one described in section 7.5. For this test, the same dataset will be used, and the same scaling steps of 5% are present. This scalability study is performed for the direct prediction of the von Mises stresses, the individual stress components, and the von Mises stress determined by the predicted individual stress components.

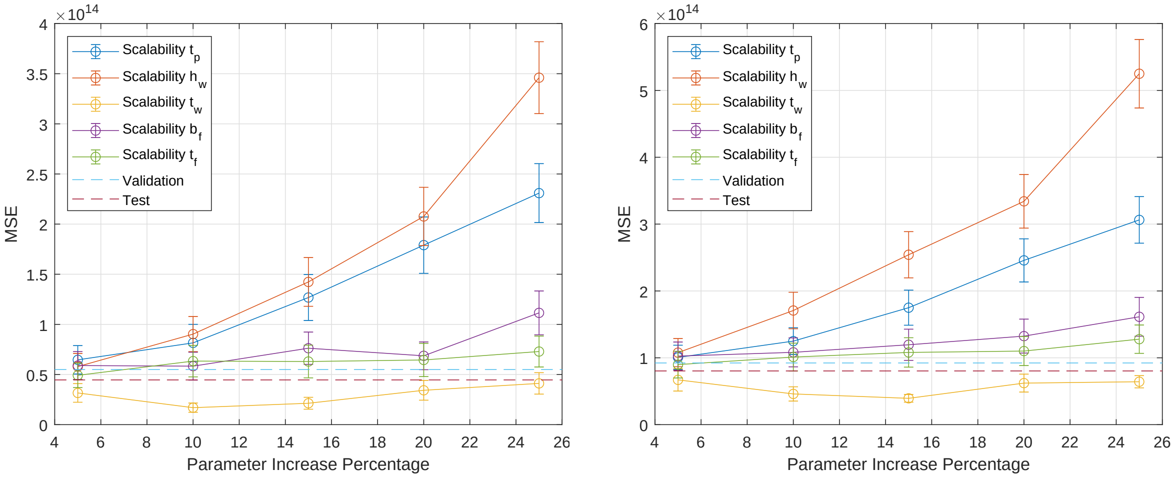

(a) Directly predicted von Mises stress MSE plot of the model developed to predict the individual stress distributions at the moment of failure. The errorbars represent the SE. It can be observed that there is an increase in error by increasing $t_p$ and $h_w$. The influence of $t_w$, $b_f$ and $t_f$ is limited. The SE of the mean becomes larger by increasing the individual parameters except for $t_w$.

(b) Individual stress component von Mises stress MSE plot of the model developed to predict the individual stress distributions at the moment of failure. The errorbars represent the SE. It can be observed that there is an increase in error by increasing $t_p$ and $h_w$. The influence of $t_w$, $b_f$ and $t_f$ is limited. The SE of the mean becomes larger by increasing the individual parameters except for $t_w$.

Figure 8.6: The MSE of both predicted von Mises stress distributions. In total 288 models used. This set is used to increase individual parameters in steps of 5%. The total set of models contains 7200 models.

Figure 8.6 shows both the MSE of both predicted von Mises stress distribution. For the directly predicted stress, it can be observed that an increase in the individual parameter does increase the loss for some of the parameters. The loss obtained by increasing the plate thickness ($t_p$) or the height of the web ($h_w$) causes a rapid increase in the error. It is interesting to see that the other parameters, the thickness of the web ($t_w$), the thickness of the flange ($t_f$), and the width of the flange ($b_f$) cause practically no increase in the loss. If these results are compared to the scalability results of the model used to predict the ultimate strength, fig. 7.6, a difference can be observed. In the model used to predict the ultimate strength, the increase of parameters caused a higher loss for every individual parameter. The loss increase of the flange parameters, the width, and thickness, was limited compared to the loss of the height of the web, web thickness, and plate thickness. Also, the losses increased significantly faster than the losses predicted with the newly developed von Mises predicting model. No apparent reason can be found explaining the difference between the results. It was expected that an increase in the individual parameters would have a similar response in both models. This increase is expected since the relation between the individual geometrical parameters would be the same, but both models obtained a different relation between the individual geometrical parameters. It is concluded that the current model is less prone to an increase in loss for models outside the range of training.

The scalability analysis is also performed on the model that is used to predict the individual stress components. The individual stress components are used to determine the von Mises stress distribution. The results of this study on the von Mises stress distribution are displayed in fig. 8.6b. Similar results are obtained as for the model that is used to predict the von Mises stress directly. A slight difference can be observed for the flange parameters, the width, and thickness, as they slowly increase beyond an increase of 15% of the individual parameters. Still, the increase of the models with a raised web height a plate thickness is more significant then the increase in loss obtained by the other geometrical parameters.

The scalability plots are also obtained for the individual stress components. The six figures are given in the following figures: fig. B.1a, fig. B.1b, fig. B.2a, fig. B.2b, fig. B.3a, and fig. B.3b. The obtained results show similar behavior as the results in fig. 8.6b. For this reason, they can be found in appendix B. One difference could be observed in predicting the individuals stress components. The increase of the thickness of the web ($t_w$) seems to lower the loss in the mean error plots. After individually inspecting the results, it became clear that by changing the web's thickness, the network less often predicts the direction of buckling incorrectly. It is also observed from those individual results, that some models show an increase in the loss by increasing the thickness of the web, while some do decrease in loss. Therefore the model shows an average decrease in the mean loss by increasing the thickness of the web.

Appendix B also shows box plots of the individual stress components and the von Mises stresses. The box plots show the performance of the individual models better, and they also show the median instead of the mean. The median helps to understand the distribution of the predicted results. The box plots show a significant spread in the results with a median substantially lower than the mean value. The medians show that the mean value is driven by the results with a considerable MSE value. All plots in Appendix B show the corresponding mean MSE error on the test and validation set.

From the loss curves during the model's training and the results obtained from scalability, it is concluded that the model is not stable with its predictions and shows some unexpected behavior. Thus, it is decided not to perform a study on how the number of training examples influences the performance of the model. Due to the model's unexpected behavior, no accurate conclusion can be drawn regarding the number of training examples.

## 8.5. Generalizability

The developed stress predicting ML model is also tested on its generalizability on different input data. To test the generalizability performance of the ML model, the same data is used as for the ultimate strenght predicting ML model. In total, 1440 curved plates are tested with five different curvatures, as described in section 7.7. Both stress distribution predicting models are tested on their generalizability. Just like in section 7.7, it is expected that the ML models will not be able to accurately predict the stress distribution over the stiffened panel at the moment of failure. It is even expected that some parts of the bottom plating will be seen as nodes on the stiffeners since these are the nodes that contain information in the z-direction in the training data. It is also expected that some stiffener nodes will have results similar to that of the bottom plating since they are now located at zero height due to the downward curvature of the stiffened panel.

The results for the individual stress component predictions are given in table 8.4. The same results are graphically represented in fig. 8.8a. From these results, it can be observed that the error is larger than the error obtained on the test and training set, but the difference is less distinct than the error obtained by the ultimate strength predicting ML model. Also worth noting is that the mean error does not increase by increasing the curvature of the stiffened panel. When looking at the individual model performance, a clear difference can be observed between the generalizability models and, for example, the test models. When predicting the stress distribution on models in the test set, some nodes in the models are near perfectly determined, and some are less accurate. The prediction on the generalizability model shows bad prediction on every single node. Therefore, it is decided to inspect the individual models graphically.

Table 8.4: Error created by the stress distribution predicting ML model. The MSE of all individual stress components are given. The generalizability dataset consists of 1440 models with five different heights (H) in steps of 0.2 meter.

| Error (Pa$^2$) | $\sigma_x$ MSE | $\sigma_y$ MSE | $\sigma_z$ MSE | $\tau_{xy}$ MSE | $\tau_{yz}$ MSE | $\tau_{zx}$ MSE |
|---|---|---|---|---|---|---|
| 0.2 m | $5.741{\cdot}10^{15}$ | $5.256{\cdot}10^{15}$ | $1.836{\cdot}10^{15}$ | $1.909{\cdot}10^{15}$ | $6.931{\cdot}10^{13}$ | $2.277{\cdot}10^{14}$ |
| 0.4 m | $5.184{\cdot}10^{15}$ | $4.231{\cdot}10^{15}$ | $1.054{\cdot}10^{15}$ | $1.275{\cdot}10^{15}$ | $2.379{\cdot}10^{14}$ | $1.805{\cdot}10^{14}$ |
| 0.6 m | $8.183{\cdot}10^{15}$ | $3.896{\cdot}10^{15}$ | $8.808{\cdot}10^{14}$ | $9.164{\cdot}10^{14}$ | $4.430{\cdot}10^{14}$ | $1.874{\cdot}10^{14}$ |
| 0.8 m | $1.677{\cdot}10^{16}$ | $4.513{\cdot}10^{15}$ | $1.091{\cdot}10^{15}$ | $8.570{\cdot}10^{14}$ | $6.692{\cdot}10^{14}$ | $2.293{\cdot}10^{14}$ |
| 1.0 m | $5.184{\cdot}10^{15}$ | $4.231{\cdot}10^{15}$ | $1.054{\cdot}10^{15}$ | $1.275{\cdot}10^{15}$ | $2.379{\cdot}10^{14}$ | $1.805{\cdot}10^{14}$ |

When graphically inspecting the individual models, it is again observed that some of the models are predicted to buckle in the wrong direction, which results in a high loss. Models that buckle in the correct direction according to the ML still have a high error. An example is shown in fig. 8.7. This is the result of a model with a mid-plate height of 0.2 meter, which is the smallest curvature tested in this research. Figure 8.7a shows the von Mises stress determined by the predicted individual stress components. Figure 8.7c shows the real von Mises stress distribution. The left side of the image represents the bottom plating, and the shape of the predicted result is fairly accurate, although the magnitudes of the stresses are not correct. The right side of the image contains the stresses over the webs and the flanges. It can be observed from the graphical representation that the ML model does not know how to handle the nodes since the predicted outcome has no physical meaning. Also, it is observed that in the predicted stress distribution, stresses occur far beyond the yield strength ($\sigma_y$) of the material. This maximum predicted stress becomes larger with a more strongly curved stiffened panel. This increase is similar to the generalizability results obtained by the ultimate strength predicting ML model.

Table 8.5: Error created by the stress distribution predicting ML models. The von Mises stress distribution is both determined by direct prediction and prediction by making use of the individual stress components. The error is large, but there is no clear increase observed by increasing the curvature of the stiffened panel

| H (m) | VM 1D MSE | VM 6D MSE |
|---|---|---|
| 0.2 m | $2.136{\cdot}10^{15}$ | $2.047{\cdot}10^{15}$ |
| 0.4 m | $4.414{\cdot}10^{15}$ | $2.491{\cdot}10^{15}$ |
| 0.6 m | $4.109{\cdot}10^{15}$ | $5.037{\cdot}10^{15}$ |
| 0.8 m | $2.358{\cdot}10^{15}$ | $1.182{\cdot}10^{16}$ |
| 1.0 m | $4.414{\cdot}10^{15}$ | $2.491{\cdot}10^{15}$ |

The von Mises results of the generalizability data are displayed in table 8.5. Similar to the results in table 8.4, no clear increase can be observed by increasing the curvature of the stiffened panel. Compared to the results in table 8.1 and table 8.2 the obtained error is significantly larger. The results are also graphically represented in the line plot fig. 8.8b. Figure 8.7b shows a directly predicted stress distribution of the von Mises stress distribution. It is interesting to observe that the results are significantly different from the distribution of fig. 8.7a. The directly predicted von Mises stress show no excessive large predicted stresses beyond the material yield strength.

Appendix C contains box plots of the individual stress components and both of the von Mises stress distributions per curvature step. These are given since they provide more information on the spread and distribution of the results compared to fig. 8.8. Most of the figures show similar behaviour compared to the results in table 8.4 and table 8.5. Although, the stress in the x-direction ($\sigma_x$) and the shear in yz-plane ($\tau_{yz}$) show an increase in the median of the error and spread of the results when increasing the curvature of the stiffened panels. Due to the magnitude of $\sigma_x$ in the von Mises stress determined by the individual stress components shows similar behavior.

(a) Predicted von Mises stress distribution over the stiffened panel determined by the individual stress components. The prediction of the stress distribution over the stiffeners is incorrect. The maximum occurring values are significantly higher than the material yield strength.

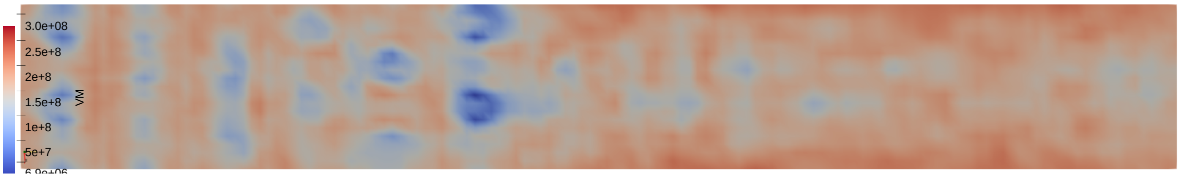

(b) Directly predicted von Mises stress distribution over the stiffened panel. The prediction of the stress distribution over the stiffeners is incorrect. The maximum occurring values are significantly higher than the material yield strength.

(c) Real von Mises stress distribution over the stiffened panel.

Figure 8.7: Predicted and real von Mises stress distribution over the stiffened panel. The stiffened panel has a height of 0.2 meters mid plane. This is the lowest curvature that is tested. The images shows the flat representation of the 3-D stiffened panel. The left section of the plate represents the plating in between stiffeners. The middle section of the image contains the webs of the stiffeners. The right side of the image contains the flanges of the stiffened panel.

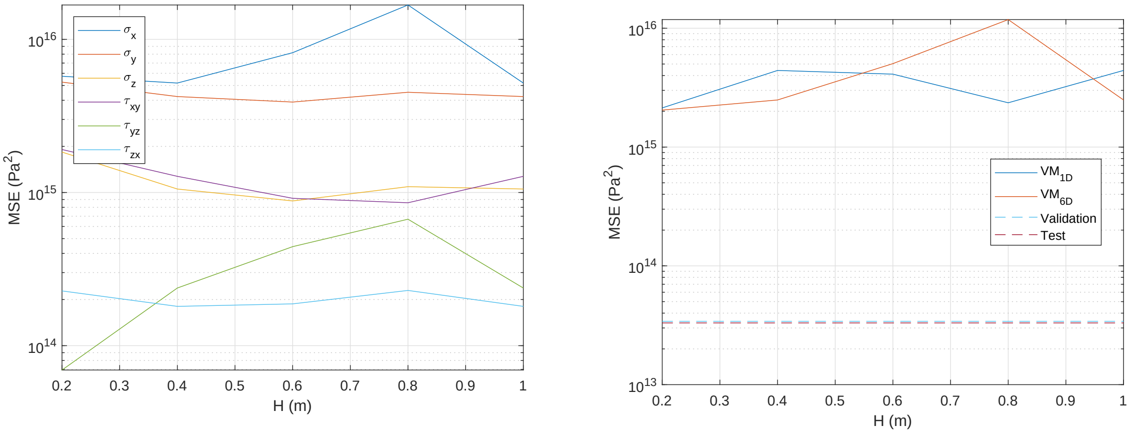

(a) Generalizability MSE graph of the individual stress components. No clear increase can be observed for the individual stress components with an increase in curvature of the stiffened panel.

(b) Generalizability MSE graph of the von Mises stress. Both the direct predicted von Mises stress ($VM_{1D}$), and the von Mises stress determined from the individuals stress components ($VM_{6D}$) is plotted.

Figure 8.8: Generalizability MSE plot of the model developed to predict the stress distribution at moment of failure. In both graph, no clear trend can be observed when the curvature gets increased.

Overall, it can be concluded that the generalizability performance of the stress distribution predicting ML model shows insufficient performance. Obtained losses are significantly large, and the predicted stress distributions are unrealistic and inaccurate. The von Mises stress determined from the individual stress components shows even stresses significantly larger than the material yield strength. Therefore it can be concluded that the performance on generalizability is poor, and obtained results cannot be used for accurate stress distribution estimates.

## 8.6. Conclusion

Overall it can be concluded that a large amount of the stress distributions is correctly predicted, and even if the result is flipped, the estimate is reasonably accurate and follows the right stress distribution. Although, by inspecting the loss graphs and the scalability and generalizability performance of the trained models, it is concluded that the ML-model predicts some unexpected results and, in some cases, shows difficulties in predicting the direction of buckling.

From the scalability study, it is observed that only increasing the height of the web ($h_w$) or the thickness of the plate ($t_w$) causes a significant increase in the loss. The other parameters show little to no increase. By inspecting the performance of the individual stiffened panels, it can be concluded that some models do increase in loss, while other models do decrease in loss. Therefore no clear conclusion can be given on how well the model performs on models outside the range of training.

The performance on the generalizability data shows that the developed ML model cannot correctly predict the stress distributions over the stiffened panels. The obtained errors are of such a large magnitude that they cannot be considered useful for further usage. Also, after graphically inspecting individual results, it is observed that the results contain no significant physical information. This conclusion is not unexpected since there is no curvature information present in the data used for training the ML model. The results make clear that the amount of curvature does not directly influence the magnitude of the obtained error.

From the conclusions, it is suggested to develop a new custom loss function that automatically detects if a result is flipped or not, and selects the correct result. There is no physical meaning as to why the plate should buckle in one of the directions. The buckling of straight plates is an unstable process, therefore, the plate can buckle in either direction. If this does not improve the process of learning, it is recommended to pay attention to the individual nodes that are inaccurately predicted that cause a significant increase in the entire model's loss. With a suitable loss function, it is expected that the model will behave like the loss curve obtained on the training set, which shows a steady decrease in the loss function. When an adequate loss function is developed, it is recommended to perform a new scalability and generalizability test to see if the obtained results match the current findings. Also, if good loss curves are obtained during training, it is advised to test the required number of training examples needed for good accurate predictions.

# IV

# Conclusion and Recommendations

# 9

# Conclusions

In this research, Machine Learning (ML) is used to predict the ultimate buckling strength and the stress distribution at the moment of failure of meshed stiffened panels. The main research question of this research is:

*Under what conditions is it possible to predict buckling and plasticity for a meshed stiffened panel making use of machine learning?*

To answer the main research question, an optimization is performed with an analytical model to obtain a representative set of geometrical parameters for stiffened panels in a ship structure. Numerical analysis is performed on the acquired set of parameters to develop a large dataset of stiffened panel models. With the numerical analysis, the ultimate strength of the stiffened panels and the stress distributions over the entire stiffened panel at the moment of failure are determined. This collected dataset is used to train two different machine learning models. One model is developed to predict the ultimate strength, while the other developed model is used to predict the stress distributions. The trained machine learning models are then used to determine under what conditions it is possible to predict buckling and plasticity for meshed ship structures. The previously described steps are used to answer the sub-questions which support the main research goal. The conclusions of the individual sub-questions will be discussed. At the end of this chapter a conclusion will be formed.

1. *Which range of geometric parameters covers a comprehensive set in shipbuilding, and captures all different types of buckling/local failure?* - An analytical model is applied based on the theory of Hughes and Paik [7] to answer this sub-question. This model incorporates five different buckling modes, residual stress, initial deflections, and classification rules to obtain a realistic set of parameters. The representative geometrical dataset turns out to be highly dependent on the type of vessel and the length and width of the stiffened panel. This study also clarifies that the parameter set depends on the direction of loading and the expected maximum loading of the stiffened panel. Also, it became clear that a significant amount of the parameter combinations obtained is close to the limits allowed by classification societies. In this research, a small correlation study is performed on the collected dataset. This study showed a strong correlation between the individual geometrical parameters of the stiffened panels.

   To conclude on this sub-question: A representative parameter range is case dependent and does rely on a substantial amount of factors. There is no distinct set that is a good representation of all types of vessels and types of loading.

2. *Which type of ML-model is suitable to predict local structural failure? Also, which type of training algorithm is efficient to train this ML-model?* - The selection of the type of ML model can often be made based on the kind of data that will be used within the research. There is no golden standard on which type of model to use. In this research, the ultimate strength and stress distribution over the stiffened panel at the moment of failure are predicted. The ultimate strength and stresses are numerical values. The prediction of numeric values is considered a regression problem. Neural networks are often used for regression tasks. In this research, it is concluded that if the entire mesh of a stiffened panel is transformed into one dataset it contains a significant amount of geometrical information. Also, there is the possibility to incorporate other parameters, like material properties within the same data structure, which is relevant for future research. If the mesh is used as data, the size of the input data becomes significantly large. For this reason, the choice has been made to use a convolutional neural network. Besides that convolutional neural

networks are efficient for large-sized inputs, they have the significant advantage of maintaining spatial information throughout the process of learning. Individual nodes in a mesh interact with each other and influence their deformations and stresses. Due to the conservation of spatial information, the developed network can learn the interaction between data points.

In this research, several optimizers have been tested to train the machine learning model. With the right selection of optimizer parameters, most optimizers were able to make the network learn from the presented data. In the end, the adaptive optimizer Adamax showed the best performance and is used for this research.

3. *How can the ML-model be trained to determine the ultimate strength of the stiffened panel without the ML-model knowing how it will fail?* - There is no clear answer to this sub-question. Machine learning models consist of layers with trainable parameters, called weights, which are continuously changed during learning to predict the correct output. It is difficult to understand what every parameter inside the developed machine learning model physically represents. With a combination of consecutive linear and non-linear functions, the model performs an accurate complex regression to estimate the ultimate strength of a stiffened panel. The mesh's data is first compressed to a smaller array of data, which contains information about the original input. This compressed input is then used to predict the ultimate strength of the stiffened panel. The network does not determine the residual stresses, initial deflections, or the expected mode of buckling. Instead, the network learns to directly output the ultimate strength without the intermediate steps required when performing standard numerical or analytical analysis.

4. *When is the ML-model fully converged, and what is the minimal amount of training data needed for acceptable convergence?* - The machine learning model is considered fully converged when the weights and other parameters in the model are such that the lowest possible error is obtained on the validation set. The developed model was able to achieve good accuracy already after 2000 epochs. An epoch is a single pass of the entire set of data through the network. After 2000 epochs, the loss curve starts to flatten, and only little improvement is obtained with performing more epochs. The model is in total trained for 20000 epochs to show the development of the loss after more epochs. After 20000 epochs, a decreasing trend in the loss function is still observed. After 20000 epochs, an error of 0.139% is obtained on the test set. If the increase in accuracy is compared to the increase in required training time, it is considered not efficient to train the model for longer. This consideration especially becomes true if the error of the network is compared to the error created by the coarse meshing of the stiffened panel in the numerical data generation. The average obtained error from the mesh convergence study showed an average error of 4.2%. It is concluded that machine learning shows excellent capabilities in accurately predicting the ultimate strength. The most improvement in accuracy can be obtained from generating more accurate input data for the machine learning.

   By training the model with the fully developed dataset, the performance of the model is also tested with less training data. The network is repetitively trained with a minimum of 10% of the original data size and a maximum of 90% of the original data size. The set is increased in steps of 10%. It is observed that at 50% of the full dataset, this is 3678 models, already shows accurate predictions made by the trained network. Until this amount of training data, a great increase in performance can be observed by increasing the amount of data. By expanding the dataset beyond the 50%, more accurate results will be obtained, but this requires significantly more models to reduce the error of the prediction by the same amount as before the 50% data size. From the results, it can also be concluded that with small amounts of training data, the range and spread of the data becomes more important. The network is trained 72 times in total, 8 times for every dataset size, while the datasets were randomly sampled. With small amounts of training data, a wide spread in the model's performance could be observed. This spread becomes less with a larger dataset. It is recommended to have at least 4000 widely spread stiffened panels model in the training data to obtain accurate predictions. Better performance can be obtained by increasing the amount of available data.

5. *Is the trained ML-model able to predict results outside its training scope, so-called 'scalability' and 'generalizability'. If so, to what level of extrapolation are results considered useful?* - A selection has been made from the dataset used for training to test the scalability of the model.

With this selection, a new set of small datasets has been developed by increasing the individual geometrical parameters of the stiffened panel by 5%. The maximum scaled models have a single geometrical parameter that is increased by 25% of the original value. With the selected set, still accurate results were obtained when the individual parameters were scaled by 5%. By further increasing the geometrical parameters, the error also starts to grow. At a 15% increase of the plate thickness, the mean squared error already increased by a factor 3. The same increase in the height of the web already increases the error by a factor 13. A factor of 7 for the increase in error is obtained for magnifying the thickness of the web. The flange parameters showed less importance and only doubled the error. At 25% increase of the geometrical parameters, some parameters showed an error increase by a factor 250. The flange parameters, the thickness and width, showed only a factor 10 and 20 increase of the loss at 25%. It can be concluded that the flange parameters are not as important in predicting the ultimate strength as the thickness of the plate and the web parameters. It also can be concluded that a 5% range outside the original dataset still results in acceptable predictions. When the geometrical parameters are further away than this 5% of training, the accuracy of the prediction rapidly decreases.

The data used for testing the generalizability is the same initial set as used for the scalability test. This set is used to make curved plates. The stiffened panels are curved in the transverse direction only with the stiffeners point towards the center of curvature. Five different curvatures are tested defined by the mid-plate height. The mid-plate height is increased in steps of 0.2 meter until a height of 1 meter is reached for a 4 meter wide stiffened panel. The results show that for both developed ML-models the predictions are considered insufficiently accurate to be acceptable for further usage. The predicted stress distributions also show unexpected results with strange distribution patterns. The obtained performance was expected since the data used for training the ML-model contains no information about curvature. The performance of the model on generalizability is not sufficient, but the predictions are as expected.

Overall, it can be said that machine learning can be considered an excellent tool to predict the ultimate strength of stiffened panels. This statement is only valid when there is sufficient data available to obtain stable learning of the algorithm. When more data is available, the model is more likely to become well trained. The trained model can achieve accurate predictions as long as the input parameters lay within a 5% margin of the original data that is used to train the model. Outside this range, there is no guarantee that the model can predict results correctly. For a similar machine learning model with a similar dataset for training, it is recommended to have at least 4000 training examples with a good spread in geometrical parameters to obtain stable learning. When data becomes more complex, due to, for example, the introduction of more geometrical parameters, it is probably necessary to increase the size of the dataset that will be used for training the machine learning model. Also, it is recommended to only use the machine learning model for tasks similar to what it is initially trained on. The generalizability of the model is poor, and the results are not useful for further usage.

# 10

# Recommendations

Based on the research and the conclusions obtained, a set of recommendations for further research will be given and discussed:

1. The scalability study of the developed machine learning model shows that results predicted for structural models outside the training scope quickly become inaccurate. Therefore, it is recommended to increase the amount of training data and perform the scalability tests again to see if more training data would improve the predictive capabilities of the developed model.
2. In the current research, data is used from which both the input and output are known. When applying the trained model on new data with an unknown output, a mesh of the model would still be required. The recommendation is to extend the model with a part that can generate the mesh from a couple of geometrical parameters to overcome the need to create a mesh with numerical software. For simple structures, this could be done by writing a code that directly creates the mesh. When using a wider variety of models, or even multiple different structural geometries, the advice is to develop a neural network that can create the mesh. This predicted mesh is then the input for the current developed network.
3. Residual stress is used in the developed analytical model to obtain a realistic dataset. Incorporating residual stress in the numerical analysis is complicated and is therefore not performed in this research. For further research, it is recommended to take the residual stress into account for the numerical created data to obtain more realistic results.
4. The developed model in this research showed the ability to predict the stress distributions over the stiffened panel. Expected is that the model is also able to predict the deformations of the stiffened panels. In this research, the initial deflection is determined by scaling the deformations of the eigenvalue buckling analysis. In reality, the shape of the initial deflection will be more complicated. If there is sufficient experimental data available for the initial deflection of stiffened panels, the recommendation is to test if machine learning can accurately predict the realistic initial deflection of stiffened panels based on their geometry. The same principle applies to learn realistic residual stress distributions in the stiffened panel. If this turns out to be possible, more accurate, numerical results can be obtained by applying the realistically predicted initial deflection and residuals stress. Currently, simplified models are used to incorporate these effects within numerical analysis.
5. In this research, the input size of the machine learning model is fixed. Nowadays, it is possible to develop a machine learning model that can handle different sizes of input data. The suggestion is to adjust the model so it could handle different sized inputs to the network. If the machine learning model can handle different sizes of inputs, it will create the opportunity to test structural models with various shapes and with varying densities of the mesh. Allowing variable input sizes would make the developed model more readily usable for ultimate strength and stress predictions.
6. The developed dataset only uses simply supported stiffened panels, loaded with longitudinal uniaxial compression and lateral pressure. In reality, the boundary conditions of continuous stiffened panels behave partially rotational restrained, which is challenging to model accurately. Next to this, the loading conditions are more complicated in real situations than used in this research. Stiffened panels in ships are loaded by a combination of bi-axial compression, lateral pressure, shear force, and bending moments. It is recommended to add new layers of data to the input

data that contains information about the boundary conditions and their locations. The suggestion is also to add layers of information about the loading of the stiffened panel to the input data. The addition of different boundary conditions and loading conditions would require the development of new data, but would significantly increase the trained machine learning model's versatility.

7. Excellent accuracy is obtained on the prediction of the ultimate strength of stiffened panels. The error caused by the machine learning model is significantly lower than the error obtained by coarsely meshing the stiffened panels for the data generation. If the machine learning model is used to predict the ultimate strength accurately, the suggestion is to train the network on data with a finer mesh to reduce the error created during numerical analysis.

8. Instead of using the machine learning model to predict the ultimate strength, it could also be turned into a classifier model that could predict the expected mode of buckling if this is a desired feature. A classifier model could also be incorporated as a parallel neural network that uses the same compressed geometrical information to predict the buckling mode during failure. This way, the model would predict the buckling mode as well as the ultimate strength. The predicted buckling mode would provide structural engineers with information on how to strengthen the stiffened panel.

Based on the recommendations, it can be concluded that the developed model shows many new opportunities for the application of machine learning in predicting the ultimate strength and stress distributions of stiffened panels.

# V

# Bibliography and Appendices

# Bibliography

[1] Y. Sumi, Y. Kawagoe, M. Kidogawa, K Kobayashi, Y. Nakajima, T. Nakano, M. Sunouchi, K. Tamura, and N. Ueda. Final report of committee on large container ship safety. Report, 2015.

[2] DNV GL. Class guidline - buckling. DNVGL-CG-0128, 2015.

[3] H. Salehi and R. Burgueño. Emerging artificial intelligence methods in structural engineering. *Engineering Structures*, 171:170–189, 2018. ISSN 01410296. doi: 10.1016/j.engstruct.2018.05.084.

[4] N. Anwar and F. Najam. *Structural Cross Sections: Analysis and Design*. Butterworth-Heinemann, 2016. ISBN 978-0-12-804443-8. doi: 10.1016/B978-0-12-804443-8.00009-9.

[5] J.K. Paik, K. Branner, Y.S. Choo, J. Czujko, M. Fujikubo, J. Gordo, G. Parmentier, R. Iaccarino, N. Pasqualino, D. Wang, X. Wang, and S. Zhang. Committee III.1 - ultimate strength. proceedings of the 17th international ship and offshore structures congress (ISSC). Report, 2009.

[6] Y. Bai and W.L. Jin. *Marine Structural Design*. Elsevier Science, 2015. ISBN 9780081000076.

[7] O.F. Hughes and J.K. Paik. *Ship Structural Analysis and Design*. Society of Naval Architects and Marine Engineers (SNAME), 2010. ISBN 978-0-939773-78-3.

[8] E. Alpaydin. *Introduction to Machine Learning*. MIT Press, 2010. ISBN 9780262012430.

[9] Y. Liu. Effects of mesh density on finite element analysis. In *SAE World Congress*, volume 2, SAE Technical Papers. doi: 10.4271/2013-01-1375.

[10] O.F. Hughes, J.K. Paik, and D. Béghin. *Ship structural analysis and design*. Society of Naval Architects and Marine Engineers, Jersey City, N.J., 2010. ISBN 9781613441404 9780939773787.

[11] MIT. *Structural Mechanics: 2.080 Lecture 11*. 2013.

[12] S.P. Timoshenko and J.M. Gere. *Theory of Elastic Stability*. Dover Publications, 2012. ISBN 9780486134802.

[13] S.K. Duggal. *Limit State Design of Steel Structures*. McGraw Hill Education, 2014. ISBN 9789351343493.

[14] J.K. Paik. *Ultimate Limit State Analysis and Design of Plated Structures*. Wiley, 2018. ISBN 9781119367796.

[15] C.S. Smith, N. Anderson, J.C. Chapman, P.C. Davidson, and P.J. Dowling. Strength of stiffened plating under combined compression and lateral pressure. *The Royal Institution of Naval Architects (RINA)*, 134:131–147, 1991.

[16] Ansys. *Mechanical APDL 19.0 - Mechanical APDL Element Reference: Part I*. 2019.

[17] Ž. Ivezić, A.J. Connolly, J.T. Van der Plas, and A. Gray. *Statistics, Data Mining, and Machine Learning in Astronomy A Practical Python Guide for the Analysis of Survey Data*. Princeton University Press, stu - student edition edition, 2014. ISBN 9780691151687. doi: 10.2307/j.ctt4cgbdj.

[18] Z. Zuo, B. Shuai, G. Wang, X. Liu, X. Wang, B. Wang, and Y. Chen. Convolutional recurrent neural networks: Learning spatial dependencies for image representation. In *2015 IEEE Conference on Computer Vision and Pattern Recognition Workshops (CVPRW)*, pages 18–26. ISBN 2160-7516. doi: 10.1109/CVPRW.2015.7301268.

[19] A. Amidi and S. Amidi. *VIP Cheatsheet: Convolutional Neural Networks*. Stanford University, 2018.

[20] H. Wu and X. Gu. Max-pooling dropout for regularization of convolutional neural networks. 2015.

[21] W. Rawat and Z. Wang. Deep convolutional neural networks for image classification: A comprehensive review. *Neural Computation*, 29:1–98, 2017. doi: 10.1162/NECO_a_00990.

[22] J. Gu, Z. Wang, J. Kuen, L. Ma, A. Shahroudy, B. Shuai, T. Liu, X. Wang, G. Wang, J. Cai, and T. Chen. Recent advances in convolutional neural networks. *Pattern Recognition*, 77:354–377, 2018. ISSN 0031-3203. doi: https://doi.org/10.1016/j.patcog.2017.10.013.

[23] B. Xu, N. Wang, T. Chen, and M. Li. Empirical evaluation of rectified activations in convolutional network. 2015.

[24] A. Moujahid. *A Practical Introduction to Deep Learning with Caffe and Python*. 2016. URL http://adilmoujahid.com/posts/2016/06/introduction-deep-learning-python-caffe/.

[25] M.C.M. Bakker, M. Rosmanit, and H. Hofmeyer. Approximate large-deflection analysis of simply supported rectangular plates under transverse loading using plate post-buckling solutions. *Thin-walled Structures*, 46(11):1224–1235, 2008. ISSN 02638231. doi: 10.1016/j.tws.2008.02.003.

[26] J.K. Paik and B.J. Kim. Ultimate strength formulations for stiffened panels under combined axial load, in-plane bending and lateral pressure: a benchmark study. *Thin-Walled Structures*, 40(1): 45–83, 2002. ISSN 0263-8231. doi: 10.1016/s0263-8231(01)00043-x.

[27] J.K. Paik, A.K. Thayamballi, and B. Ju Kim. Large deflection orthotropic plate approach to develop ultimate strength formulations for stiffened panels under combined biaxial compression/tension and lateral pressure. *Thin-Walled Structures*, 39(3):215–246, 2001. ISSN 0263-8231. doi: 10.1016/s0263-8231(00)00059-8.

[28] J.K. Paik. Empirical formulations for predicting the ultimate compressive strength of welded aluminum stiffened panels. *Thin-Walled Structures*, 45(2):171–184, 2007. ISSN 0263-8231. doi: 10.1016/j.tws.2007.02.003.

[29] M.R. Khedmati, H.R. Memarian, M. Fadavie, and M.R. Zareei. Empirical formulations for estimation of ultimate strength of continuous aluminium stiffened plates under combined transverse compression and lateral pressure. *Ships and Offshore Structures*, 11(3):258–277, 2016. ISSN 1744-5302. doi: 10.1080/17445302.2014.985430.

[30] M. Zareei and M.R. Iranmanesh. Ultimate strength formulation of stiffened panels under in-plane compression or tension with cracking damage. *Journal of Naval Architecture and Marine Engineering*, 15(1):1–16, 2018. ISSN 2070-8998. doi: 10.3329/jname.v15i1.31668.

[31] D.G. Stamatelos, G.N. Labeas, and K.I. Tserpes. Analytical calculation of local buckling and post-buckling behavior of isotropic and orthotropic stiffened panels. *Thin-Walled Structures*, 49 (3):422–430, 2011. ISSN 0263-8231. doi: https://doi.org/10.1016/j.tws.2010.11.008.

[32] D.A. Danielson and A. Wilmer. Buckling of stiffened plates with bulb flat flanges. *International Journal of Solids and Structures*, 41(22-23):6407–6427, 2004. ISSN 0020-7683. doi: 10.1016/j.ijsolstr.2004.05.063.

[33] Z.H. Mohammad, E. Nouri, M.R. Khedmati, and M.M. Roshanali. Degradation of the compressive strength of unstiffened/stiffened steel plates due to both-sides randomly distributed corrosion wastage. *Latin American Journal of Solids and Structures*, 7(3):335–367, 2010. ISSN 1679-7825. doi: 10.1590/S1679-78252010000300006.

[34] D.K. Kim, D.K. Park, J.H. Kim, S.J. Kim, B.J. Kim, J.K. Seo, and J.K. Paik. Effect of corrosion on the ultimate strength of double hull oil tankers - Part I: Stiffened panels. *Structural Engineering and Mechanics*, 42(4):507–530, 2012. ISSN 1225-4568. doi: 10.12989/sem.2012.42.4.507.

[35] T. Yao and M. Fujikubo. *Buckling and ultimate strength of ship and ship-like floating structures*. Butterworth-Heinemann, Kidlington, Oxford; Singapore, 2016. ISBN 9780128038499 0128038497.

[36] Z. Qiu, X. Wang, and Z. Li. Post-buckling analysis of a thin stiffened plate with uncertain initial deflection via interval analysis. *International Journal of Non-Linear Mechanics*, 44(10):1031–1038, 2009. ISSN 00207462. doi: 10.1016/j.ijnonlinmec.2009.08.001.

[37] B. Chen and C.G. Soares. A simplified model for the effect of weld-induced residual stresses on the axial ultimate strength of stiffened plates. *Journal of Marine Science and Application*, 17(1): 57–67, 2018. ISSN 1671-9433 1993-5048. doi: 10.1007/s11804-018-0007-7.

[38] E. Byklum and J. Amdahl. A simplified method for elastic large deflection analysis of plates and stiffened panels due to local buckling. *Thin-Walled Structures*, 40(11):925–953, 2002. ISSN 0263-8231. doi: 10.1016/s0263-8231(02)00042-3.

[39] Y. Okumoto, Y. Takeda, M. Mano, and T. Okada. *Design of ship hull structures: A practical guide for engineers*. 2009. ISBN 978-3-540-88444-6 978-3-540-88445-3. doi: 10.1007/978-3-540-88445-3.

[40] J.K. Paik, D.K. Kim, H.L. Lee, and Y.L. Shim. A method for analyzing elastic large deflection behavior of perfect and imperfect plates with partially rotation-restrained edges. *Journal of Offshore Mechanics and Arctic Engineering*, 134(2), 2012. ISSN 0892-7219 1528-896X. doi: 10.1115/1.4004632.

[41] M. Xu, M. Fujikubo, and C. Guedes Soares. *Influence of Model Geometry and Boundary Conditions on the Ultimate Strength of Stiffened Panels Under Uniaxial Compressive Loading*, volume 135. 2012. doi: 10.1115/OMAE2012-84262.

[42] M.C. Xu, D. Yanagihara, M. Fujikubo, and C. Guedes Soares. Influence of boundary conditions on the collapse behaviour of stiffened panels under combined loads. *Marine Structures*, 34: 205–225, 2013. ISSN 0951-8339. doi: 10.1016/j.marstruc.2013.09.002.

[43] J. Pan, N. Li, Z.J. Song, and M.C. Xu. Influence of boundary condition and stiffener type on collapse behaviours of stiffened panels under longitudinal compression. *Advances in Mechanical Engineering*, 11(10), 2019. ISSN 1687-8140. doi: 10.1177/1687814019884762.

[44] J. Du, P. Yang, C. Cui, and T. Xia. Ultimate strength of steel panels and stiffened plates with longitudinal through-thickness cracks under compression. 2016. doi: 10.2991/icseee-15.2016.146.

[45] M.R. Khedmati, A. Bayatfar, and P. Rigo. Post-buckling behaviour and strength of multi-stiffened aluminium panels under combined axial compression and lateral pressure. *Marine Structures*, 23(1):39–66, 2010. ISSN 0951-8339. doi: 10.1016/j.marstruc.2009.10.003.

[46] C. Li, S. Dong, T. Wang, W. Xu, and X. Zhou. Numerical investigation on ultimate compressive strength of welded stiffened plates built by steel grades of s235–s390. *Applied Sciences*, 9(10): 2088, 2019. ISSN 2076-3417. doi: 10.3390/app9102088.

[47] M.R. Khedmati and P. Edalat. A numerical investigation into the effects of parabolic curvature on the buckling strength and behaviour of stiffened plates under in-plane compression. *Latin American Journal of Solids and Structures*, 7(3):249–264, 2010. ISSN 1679-7825. doi: 10.1590/S1679-78252010000300002.

[48] J.S. Park, Y.C. Ha, and J.K. Seo. Estimation of buckling and ultimate collapse behaviour of stiffened curved plates under compressive load. *Journal of Ocean Engineering and Technology*, 34(1):37–45, 2020. ISSN 1225-0767 2287-6715. doi: 10.26748/ksoe.2019.108.

[49] B. Wu, A. Pagani, M. Filippi, W.Q. Chen, and E. Carrera. Large-deflection and post-buckling analyses of isotropic rectangular plates by carrera unified formulation. *International Journal of Non-Linear Mechanics*, 116:18–31, 2019. ISSN 0020-7462. doi: 10.1016/j.ijnonlinmec.2019.05.004.

[50] L. Huang, B. Li, and Y. Wang. Fem and efg quasi-static explicit buckling analysis for thin-walled members. *Open Journal of Civil Engineering*, 07(3):432–452, 2017. ISSN 2164-3164 2164-3172. doi: 10.4236/ojce.2017.73030.

[51] S. Sadamoto, S. Tanaka, K. Taniguchi, M. Ozdemir, T. Q. Bui, C. Murakami, and D. Yanagihara. Buckling analysis of stiffened plate structures by an improved meshfree flat shell formulation. *Thin-Walled Structures*, 117:303–313, 2017. ISSN 02638231. doi: 10.1016/j.tws.2017.04.012.

[52] S. Jin, Z. Li, F. Huang, D. Gan, R. Cheng, and G. Deng. Constrained shell finite element method for elastic buckling analysis of thin-walled members. *Thin-Walled Structures*, 145:106409, 2019. ISSN 0263-8231. doi: 10.1016/j.tws.2019.106409.

[53] M.Z. Haffar and S. Ádány. On the buckling of longitudinally stiffened plates, part 1: Modal analysis by the constrained finite element method. *Thin-Walled Structures*, 145:106394, 2019. ISSN 0263-8231. doi: 10.1016/j.tws.2019.106394.

[54] E. Steen, E. Byklum, K. Vilming, and T. Østvold. Computerized buckling models for ultimate strength assessment of stiffened ship hull panels. 2004.

[55] M.A. Khan. *Accelerated Bridge Construction: Best Practices and Techniques*. Elsevier Science, 2014. ISBN 9780124072244.

[56] G. Hancock and C. Pham. Developments in the finite strip buckling analysis of plates and channel sections under localised loading. *22nd International Specialty Conference on Recent Research and Developments in Cold-Formed Steel Design and Construction*, pages 295–309, 2014.

[57] D. Wei and S. Zhang. Ultimate compressive strength prediction of stiffened panels by counter-propagation neural networks (CPN). In *The Ninth International Offshore and Polar Engineering Conference*, page 6. International Society of Offshore and Polar Engineers.

[58] S.K. Babanajad, A.H. Gandomi, and A.H. Alavi. New prediction models for concrete ultimate strength under true-triaxial stress states: An evolutionary approach. *Advances in Engineering Software*, 110:55–68, 2017. ISSN 09659978. doi: 10.1016/j.advengsoft.2017.03.011.

[59] H. Tekeli, K.A. Korkmaz, F. Demir, and A.I. Carhoglu. Comparison of critical column buckling load in regression, fuzzy logic and ann based estimations. *Journal of Intelligent & Fuzzy Systems: Applications in Engineering and Technology*, 26(3):1077–1087, 2014. ISSN 10641246. doi: 10.3233/IFS-120701.

[60] S. Tohidi and Y. Sharifi. A new predictive model for restrained distortional buckling strength of half-through bridge girders using artificial neural network. *KSCE Journal of Civil Engineering*, 20 (4):1392–1403, 2016. ISSN 1226-7988 1976-3808. doi: 10.1007/s12205-015-0176-8.

[61] Y. Sharifi, A. Moghbeli, M. Hosseinpour, and H. Sharifi. Neural networks for lateral torsional buckling strength assessment of cellular steel i-beams. *Advances in Structural Engineering*, 22 (9):2192–2202, 2019. ISSN 1369-4332 2048-4011. doi: 10.1177/1369433219836176.

[62] M. Abambres, K. Rajana, K. Tsavdaridis, and T. Ribeiro. Neural network-based formula for the buckling load prediction of i-section cellular steel beams. *Computers*, 8(1):1–26, 2018. ISSN 2073-431X. doi: 10.3390/computers8010002.

[63] M.R. Sheidaii and R. Bahraminejad. Evaluation of compression member buckling and post-buckling behavior using artificial neural network. *Journal of Constructional Steel Research*, 70: 71–77, 2012. ISSN 0143974X. doi: 10.1016/j.jcsr.2011.10.020.

[64] Y. Pu and E. Mesbahi. Application of artificial neural networks to evaluation of ultimate strength of steel panels. *Engineering Structures*, 28(8):1190–1196, 2006. ISSN 01410296. doi: 10.1016/j.engstruct.2005.12.009.

[65] A. Cevik and I.H. Guzelbey. A soft computing based approach for the prediction of ultimate strength of metal plates in compression. *Engineering Structures*, 29(3):383–394, 2007. ISSN 01410296. doi: 10.1016/j.engstruct.2006.05.005.

[66] T. Subramani and S. Sharmila. Prediction of deflection and stresses of laminated composite plate with artificial neural network aid. *International Journal of Modern Engineering Research (IJMER)*, 4(6):51–58, 2014. ISSN 2249-6645.

[67] M. Sonmez and M.A. Komur. Using fem and artificial networks to predict on elastic buckling load of perforated rectangular plates under linearly varying in-plane normal load. *Structural Engineering and Mechanics*, 34(2):159–174, 2010. ISSN 1225-4568. doi: 10.12989/sem.2010.34.2.159.

[68] Y. Pu, E. Mesbahi, and A.H. Elhewy. Ann-based response surface method and its application to ultimate strength of plates. *Proceedings of the International Offshore and Polar Engineering Conference*, 2005:752–758, 2005.

[69] H. Hasanzadehshooiili, A. Lakirouhani, and A. Šapalas. Neural network prediction of buckling load of steel arch-shells. *Archives of Civil and Mechanical Engineering*, 12(4):477–484, 2012. ISSN 16449665. doi: 10.1016/j.acme.2012.07.005.

[70] E. Mesbahi and Y. Pu. Application of ann-based response surface method to prediction of ultimate strength of stiffened panels. *Journal of Structural Engineering*, 134(10):1649–1656, 2008. ISSN 0733-9445 1943-541X. doi: 10.1061/(asce)0733-9445(2008)134:10(1649).

[71] M.R. Zareei, M.R. Khedmati, and P. Rigo. Application of artificial neural networks to the evaluation of the ultimate strength of uniaxially compressed welded stiffened aluminium plates. *Proceedings of the Institution of Mechanical Engineers, Part M: Journal of Engineering for the Maritime Environment*, 226(3):197–213, 2012. ISSN 1475-0902 2041-3084. doi: 10.1177/1475090212445865.

[72] U.K. Mallela and A. Upadhyay. Buckling load prediction of laminated composite stiffened panels subjected to in-plane shear using artificial neural networks. *Thin-walled Structures*, 102:158–164, 2016.

[73] S. Kumar, R. Kumar, S. Mandal, and A.K. Rahul. The prediction of buckling load of laminated composite hat-stiffened panels under compressive loading by using of neural networks. *The Open Civil Engineering Journal*, 12(1):468–480, 2018. ISSN 1874-1495. doi: 10.2174/1874149501812010468.

[74] Z.R. Tahir and P. Mandal. Artificial neural network prediction of buckling load of thin cylindrical shells under axial compression. *Engineering Structures*, 152:843–855, 2017. ISSN 01410296. doi: 10.1016/j.engstruct.2017.09.016.

[75] L. Liang, M. Liu, C. Martin, and W. Sun. A deep learning approach to estimate stress distribution: a fast and accurate surrogate of finite-element analysis. *J R Soc Interface*, 15(138), 2018. ISSN 1742-5689 1742-5662. doi: 10.1098/rsif.2017.0844.

[76] L. Liang, W. Mao, and W. Sun. A feasibility study of deep learning for predicting hemodynamics of human thoracic aorta. *J Biomech*, 99:109544, 2020. ISSN 1873-2380 (Electronic) 0021-9290 (Linking). doi: 10.1016/j.jbiomech.2019.109544.

[77] Z. Nie, H. Jiang, and L.B. Kara. Stress field prediction in cantilevered structures using convolutional neural networks. *Journal of Computing and Information Science in Engineering*, 20(1):1, 2020. ISSN 1530-9827 1944-7078. doi: 10.1115/1.4044097.

[78] G. Chen, T. Li, Q. Chen, S. Ren, C. Wang, and S. Li. Application of deep learning neural network to identify collision load conditions based on permanent plastic deformation of shell structures. *Computational Mechanics*, 64(2):435–449, 2019. ISSN 0178-7675 1432-0924. doi: 10.1007/s00466-019-01706-2.

[79] S. Ren, G. Chen, T. Li, Q. Chen, and S. Li. A deep learning-based computational algorithm for identifying damage load condition: An artificial intelligence inverse problem solution for failure analysis. *Computer Modeling in Engineering & Sciences*, 117(3):287–307, 2018. ISSN 15261492. doi: 10.31614/cmes.2018.04697.

[80] H. Liu and Y. Zhang. Deep learning-based brace damage detection for concentrically braced frame structures under seismic loadings. *Advances in Structural Engineering*, 22(16):3473–3486, 2019. ISSN 1369-4332 2048-4011. doi: 10.1177/1369433219859389.

[81] H. Liu and Y. Zhang. Image-driven structural steel damage condition assessment method using deep learning algorithm. *Measurement*, 133:168–181, 2019. ISSN 02632241. doi: 10.1016/j.measurement.2018.09.081.

[82] M.G Tharian and C.G Nandakumar. Hat stiffened plates for shipbuilding. *International Journal of Applied Engineering Research and Development (IJAERD)*, 3(1):1–10, 2013. ISSN 2250-1584.

[83] L. Fagerberg. Wrinkling in sandwich panels for marine applications. 2003. ISSN 1651-7660.

[84] T. Von Kármán. *Collected Works of Theodore Von Kármán*. Butterworths Scientific Publications, 1956.

[85] J.K. Paik, A.K. Thayamballi, B.J. Kim, G. Wang, Y.S. Shin, and D. Liu. Ultimate limit state design of ship stiffened panels and grillages. *Society of Naval Architects and Marine Engineers (SNAME)*, 109:221–268, 2001.

[86] DNV GL SE. Rules for classification and construction I. ship technology. Part 1. Chapter 5. structural rules for container ships. 2016.

[87] J.K. Paik and J.K. Seo. Nonlinear finite element method models for ultimate strength analysis of steel stiffened-plate structures under combined biaxial compression and lateral pressure actions—part ii: Stiffened panels. *Thin-Walled Structures*, 47(8):998–1007, 2009. ISSN 0263-8231. doi: https://doi.org/10.1016/j.tws.2008.08.006.

[88] O.F. Hughes and M. Ma. Elastic tripping analysis of asymmetrical stiffeners. *Computers & Structures*, 60(3):369–389, 1996. ISSN 0045-7949. doi: https://doi.org/10.1016/0045-7949(95)00389-4.

[89] K. Pearson and F. Galton. Vii. note on regression and inheritance in the case of two parents. *Proceedings of the Royal Society of London*, 58(347-352):240–242, 1895. doi: doi:10.1098/rspl.1895.0041.

[90] B. Li, P. Cao, D. Zhang, and T. Xu. Experimental research on the stability bearing capacity of q420 high-strength steel tubular members.

[91] Y. Li, Q. Pan, M. Huang, and L. Li. Set-based parametric modeling, buckling and ultimate strength estimation of stiffened ship structures. *Journal of Central South University*, 26(7):1958–1975, 2019. ISSN 2227-5223. doi: 10.1007/s11771-019-4145-0.

[92] S. Zhang and I. Khan. Buckling and ultimate capability of plates and stiffened panels in axial compression. *Marine Structures*, 22(4):791–808, 2009. ISSN 0951-8339. doi: https://doi.org/10.1016/j.marstruc.2009.09.001.

[93] D. Faulkner. A review of effective plating for use in the analysis of stiffened plating in bending and compression. *Journal of Ship Research*, 19(01):1–17, 1975. ISSN 0022-4502.

[94] S. Mo, Y. Zhu, N. Zabaras, X. Shi, and J. Wu. Deep convolutional encoder-decoder networks for uncertainty quantification of dynamic multiphase flow in heterogeneous media. *Water Resources Research*, 55(1):703–728, 2019. ISSN 0043-1397. doi: 10.1029/2018wr023528.

[95] I. Funke, S. Bodenstedt, F. Oehme, F. von Bechtolsheim, J. Weitz, and S. Speidel. Using 3D convolutional neural networks to learn spatiotemporal features for automatic surgical gesture recognition in video. In Dinggang Shen, Tianming Liu, Terry M. Peters, Lawrence H. Staib, Caroline Essert, Sean Zhou, Pew-Thian Yap, and Ali Khan, editors, *Medical Image Computing and Computer Assisted Intervention – MICCAI 2019*, pages 467–475. Springer International Publishing. ISBN 978-3-030-32254-0.

[96] M. Puheim and L. Madarász. Normalization of inputs and outputs of neural network based robotic arm controller in role of inverse kinematic model. In *SAMI 2014 - IEEE 12th International Symposium on Applied Machine Intelligence and Informatics, Proceedings*. doi: 10.1109/SAMI.2014.6822439.

[97] K. Simonyan and A. Zisserman. Very deep convolutional networks for large-scale image recognition. *arXiv 1409.1556*, 2014.

[98] S. Loffe and C. Szegedy. Batch normalization: accelerating deep network training by reducing internal covariate shift. *Proceedings of the 32nd International Conference on International Conference on Machine Learning - Volume 37*, page 448–456, 2015.

[99] D. Choi, C. Shallue, Z. Nado, J. Lee, C. Maddison, and G. Dahl. On empirical comparisons of optimizers for deep learning. *arXiv 1910.05446*, 2019.

[100] K. He, X. Zhang, S. Ren, and J. Sun. Deep residual learning for image recognition. In *2016 IEEE Conference on Computer Vision and Pattern Recognition (CVPR)*, pages 770–778. ISBN 1063-6919. doi: 10.1109/CVPR.2016.90.

[101] J. Hu, L. Shen, G. Sun, and S. Albanie. Squeeze-and-excitation networks. *IEEE Transactions on Pattern Analysis and Machine Intelligence*, PP, 2017. doi: 10.1109/TPAMI.2019.2913372.

[102] E. Rezende, G. Ruppert, A. Theophilo, and T. Carvalho. Exposing computer generated images by using deep convolutional neural networks. *Signal Processing: Image Communication*, 2017. doi: 10.1016/j.image.2018.04.006.

# A

# Geometrical Parameter Set

This appendix contains more detailed information on the geometrical parameter set obtained by the analytical model and the different datasets developed as input for the Machine Learning (ML) model.

Figure A.1 contains the correlation plots which is described in section 5.6.3 and is displayed on the next page. The stiffened panel geometry in this research contains six variable values. In this study, the Pearson Correlation Coefficient (PCC) is used to see if a linear trend can be observed between parameters. Value of -1 and +1 show a strong negative and positive linear correlation, respectively, while values close to 0 implies no or a weak correlation. The entire obtained dataset consists of two groups of which one is a small group located at the limits obtained from classifications societies. This group was not taken into account for making the correlation plot to obtain accurate standard deviations for the PCC. For the same reason, outliers are filtered. It can be observed that most of the parameters show some (>0.6) to a strong (>0.85)correlation. The parameters that show less correlation are still decently grouped. The correlations of the number of stiffeners ($n_s$) are not representative since this can only be an integer.

The histograms displayed in fig. A.2 show the geometrical parameter distributions of the entire data set of 9207 models, which is obtained after applying noise to the genetic algorithm generated data. Only the variable geometrical parameters are shown. The figures make clear that the spread in the individual parameters is significant. The figures make clear that most models prefer a thin plate thickness ($t_p$). For the used length and width of the stiffened panel, it is clear that there is a preference for large stiffeners, as seen from the distribution of the web height ($h_w$). Then web thickness ($t_w$) utilizes only the lower part of the parameters, while the thickness of the flange ($t_f$) spans the entire possible parameter range. The width of the flange ($b_f$) is also widely spread.

This dataset is then used to obtain the training and validation dataset. These sets are sampled such that they maintain the same distributions as the original set. In total, 7355 models are used for training data, and the other 1893 models are used as validation data. Their distributions are displayed over the distributions of the total set in fig. A.3.

A test set is obtained by again adding noise to the genetic algorithm obtained data. In total, 1782 new models are created, and it is verified that none of the models is equal to the training or validation data. The distributions of the test data are plotted in fig. A.4. Their distribution is similar to the original data set.

From the test set, 288 models are selected that will be used for the scalability and the generalizability test. The distribution is displayed in fig. A.5. The bin size is different to show the distributions better because the number of models is small. The set is small because the set is used repetitively for scalability and generalizability tests. With the repetitive use of the 288 models, a scalability set is developed of 7200 models. The same principle is used for the generalizability and a set of 1440 models is obtained.

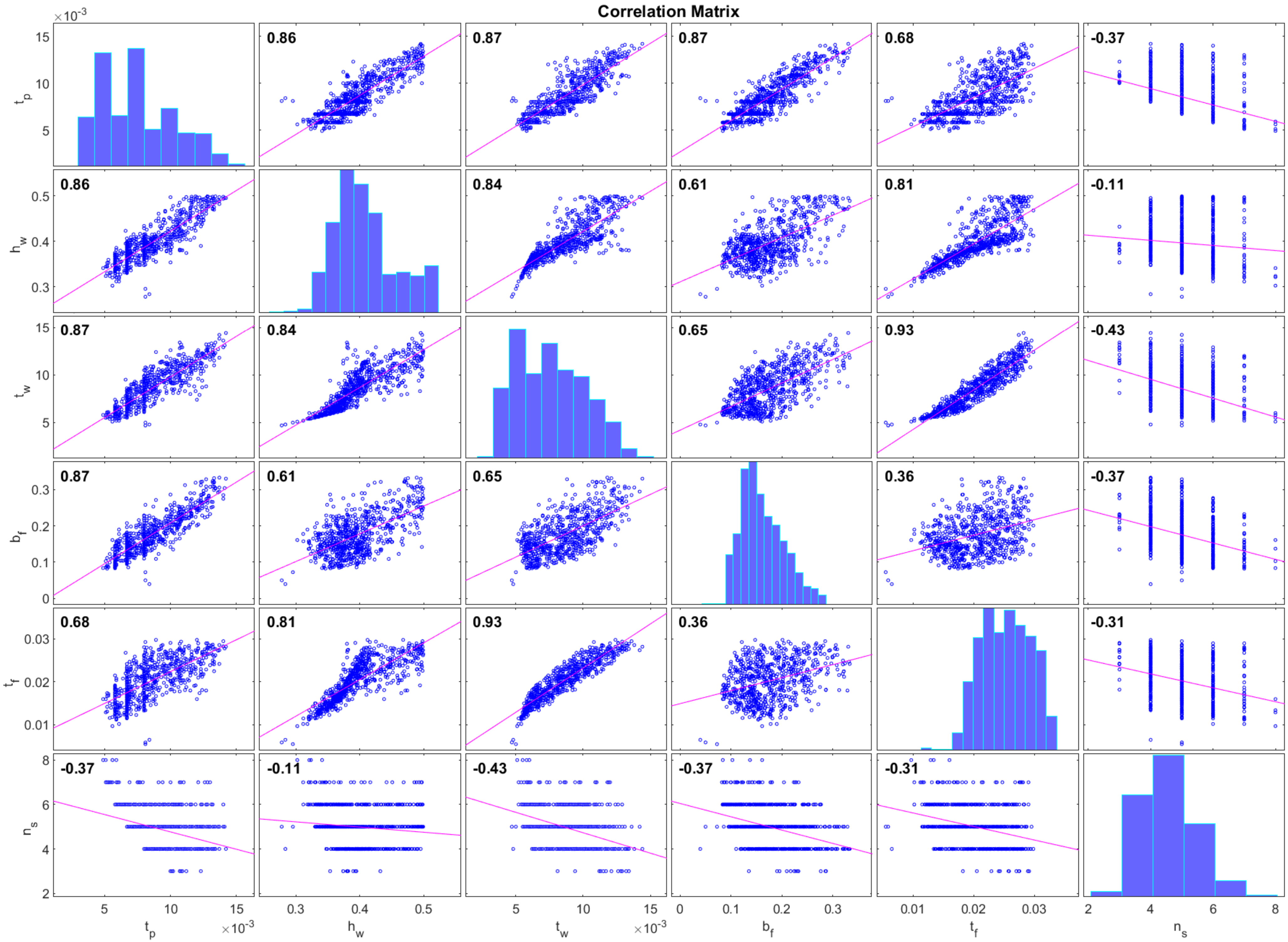
Correlation Matrix
×10^-3
t_p
h_w
t_w
b_f
t_f
n_s
15
10
5
0.5
0.4
0.3
0.3
0.2
0.1
0
0.03
0.02
0.01
8
6
4
2
0.86
0.87
0.87
0.68
-0.37
0.86
0.84
0.61
0.81
-0.11
0.87
0.84
0.65
0.93
-0.43
0.87
0.61
0.65
0.36
-0.37
0.68
0.81
0.93
0.36
-0.31
-0.37
-0.11
-0.43
-0.37
-0.31
5
10
15
×10^-3
0.3
0.4
0.5
5
10
15
×10^-3
0
0.1
0.2
0.3
0.01
0.02
0.03
2
4
6
8

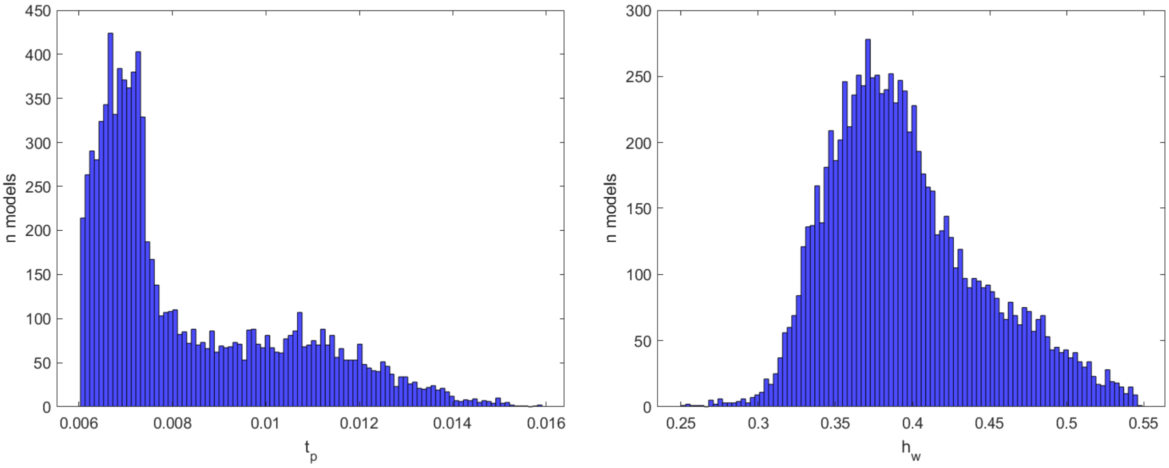

(a) Distribution of the bottom plate thickness which is used as dataset for the machine learning.

(b) Distribution of the height of the web which is used as dataset for the machine learning.

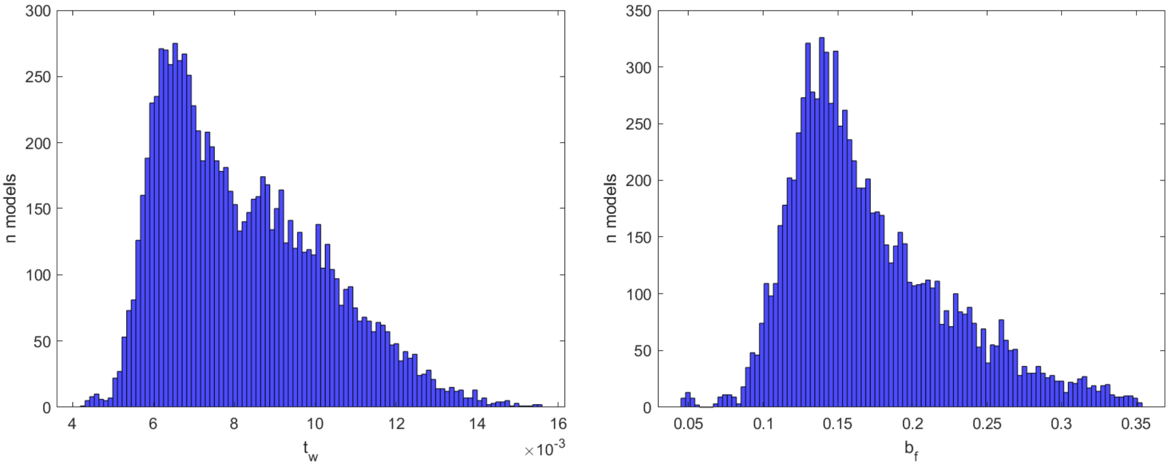

(c) Distribution of the thickness of the web which is used as dataset for the machine learning.

(d) Distribution of the width of the flange which is used as dataset for the machine learning.

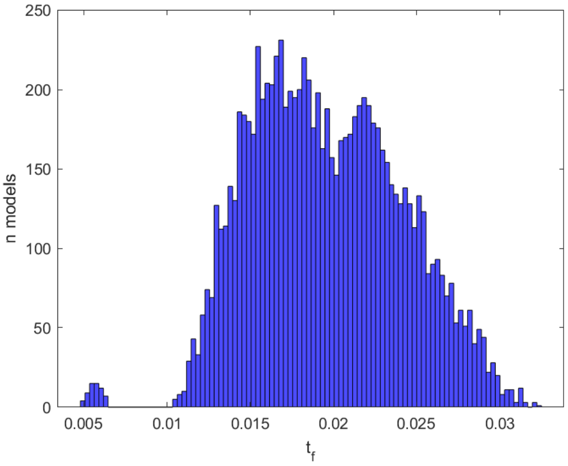

(e) Distribution of the thickness of the flange which is used as dataset for the machine learning.

Figure A.2: Distributions of the geometrical parameters of the dataset of 9207 models. This dataset forms the input data set for the machine learning model. A wide spread of every single geometrical parameter can be observed.

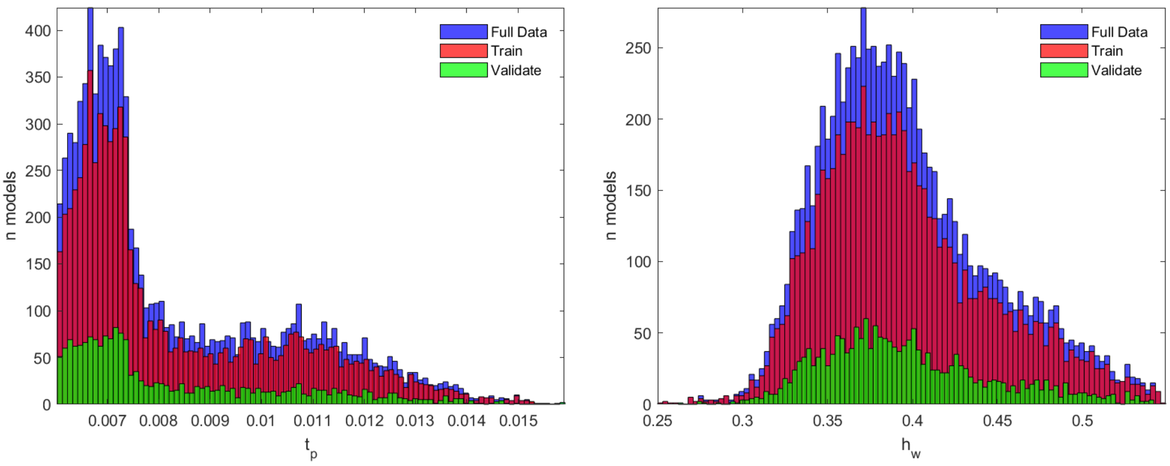

(a) Distribution of the bottom plate thickness which is used as dataset for the machine learning. Besides the original dataset, also the train and validation set is plotted.

(b) Distribution of the height of the web which is used as dataset for the machine learning. Besides the original dataset, also the train and validation set is plotted.

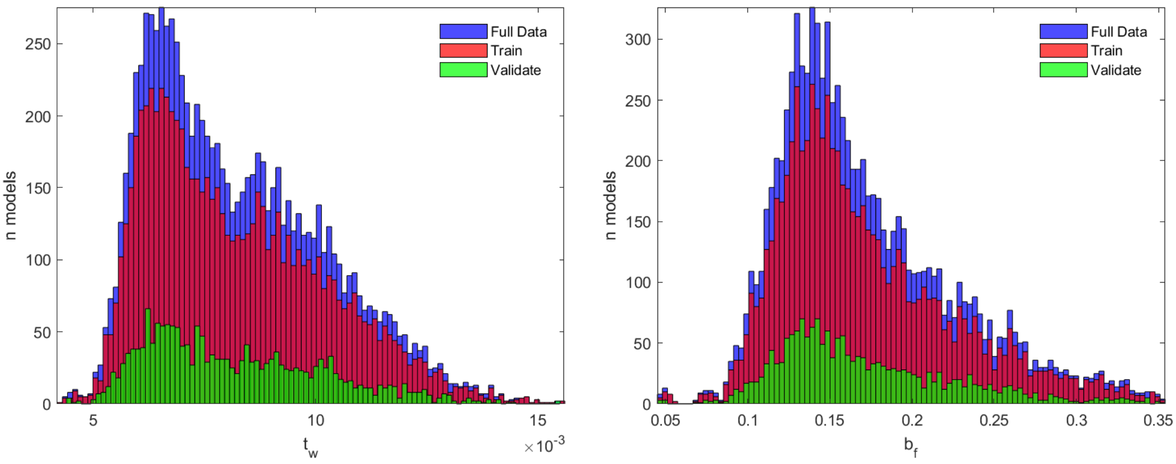

(c) Distribution of the thickness of the web which is used as dataset for the machine learning. Besides the original dataset, also the train and validation set is plotted.

(d) Distribution of the width of the flange which is used as dataset for the machine learning. Besides the original dataset, also the train and validation set is plotted.

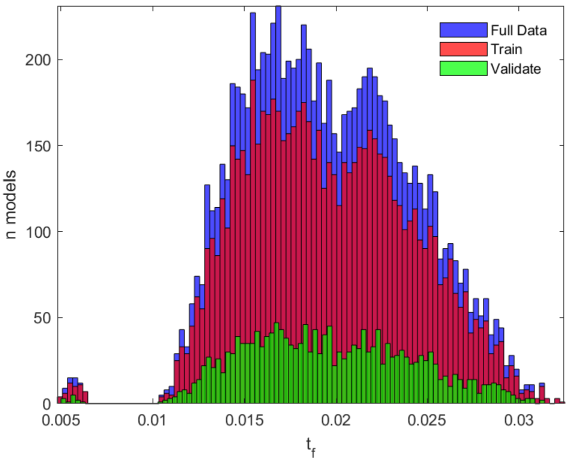

(e) Distribution of the thickness of the flange which is used as dataset for the machine learning. Besides the original dataset, also the train and validation set is plotted.

Figure A.3: Distributions of the geometrical parameters of the dataset of 9207 models. The training set contains 80% of the models which are 7355 models. The validation set contains 20% of the models which are 1893 models. The training and validation dataset forms the input data set for the machine learning model to train and validate the the training process. A wide spread of every single geometrical parameter can be observed.

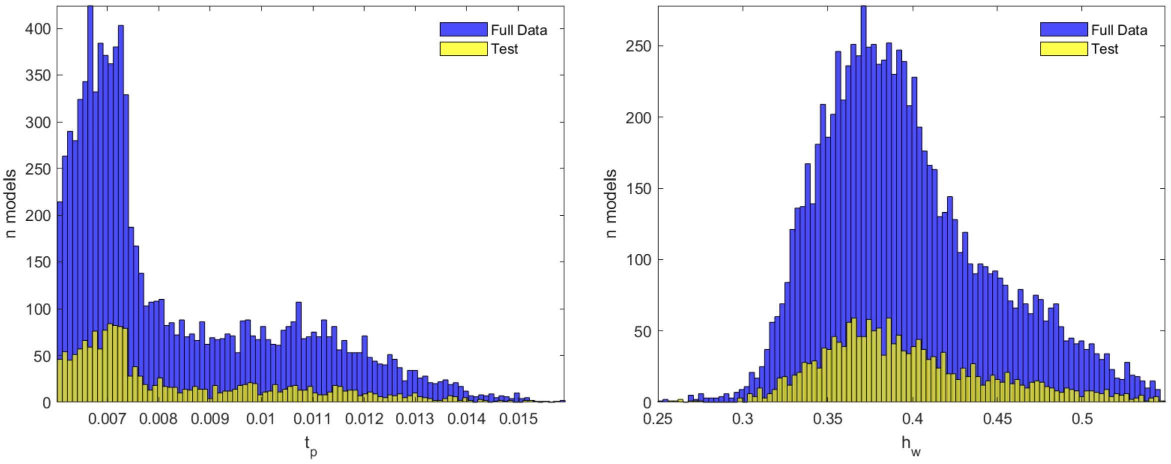

(a) Distribution of the bottom plate thickness which is used as dataset for the machine learning. Besides the original dataset, also the test set is plotted.

(b) Distribution of the height of the web which is used as dataset for the machine learning. Besides the original dataset, also the test set is plotted.

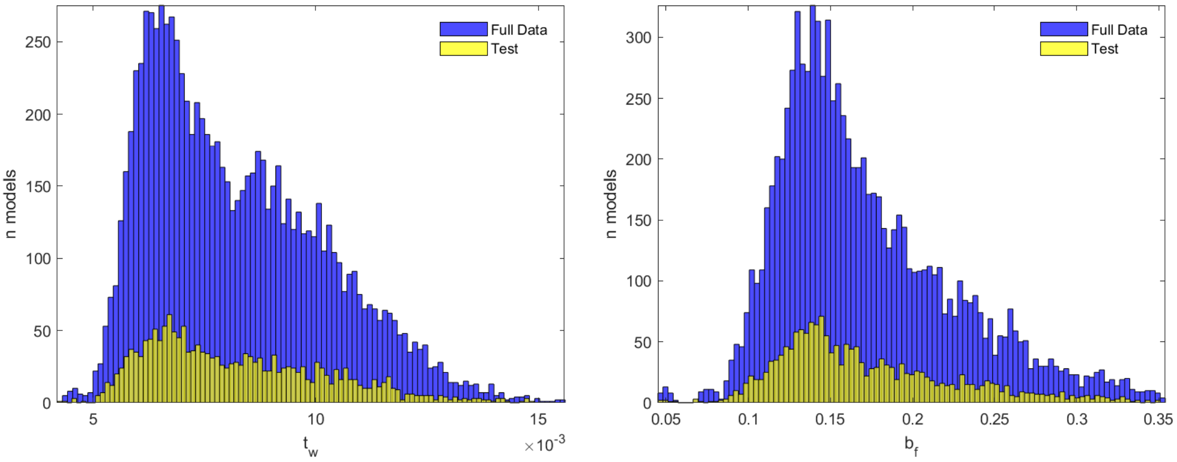

(c) Distribution of the thickness of the web which is used as dataset for the machine learning. Besides the original dataset, also the test set is plotted.

(d) Distribution of the width of the flange which is used as dataset for the machine learning. Besides the original dataset, also the test set is plotted.

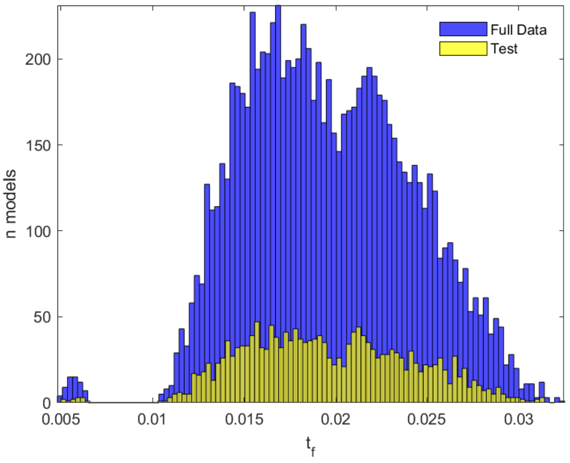

(e) Distribution of the thickness of the flange which is used as dataset for the machine learning. Besides the original dataset, also the test set is plotted.

Figure A.4: Distributions of the geometrical parameters of the dataset of 9207 models. The test set is a new generated set of models which contains 1782 models. This dataset forms the test input data set for the machine learning model. A wide spread of every single geometrical parameter can be observed.

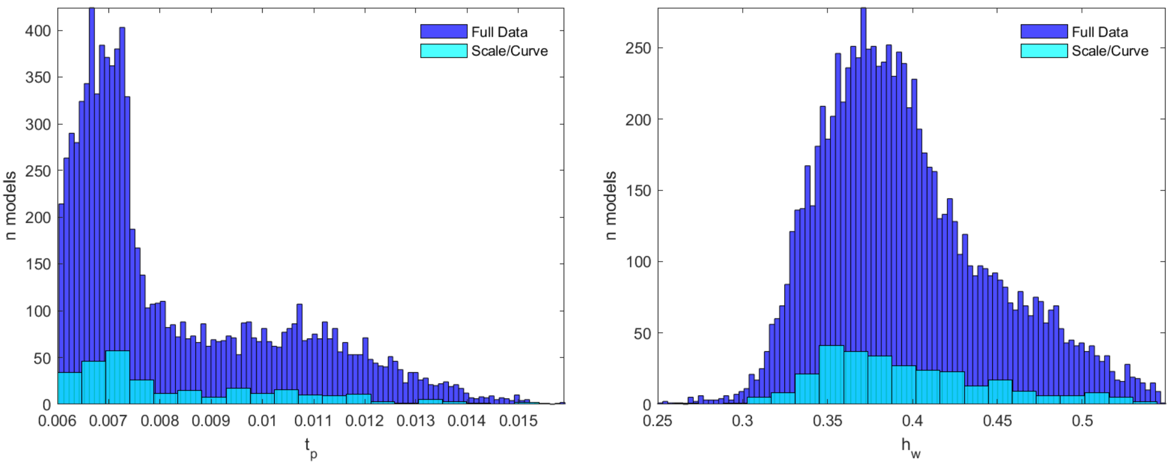

(a) Distribution of the bottom plate thickness which is used as dataset for the machine learning. Besides the original dataset, also the dataset for the scalability and generalizability is plotted.

(b) Distribution of the height of the web which is used as dataset for the machine learning. Besides the original dataset, also the dataset for the scalability and generalizability is plotted.

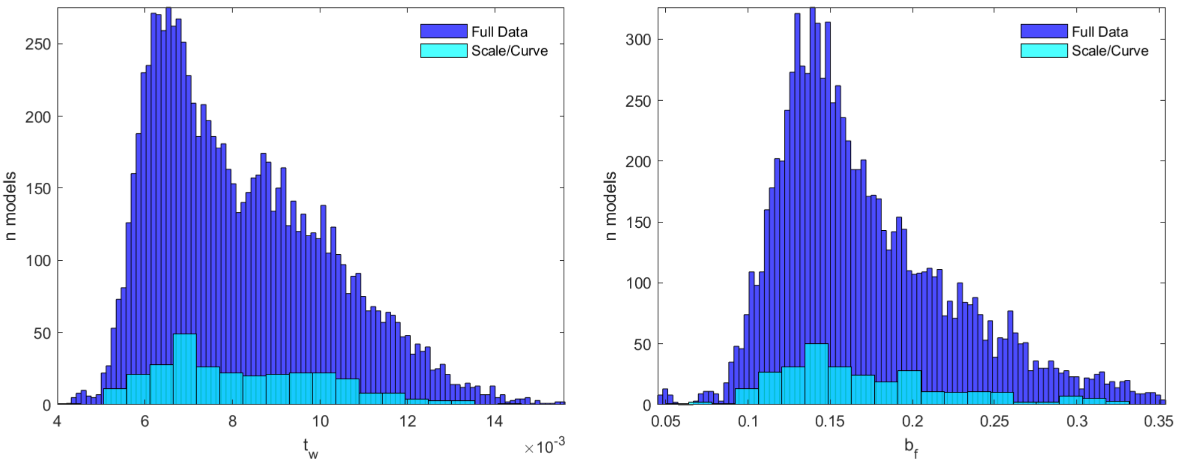

(c) Distribution of the thickness of the web which is used as dataset for the machine learning. Besides the original dataset, also the dataset for the scalability and generalizability is plotted.

(d) Distribution of the width of the flange which is used as dataset for the machine learning. Besides the original dataset, also the dataset for the scalability and generalizability is plotted.

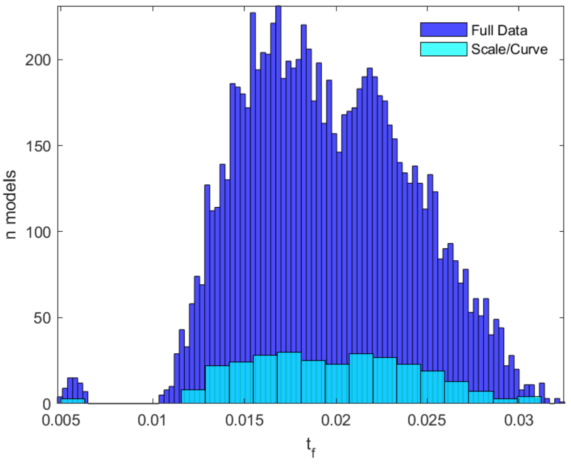

(e) Distribution of the thickness of the flange which is used as dataset for the machine learning. Besides the original dataset, also the dataset for the scalability and generalizability is plotted.

Figure A.5: Distributions of the geometrical parameters of the dataset of 9207 models. This set is the small dataset drawn from the original dataset which will repetitively be used for testing the scalability and the generalizability. This set contains 288 individual models but will be extended to 7200 models for scalability and 1440 models for generalizability. The bin size of the 288 models is larger to show the distribution for this small dataset.

# B

# Scalability Stress Distribution

A set of 288 structural models is selected from the training set. From those 288 models, every single parameter is increased in steps of 5% to see how well the developed ML model can predict results outside the training range. There are five variables in the geometry that are increased with a maximum of 25%. This will result in a scalability test set of 7200 models.

The error on all the individual models is obtained to test the performance of the developed ML models. A curve of the mean MSE error is obtained. Error bars are added to this mean error curve that represents the Standard Error (SE), which can be determined by making use of eq. (B.1). The SE is determined by dividing the standard deviation ($\sigma_{std}$) by the square root of the number of data points. The reason for plotting the SE instead of the standard deviation is, that every 288 models will result in equal number means which will be used to obtain an average mean of all 288 models. The error bars then represent the variability of the plotted mean. Also, it became clear that the spread of the individual results is significant, causing a large standard deviation that is not well presentable. Therefore, box plots of the individual datasets are made to show the distribution and spread of the predicted results. Box plots are also based on the median value instead of the mean, which provides some information on the distribution.

This appendix shows the scalability results for the individual predicted stress components, the corresponding von Mises stress, the directly predicted von Mises stress distribution, and results of the ultimate strength prediction. All figures also show the corresponding test van validation error.

$$SE = \frac{\sigma_{std}}{\sqrt{n_d}} \tag{B.1}$$

Figure B.1 shows the results for the stress distribution in x- and y-direction ($\sigma_x$ and $\sigma_y$). The line plots fig. B.1a and fig. B.1b show an significant increase in the mean error when increasing the plate thickness ($t_p$) and the height of the web ($h_w$). The error increases slightly when increasing the width of the flange ($b_f$). The thickness of the web ($t_w$) and flange ($t_f$) do not significantly influence the error. The mean error seems even to decrease when increasing the thickness of the web. Figure B.1c and fig. B.1d show the corresponding box plots. Every box shows the results for 288 models that belong to a specific increase of a single parameter. From the box plots, similar conclusions can be drawn compared to the line plots. The box plot also makes the spread of the results clear. Since the median is used instead of the mean, an increase can be observed when increasing $b_f$. The figures also show a substantial number of outliers. These are not specifically outliers in these results, but they are beyond the 1.5 interquartile range of the box plot whiskers and are therefore drawn as outliers. The large number of outliers makes clear that there is a large spread in the obtained results.

Similar results are shown for the different individual stress components. Figure B.2 shows the results for the stress in z-direction ($\sigma_z$) and the shear in the xy-plane ($\tau_{xy}$). Figure B.2a and B.2b show the line plots with similar results. Figure B.2c and fig. B.2d show the corresponding box plots. The obtained results show similar results compared to the stresses in x- and y-direction. Figure B.3 shows the results for the shear in yz- and zx-plane ($\tau_{yz}$ and $\tau_{zx}$). Figure B.3a and fig. B.3b show the line plots. Figure B.3c and fig. B.3d show the corresponding box plots. Similar results are obtained compared to all other graphs. The increase in error for $\tau_{yz}$ shows a similar increase in behavior, but the magnitude of the increase is significantly smaller. Figure B.4 shows the results for the directly predicted von Mises stress, the von Mises determined from the individual stress components and the ultimate strength results. Figure 8.6a and fig. 8.6b show the line plots of Figure B.4a and fig. B.4b, respectively. The graphs show similar results to the individual stress components. Figure B.4c show the ultimate strength box plots belonging to fig. 7.6.

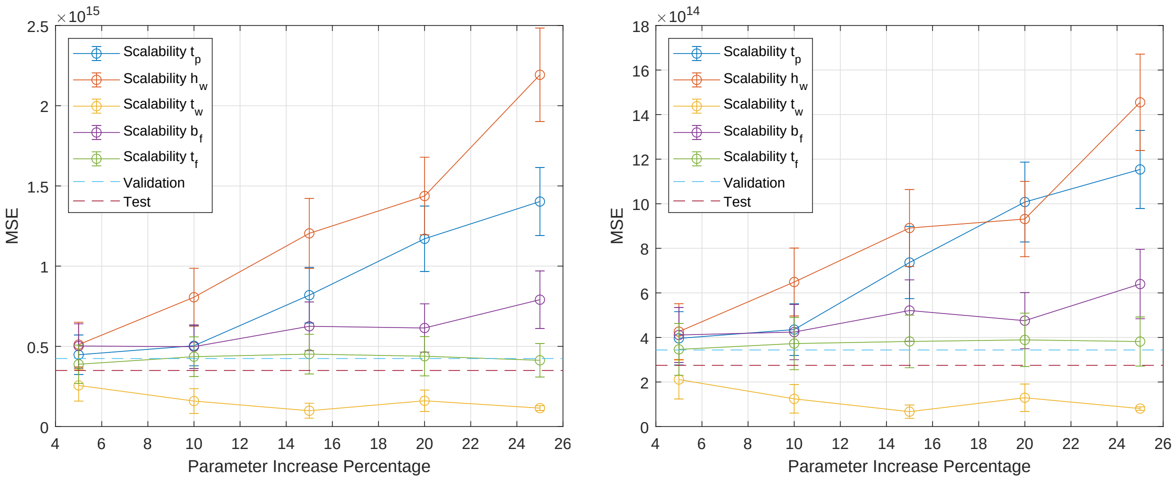

(a) Stress in x-direction ($\sigma_x$) MSE plot of the model developed to predict the individual stress distributions at the moment of failure. The errorbars represent the SE. It can be observed that there is a strong increase in error by increasing $t_p$ and $h_w$. A minor increase is obser ved for the increase of $b_f$. The influence of $t_w$ and $t_f$ is limited. The SE of the mean becomes larger by increasing the individual parameters except for $t_w$.

(b) Stress in y-direction ($\sigma_y$) MSE plot of the model developed to predict the individual stress distributions at the moment of failure. The errorbars represent the SE. It can be observed that there is a strong increase in error by increasing $t_p$ and $h_w$. A minor increase is obser ved for the increase of $b_f$. The influence of $t_w$ and $t_f$ is limited. The SE of the mean becomes larger by increasing the individual parameters except for $t_w$.

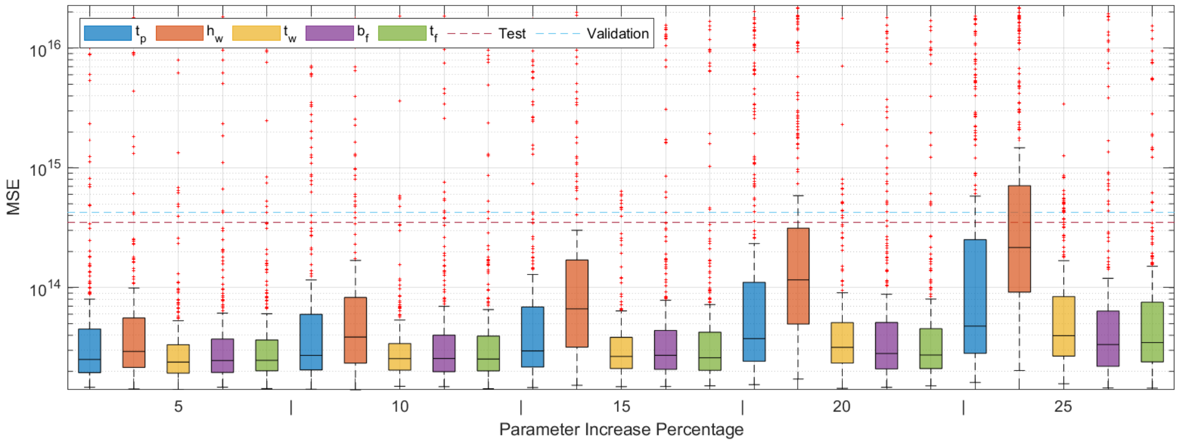

(c) MSE box plot corresponding to fig. B.1a. The boxes make clear that the spread and median becomes larger by increasing the parameters. Different to the mean, the median of $t_w$ shows an increase by increasing the parameters. It again becomes clear that error on $t_p$ and $h_w$ are the most influenced by the increase of parameters. The large number of outliers shows that the data contains predictions with significantly larger errors.

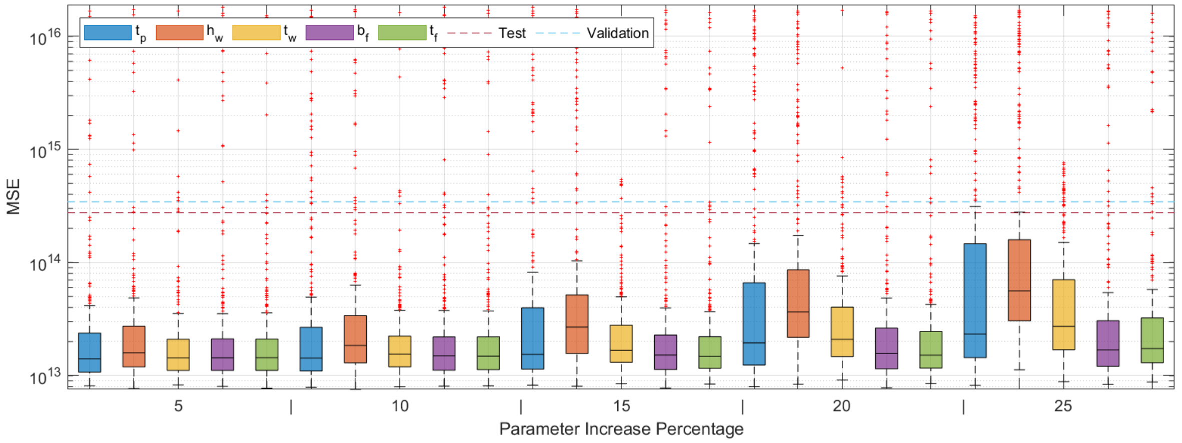

(d) MSE Box plot corresponding to fig. B.1b. The boxes make clear that the spread and median becomes larger for $t_p$, $h_w$, and $t_w$. The increase in spread and median of $b_f$ and $t_f$ remains limited. Different to the mean, the median of $t_w$ shows an increase by increasing the parameters. Also, different to fig. B.1b, the median of $t_p$ is never higher than the median of $h_w$.

Figure B.1: Scalability results of $\sigma_x$ and $\sigma_y$ determined by the model developed to predict the individual stress distribution at the moment of failure. (a) shows a line plot of the mean error on $\sigma_x$ by increasing the individual parameters. (b) shows a line plot of the mean error on $\sigma_y$ by increasing the individual parameters. Both line plots also display the Standard Error (SE). (c) shows box plots of the mean error on $\sigma_x$. (d) shows box plots of the mean error on $\sigma_y$. Every box corresponds to a dataset of 288 models with a total of 7200 models.

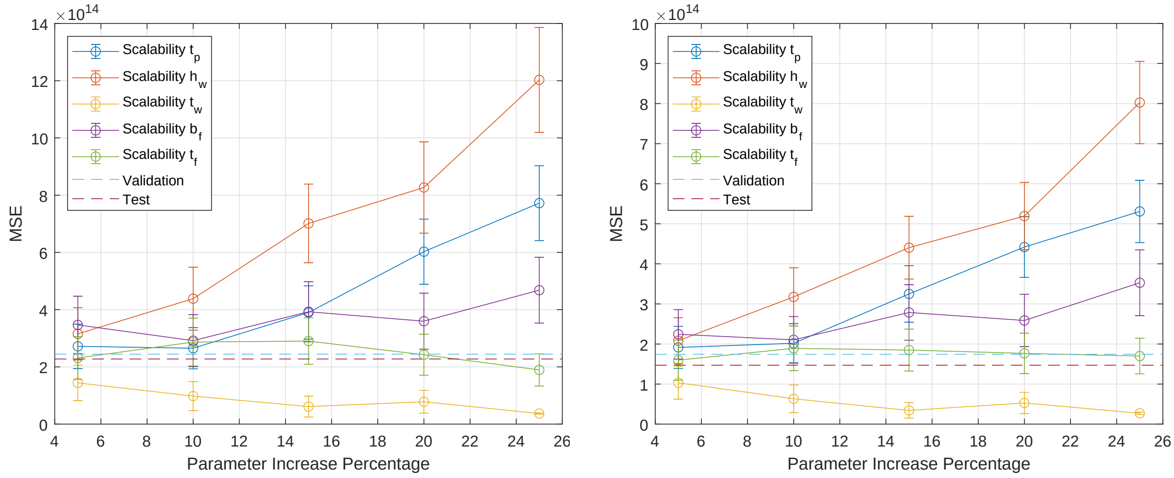

(a) Stress in z-direction ($\sigma_z$) MSE plot of the model developed to predict the individual stress distributions at the moment of failure. The errorbars represent the SE. It can be observed that there is a strong increase in error by increasing $t_p$ and $h_w$. A minor increase is observer for the increase of $b_f$. The influence of $t_w$ and $t_f$ is limited. The SE of the mean becomes larger by increasing the individual parameters except for $t_w$.

(b) Shear in the xy-plane ($\tau_{xy}$) MSE plot of the model developed to predict the individual stress distributions at the moment of failure. The errorbars represent the SE. It can be observed that there is a strong increase in error by increasing $t_p$ and $h_w$. A minor increase is observer for the increase of $b_f$. The influence of $t_w$ and $t_f$ is limited. The SE of the mean becomes larger by increasing the individual parameters except for $t_w$.

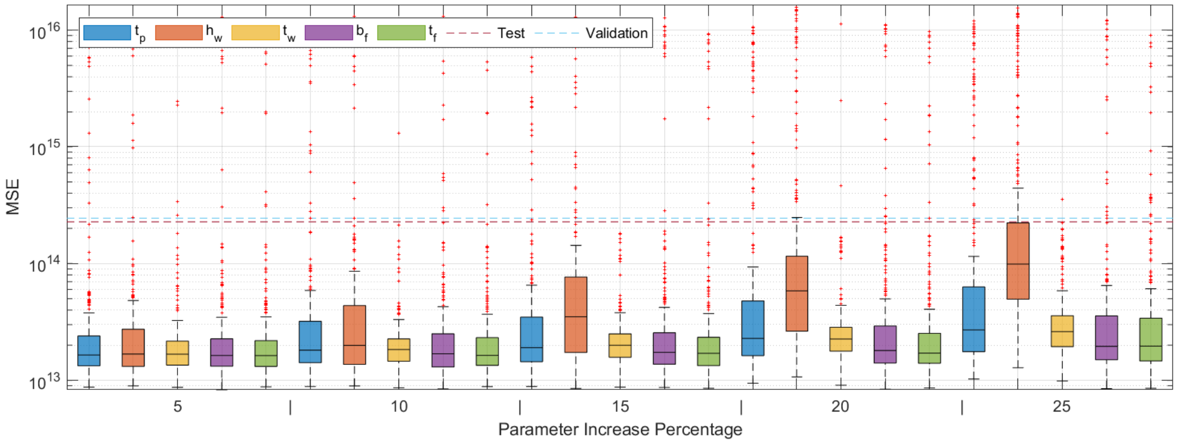

(c) MSE Box plot corresponding to fig. B.2a. The boxes make clear that the spread and median becomes larger by increasing the parameters. Different to the mean, the median of $t_w$ shows an increase by increasing the parameters. The box moves to a larger error by increasing $t_w$ with little increase in spread. It again becomes clear that error on $t_p$ and $h_w$ are the most influenced by the increase of parameters. The large number of outliers show that the data contains predictions with significantly larger errors.

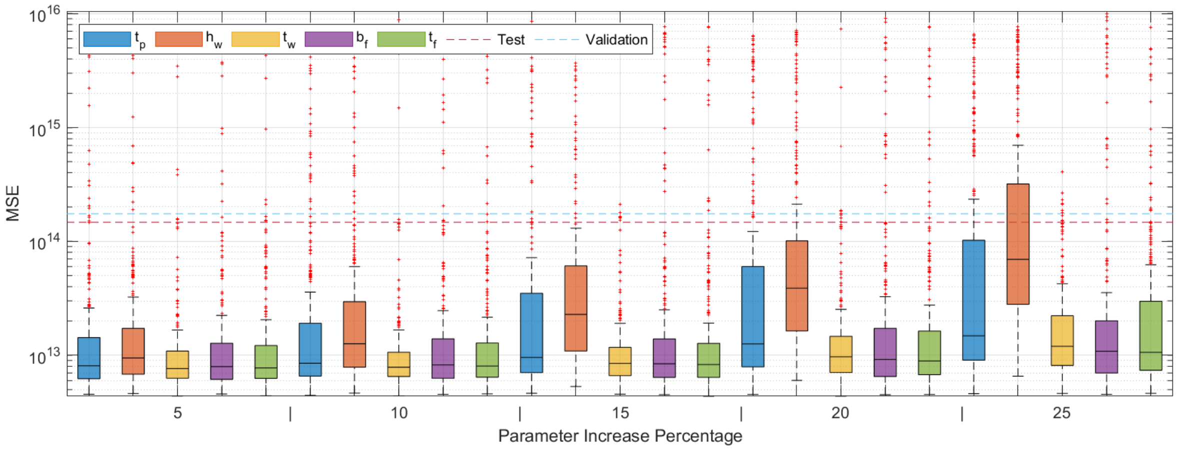

(d) MSE Box plot corresponding to fig. B.2b. The boxes make clear that the spread and median becomes larger by increasing the parameters. Different to the mean, the median of $t_w$ shows an increase by increasing the parameters. It again becomes clear that error on $t_p$ and $h_w$ are the most influenced by the increase of parameters. The large number of outliers show that the data contains predictions with significantly larger errors.

Figure B.2: Scalability results of $\sigma_z$ and $\tau_{xy}$ determined by the model developed to predict the individual stress distribution at the moment of failure. (a) shows a line plot of the mean error on $\sigma_z$ by increasing the individual parameters. (b) shows a line plot of the mean error on $\tau_{xy}$ by increasing the individual parameters. Both line plots also display the Standard Error (SE). (c) shows box plots of the mean error on $\sigma_z$. (d) shows box plots of the mean error on $\tau_{xy}$. Every box corresponds to a dataset of 288 models with a total of 7200 models.

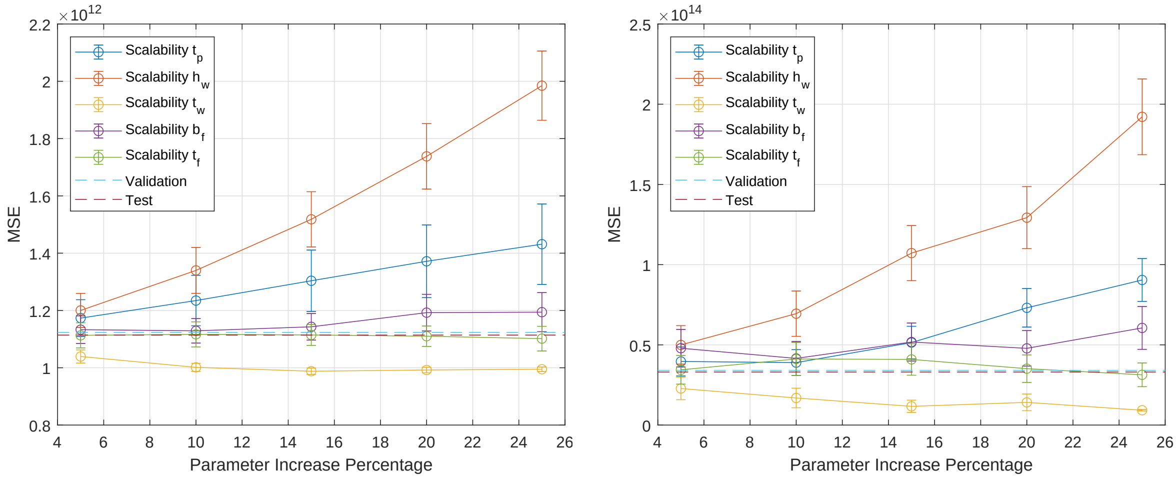

(a) Shear in the yz-plane ($\tau_{yz}$) MSE plot of the model developed to predict the individual stress distributions at the moment of failure. The errorbars represent the SE. It can be observed that there is an increase in error by increasing $t_p$ and $h_w$. The influence of $t_w$, $b_f$ and $t_f$ is limited. The SE of the mean becomes larger by increasing the individual parameters except for $t_w$. The increase of error is less significant compared to other stress factors.

(b) Shear in the zx-plane ($\tau_{zx}$) MSE plot of the model developed to predict the individual stress distributions at the moment of failure. The errorbars represent the SE. It can be observed that there is a strong increase in error by increasing $h_w$. A minor increase is observer for the increase of $t_p$ and $b_f$. The influence of $t_w$ and $t_f$ is limited. The SE of the mean becomes larger by increasing the individual parameters except for $t_w$.

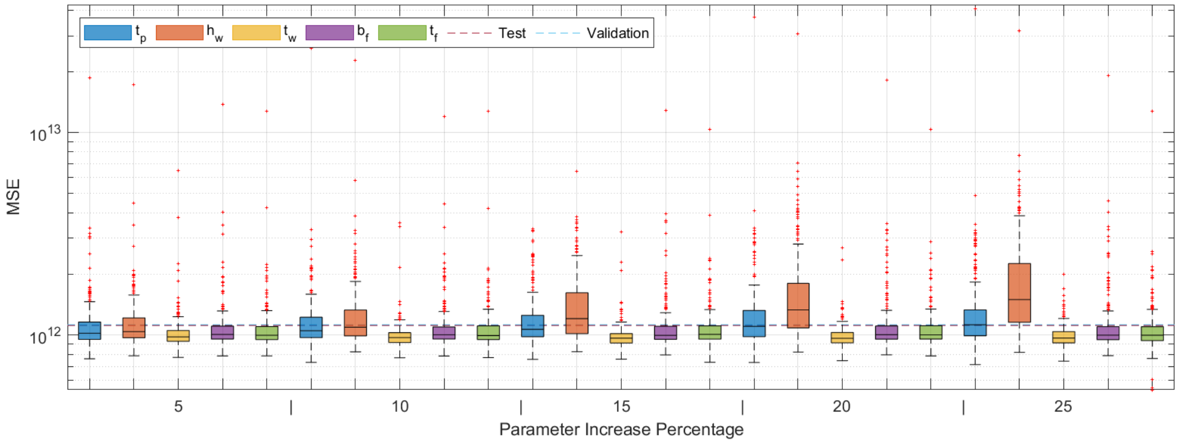

(c) MSE Box plot corresponding to fig. B.3a. The boxes make clear that the spread and median becomes larger by increasing $t_p$ and $h_w$. All other parameters show little influence on the obtained error, the spread and the median. It again becomes clear that error on $t_p$ and $h_w$ are the most influenced by the increase of parameters. The large number of outliers show that the data contains predictions with significantly larger errors, although the outliers are less extreme compared to other stress components

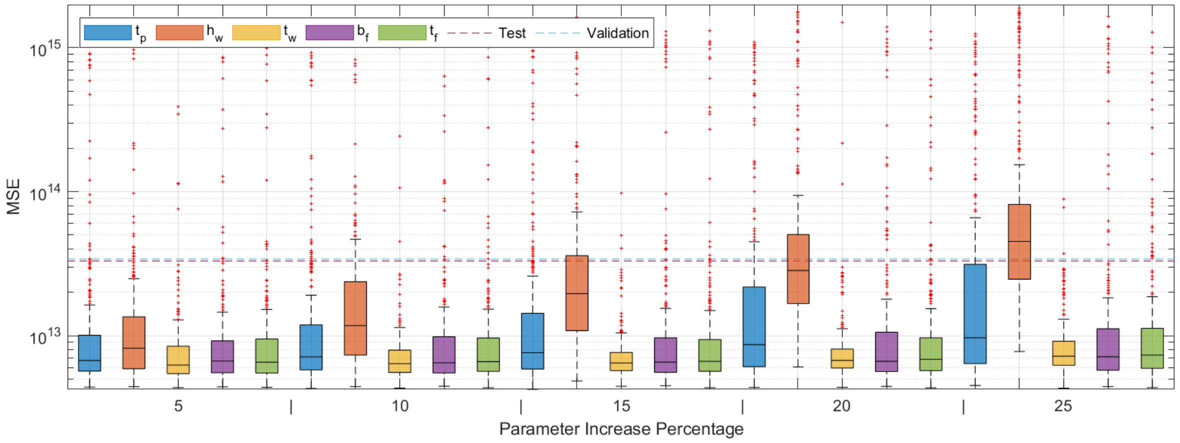

(d) MSE Box plot corresponding to fig. B.3b. The boxes make clear that the spread and median becomes larger by increasing the parameters. Different to the mean, the median of $t_w$ shows an increase by increasing the parameters. It again becomes clear that error on $t_p$ and $h_w$ are the most influenced by the increase of parameters. The large number of outliers show that the data contains predictions with significantly larger errors.

Figure B.3: Scalability results of $\tau_{yz}$ and $\tau_{zy}$ determined by the model developed to predict the individual stress distribution at the moment of failure. (a) shows a line plot of the mean error on $\tau_{yz}$ by increasing the individual parameters. (b) shows a line plot of the mean error on $\tau_{zx}$ by increasing the individual parameters. Both line plots also display the Standard Error (SE). (c) shows box plots of the mean error on $\tau_{yz}$. (d) shows box plots of the mean error on $\tau_{zx}$. Every box corresponds to a dataset of 288 models with a total of 7200 models.

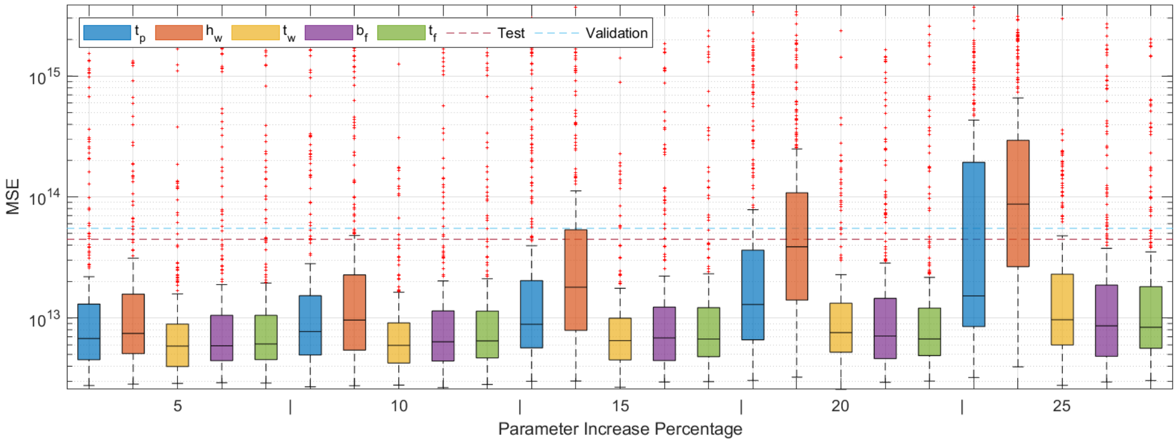

(a) MSE Box plot corresponding to fig. 8.6a. The boxes make clear that the spread and median becomes larger by increasing $t_p$ and $h_w$. All other parameters show little influence on the obtained error, the spread and the median. It again becomes clear that error on $t_p$ and $h_w$ are the most influenced by the increase of parameters. The large number of outliers show that the data contains predictions with significantly larger errors, although the outliers are less extreme compared to other stress components

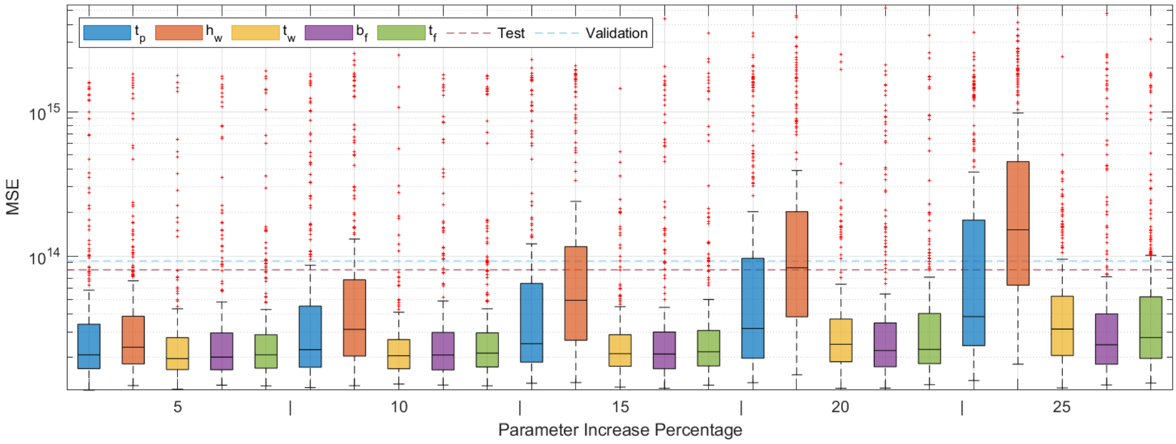

(b) MSE Box plot corresponding to fig. 8.6b. The boxes make clear that the spread and median becomes larger by increasing the parameters. The behaviour is similar to the results obtained from the individual stress components. This is due to the fact that these stresses will be used to determine the von Mises stress.

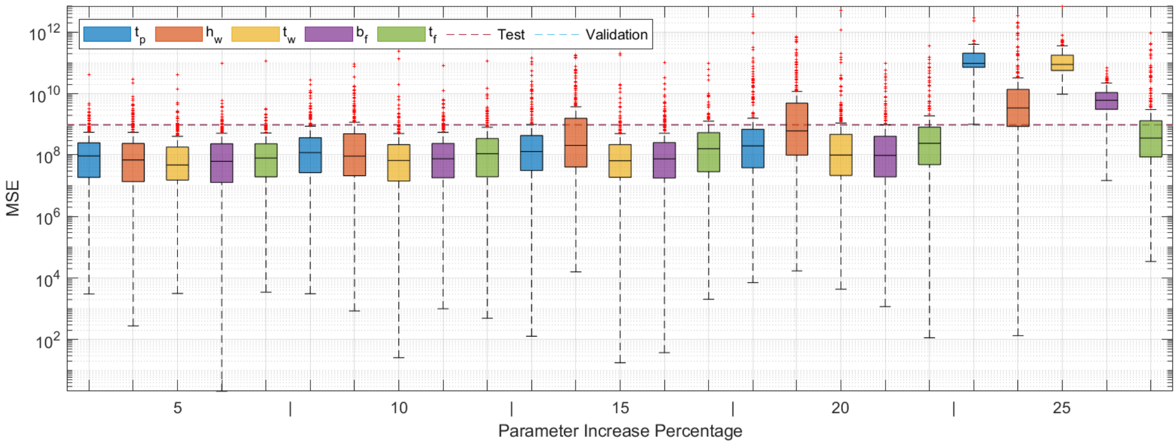

(c) MSE Box plot corresponding to fig. 7.6. The boxes make clear that the spread and median becomes larger by increasing the parameters. An increasing trend can be observed when increasing the individual parameters. Also, more outliers are present with an increase in parameters. A significant increase in MSE is observed at a 25% increase.

Figure B.4: Scalability results of both von Mises stresses, the directly predicted von Mises stress and the von Mises determined by the individual stress distribution at the moment of failure. Also, the scalability results of the ultimate strengh predicting model are displayed. (a) shows box plots of the individual mean errors on the directly predicted von Mises stress. (b) shows box plots of the individual mean errors on the von Mises determined from the individual stress components. (c) shows the box plots of the ultimate strength predictions. Every box corresponds to a dataset of 288 models with a total of 7200 models.

# C

# Generalizability Stress Distribution

The dataset used to examine the generalizability consists of 1440 curved stiffened panel models based on 288 base models that are also used for the scalability data set. In total, five different curvatures have been tested. Instead of defining a fixed radius of curvature, a fixed height in the middle of the stiffened panel is used. This height is increased in steps of 0.2 meter until a height of 1.0 meter is reached in the middle of the panel. For the generalizability, the stiffened panels are only curved in one direction, which is the transverse direction. This direction of curvature is a commonly used shape in the bilge of ships. The stiffened panels are curved such that the stiffeners point towards the center of curvature as is described in section 7.7.

This appendix displays box plots for the individual stress components, the von Mises stress determined from these individual stress components, and the directly predicted von Mises stress. All plots also show the Mean Squared Error (MSE) obtained on the corresponding validation and test set.

Figure C.1a shows the MSE for the stress in x-direction ($\sigma_x$). The graph shows a clear increase in the median and the spread of the error when the curvature of the stiffened panels increases. Figure C.1b and fig. C.1c show the MSE of the stress in y- and z-direction respectively ($\sigma_y$ and $\sigma_z$). Both graphs show that an increase in curvature will not result in an increase in the obtained loss. It is interesting to observe that the largest spread in the predictions is observed for the stiffened panels with the smallest curvature that has been tested. Similar behaviour can be observed for the shear stress in the xy-plane ($\tau_{xy}$) . This behaviour is different compared to the results in x-direction. Figure C.1e shows the loss obtained on the shear stress in the yz-plane ($\tau_{yz}$). The shear stress in the yz-plane shows similar behaviour to the stress in x-direction since an increase in curvature will also result in an increase of the median and the spread of the predictions. The shear stress in zx-plane ($\tau_z x$) is displayed in fig. C.1f. In this plot it can again be seen that the curvature will not significantly influence the loss and the spread obtained.

The loss of the predicted von Mises stress distributions are given in fig. C.2. Figure C.2a shows the results for the directly predicted von Mises stresses. No clear conclusion could be drawn on these results because no clear behavior could be observed. Figure C.2b shows the results of the von Mises stress distribution generated from the individual stress components. It can be observed that the loss increases when the curvature of the stiffened panel increases. This behaviour is probably determined by the stress in the x-direction, which follows the same trend. Also, the stress in x-direction generates the largest losses, so it will impact the calculated von Mises stress significantly.

This appendix only shows the box plots of the obtained results. The individual mean values are displayed in fig. 8.8a and fig. 8.8b for respectively the individual stress components and the von Mises stress distribution.

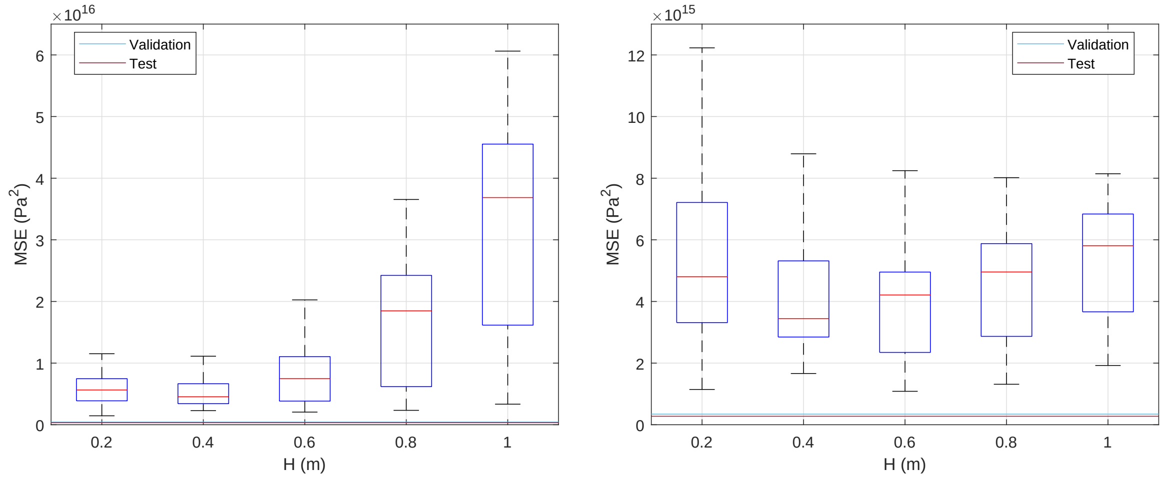

(a) Box plot of the MSE per curvature of the stress in x-direction ($\sigma_x$). It can be observed that an increase in curvature also increases the error and the spread of the errors.

(b) Box plot of the MSE per curvature of the stress in y-direction ($\sigma_y$). It can be observed that the error is not dependent on the amount of curvature.

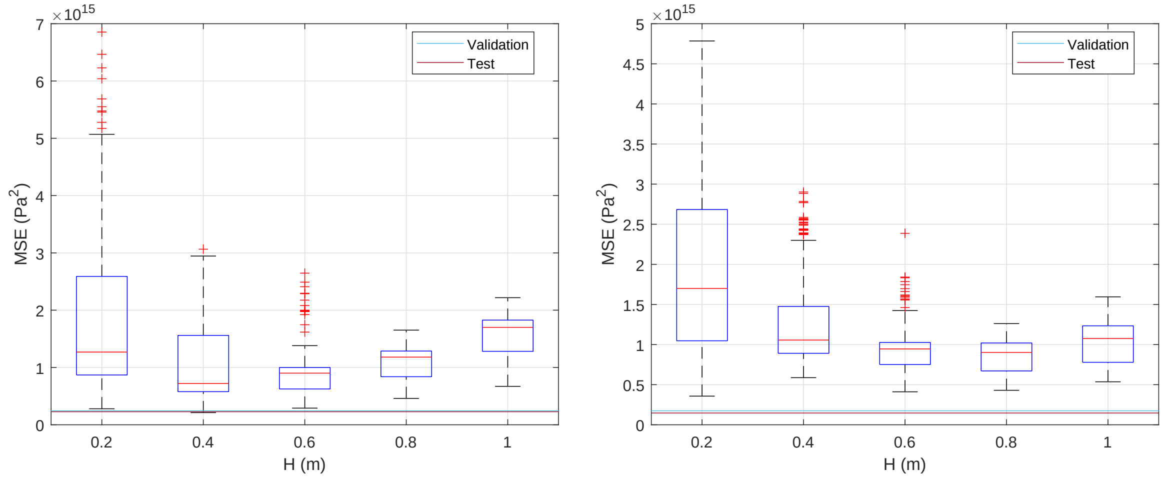

(c) Box plot of the MSE per curvature of the stress in z-direction ($\sigma_z$). It can be observed that the error is not significantly dependent on the curvature. The largest spread is observed for the smallest curvature.

(d) Box plot of the MSE per curvature of the shear in xy-plane ($\tau_{xy}$). It can be observed that the error is not significantly dependent on the curvature. The largest spread is observed for the smallest curvature.

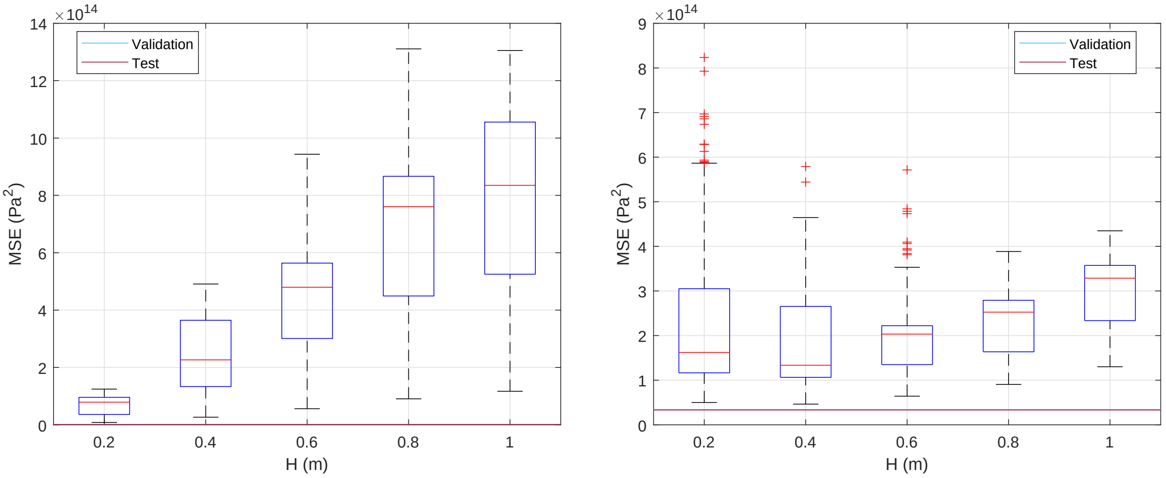

(e) Box plot of the MSE per curvature of the shear in yz-plane ($\tau_{yz}$). It can be observed that an increase in curvature also increases the error and the spread of the errors.

(f) Box plot of the MSE per curvature of the shear in zx-plane ($\tau_{zx}$). It can be observed that the error is not dependent on the amount of curvature.

Figure C.1: Generalizability box plots of the individual stress components predicted by the ML model. The plots represent the Mean Squared Error (MSE) related to the curvature of the stiffened panel. A plot is given for every individual stress component.

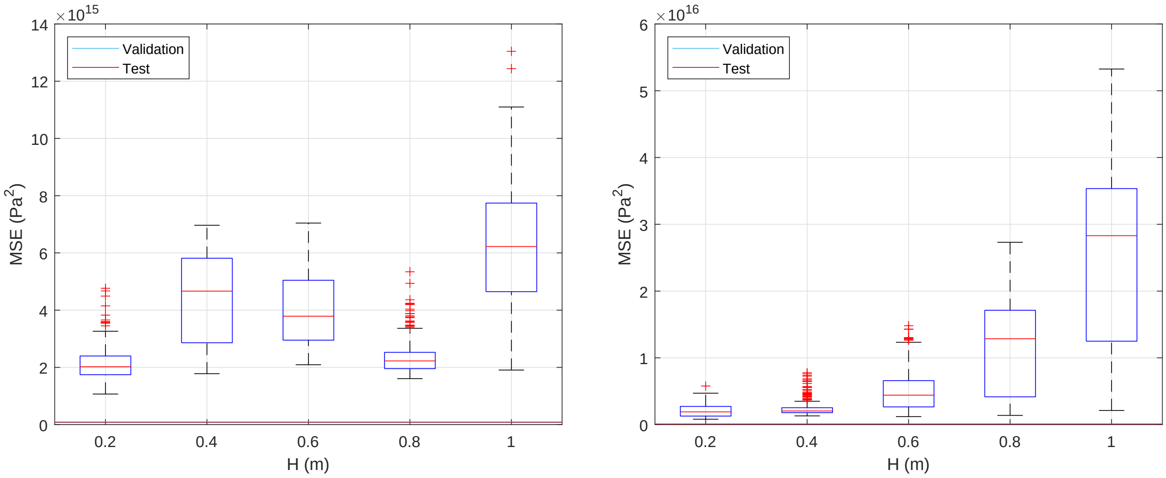

(a) Box plot of the MSE per curvature of the directly predicted Von Mises stress. The amount of curvature does not seem to have a clear effect influence on the obtained MSE.

(b) Box plot of the MSE per curvature of the von Mises stress obtained from the individual stress components. An increase in curvature also increases the MSE and the spread of the results.

Figure C.2: Generalizability box plots of the von Mises stresses predicted by the ML model. The plots represent the Mean Squared Error (MSE) related to the curvature of the stiffened panel. A plot is given for the directly predicted von Mises stress and for the von Mises stress determined by the individual stress components.